NEW MATERIALS INTERFACES AND MODELING FOR PHOTOSYSTEM I-BASED BIOHYBRID SOLAR CELLS

By

Maxwell Thatcher Robinson

Dissertation

Submitted to the Faculty of the

Graduate School of Vanderbilt University

in partial fulfillment of the requirements

for the degree of

DOCTOR OF PHILOSOPHY

in

Chemical Engineering

January 31, 2018

Nashville, Tennessee

Approved:

G. Kane Jennings, Ph.D.

Rizia Bardhan, Ph.D.

David E. Cliffel, Ph.D.

Paul E. Laibinis, Ph.D.

Ronald D. Schrimpf, Ph.D.

For my family

ACKNOWLEDGEMENTS

First, I would like to thank the many organizations that funded this work: the National Science Foundation (NSF, DMR-1507505), the United States Department of Agriculture (2013-67021-21029), NSF EPSCoR (EPS 1004083), and the Environmental Protection Agency (SU-83528701). Additional support was provided through Vanderbilt University in the form of a University Graduate Fellowship.

I would like to thank my advisor Prof. G. Kane Jennings for his sound advice and careful guidance that have steadily molded me into a competent researcher and a more grounded individual. I would also like to thank Professor David E. Cliffel for his creative ideas and support that have been helpful throughout my time at Vanderbilt. Additionally, I would like to thank Professor Ronald Schrimpf, Professor Rizia Bardhan, and Professor Paul Laibinis for offering their diverse insights as part of my thesis committee.

I would also like to thank the students that I have mentored over the years: Patrick Wellborn, Laurel Cunningham, Jane Jiang, Avi Gargye, Marie Armbruster, Clara Simons, and Bridget Anger. I'm honored to be a part of your introduction to research and I wish you all the very best in your future endeavors.

I would like to express my gratitude to the graduate students and post-docs who have made my time in Nashville fun and interesting in and out of the lab. In particular, I'd like to thank Dr. Ian Njoroge for his friendship and wisdom. Our long and often deafening discussions concerning science, politics, and philosophy were immensely entertaining and rewarding. Your many scientific insights and technical acumen have certainly made their mark on this thesis. I'd like to thank my close friends in the ChBE program who have made my home for the last 4+ years so warm and welcoming: Dan Shae, Max

Jacobson, Devon Powers, Krysta Waldrop, and Kevin Miller. Additionally, I'd like to thank Dr. Gabriel Leblanc for his patient mentoring during my first year of research. I would like to thank Faustin Mwambutsa, Ricky Deng, Leo Yang, and Josh Passantino of the Jennings lab and Dr. Evan Gizzie, Chris Stachurski, Dilek Dervishogullari, and Dr. Dusty Miller of the Cliffel lab. I want to thank members of the Bardhan lab for their generous advice over the years: Dr. Will Erwin and Dr. Holly Zarick.

I would like to thank members of Vanderbilt Institute for Nanoscale Science and Engineering (VINSE) for their assistance. In particular, I'd like to thank Dr. Dmitry Koktysh for all of the guidance and he has provided over the years with regard to the numerous characterization tools offered in the VINSE Nanocrystal/Analytical Support Core. Additionally, I'd like to thank Prof. Anthony Hmelo for his help with SEM and EDX used in the delicate characterization of composite films in Chapter 5 of this thesis.

Finally, I would like to thank my incredibly loving and supportive family to whom I dedicate this thesis. To my parents, David and Mary Ann, thank you for your broad wisdom, bright humor, and boundless kindness. Thanks for always having my back. To my brothers, Brad and Patrick, thank you for being fantastic role models, great friends, and the very best travel companions

TABLE OF CONTENTS

LIST OF TABLES

LIST OF FIGURES

CHAPTER 1

INTRODUCTION TO PHOTOSYSTEM I PROTEINS AND THEIR USE IN SOLAR CELLS

Photosynthesis is the ubiquitous solar-to-fuel conversion process used by plants, algae, and cyanobacteria to synthesize sugars from atmospheric carbon dioxide. An energetic 'Z-scheme' of specialized proteins drives photosynthesis by transducing visible light into efficient energy utilization in cell chloroplasts. Over 3.5 billion years of sustained environmental stress have fine-tuned these abundant biological machines to the Earth's climate and the Sun's radiant energy profile.[1,2]

One such protein is Photosystem I (PSI), a photodiode that achieves 1.1 V charge separation with >99% internal quantum efficiency. PSI facilitates the photo-excitation and transport of an electron necessary for reduction of the energy-carrying co-factor, nicotinamide adenine dinucleotide phosphate ($NADP^+$).[3,4] Within PSI, antenna chlorophylls guide absorbed energy to a chlorophyll A dimer, P_{700}. Energy transfer to P_{700} prompts an excited electronic state, P^*_{700}, that quickly donates to an internal electron transfer chain terminating with the iron-sulfur complex F_B (**Figure 1.1**). *In vivo*, P_{700} and F_B are electronically accessible by the mobile electron-transfer metalloproteins plastocyanin and ferredoxin, respectively.

Due to its abundance, stability, and exceptional optoelectronic properties, PSI has been extracted from photosynthetic organisms and paired with redox mediators for biohybrid solar energy conversion (**Figure 1.2**). These efforts are rooted in studies of

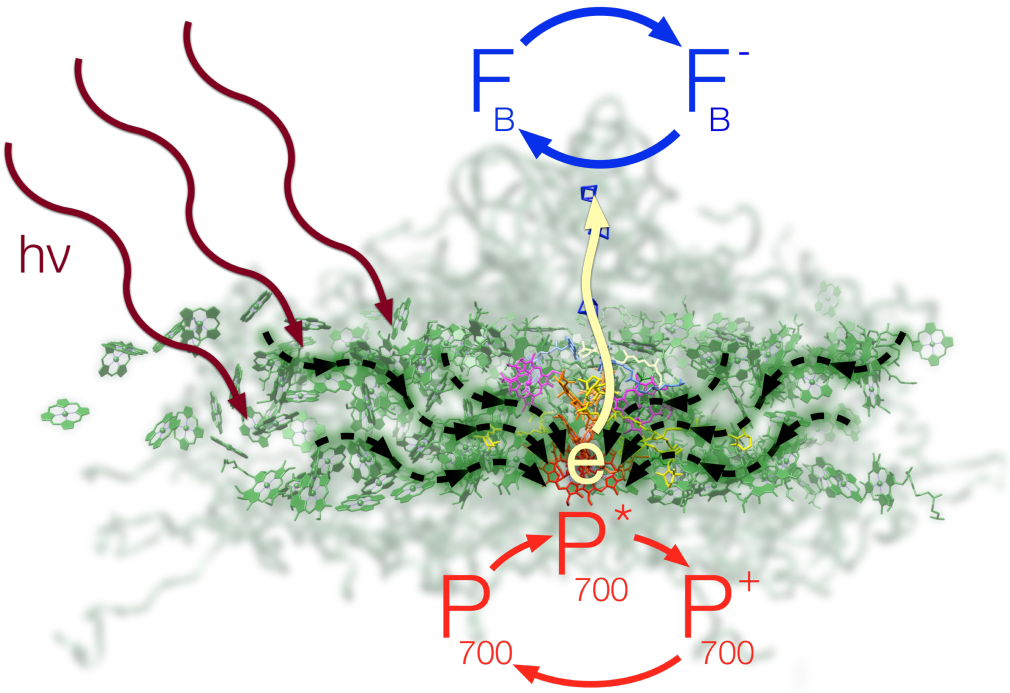

Figure 1.1. Structure and Function of a PSI Protein. PSI is a natural, nanoscale photodiode found in photosynthetic organisms. Under illumination, PSI efficiently energizes and isolates a high-energy electron for use within the chloroplasts of photosynthetic organisms. Atomic coordinates for PSI were taken from PDB entry 2o01.

chloroplasts exposed to exogenous redox ions in the 1960s.[5,6] Losada *et al.* observed that aqueous solutions containing dichloroindophenol (DCPIP) or ferricyanide rapidly oxidize chloroplasts under illumination, effectively short-circuiting electron transfer in photosynthesis.[6] Subsequently, Greenbaum *et al.* performed chloroplast platinization *via* PSI photoreduction of hexachloroplatinate. Aqueous suspensions containing platinized chloroplasts performed hydrogen evolution under illumination, due to platinum clusters bridging the biochemical reaction between F_B^- and H^+.[7–10]

The development of high-throughput PSI extraction protocols in the 1970s and 1980s stimulated ongoing efforts to apply the protein's reduction potential to heterogeneous photoelectrochemistry.[11–13] These endeavors are broadly divided into two

categories based on the mechanism of PSI/electrode charge exchange: direct electron transfer (DET) and mediated electron transfer (MET).[14–16] For DET, a sparse layer of PSI is affixed to an electrode surface to promote light-induced charge exchange with F_B^- or P_{700}^+ *via* electron tunneling and/or hopping.[17,18] Judicious combination of PSI mutagenesis[19–21]and electrode surface engineering[22,23] has led to significant improvements in PSI/electrode DET. As for analogous systems utilizing DET with molecular dyes,[24–26] power output of PSI-sensitized biophotovoltaic devices improves with increased surface area of PSI/electrode interaction.[21,27–30] Notably, Mershin *et al.* genetically engineered cyanobacterial PSI to express metal-oxide binding peptides and affixed them to three-dimensional inorganic semiconductor anodes—including films of ZnO nanorods and TiO_2 nanoparticles—for enhanced photocurrent and photovoltage as part of a dye-sensitized solar cell.[21]

In contrast, photocells based on MET exploit an electron relay—diffusible small molecules, an oxidoreductase, and/or a conductive polymer—to shuttle electrons between photoexcited PSI and an electrode surface.[15] Assemblies utilizing MET exhibit inherent inefficiencies related to additional electron transfer step(s); however, their power output can often be greatly improved simply by increasing the amount of incorporated PSI to catalyze the principal photochemical reaction(s). PSI-based photocurrent generation *via* MET was first explored and discussed in the 1970s.[31–34] Gross *et al.* constructed solar cells consisting of electrolyte-contacted platinum electrodes placed within two compartments separated by a PSI-packed cellulose-acetate membrane. The authors filled one compartment with aqueous flavin mononucleotide (FMN)—a known electron acceptor from F_B^-—and the other with aqueous ferrocyanide—a known electron donor to

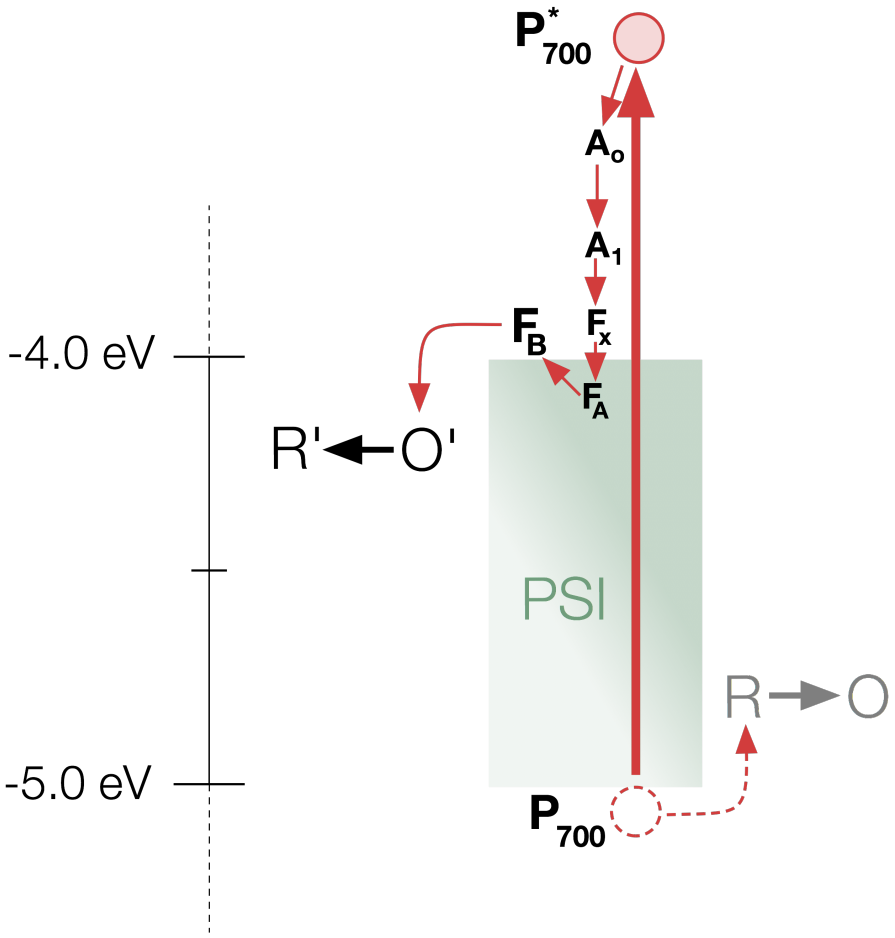

Figure 1.2. PSI as Employed Within Biohybrid Photoelectrodes. The energy diagram illustrates how exogeneous redox mediators—O' and R—are employed in targeted electron transfer reactions with high-energy (F_B) or low-energy (P_{700}) co-factors, respectively. Many conductive redox materials have been used to interface with PSI, including diffusible small molecules, enzymes, inorganic semiconductors, and polymer scaffolds.

P^{+}_{700}—and observed sustained PSI-based photocurrent. They surmised that electron exchange between photoexcited PSI and redox mediators established a chemical potential gradient between compartments and a compensating current through the external circuit.[31]

Over the previous decade, several research groups have developed strategies for

MET-based biophotovoltaics using PSI films applied directly to electrode surfaces. In 2010, we constructed a photoelectrochemical device comprising a ~1 μm PSI multilayer atop a gold cathode, a copper-contacted ITO anode, and an electrolyte containing sodium ascorbate (Asc) and DCPIP.[35] We observed sustained photocurrent and photovoltage, ostensibly due to simultaneous reduction and oxidation of PSI by reduced DCPIP and O_2, respectively. Later that year, we described a vacuum-assisted technique to rapidly assemble PSI multilayer films atop planar gold electrodes and characterized their photoelectrochemical performance as part of a three-electrode setup in a ferri/ferrocyanide electrolyte.[36] Photocurrent generation from either system was attributed to an underlying electrode's electrochemical response to the photo-induced kinetics of a PSI multilayer film, which rapidly modifies the concentration of diffusible mediators at the electrode surface. Subsequently, Badura *et al.* entrapped PSI within a crosslinked poly(vinyl)imidazole hydrogel scaffold with covalently bound $[Os(bpy)_2Cl_2]$, and exposed the composite film to an aqueous solution containing dissolved O_2 and methyl viologen (MV^{2+})—a well-studied electron relay between F_B^- and O_2. Under illumination, the reduced Os complexes in the film shuttled electrons to P_{700}^+ while freely diffusing MV^{2+} mediated high-energy electron transport from F_B^- to O_2.[37] This cell architecture was improved to permit a per-PSI electron turnover rate of 335 e^- s^{-1} PSI^{-1}, representing a more than six-fold improvement relative to that of chloroplasts *in vivo*.[38] In 2014, Stieger *et al.* assembled films containing PSI and cytochrome c and observed photocurrent enhancement due to augmented intra-film electron transport mediated by cytochrome c.[39,40] In 2015, Gizzie *et al.* used electrochemical polymerization of polyaniline (PAni) to assemble composite films of PSI:PAni from mesoporous TiO_2 films atop fluorine-doped

tin oxide (FTO), which served as an anode in a two-electrode solid-state photovoltaic cell.[41] Under 1-sun illumination, such devices generated an external quantum efficiency (EQE) of 0.01%, establishing a record for PSI-based solid-state devices and a four-fold improvement over analogous devices containing PAni only. Owing to the stability of both PAni and PSI, these devices were highly resilient under prolonged on/off cycling of illumination in ambient conditions.

Herein, new insights and materials systems for PSI-based MET are described. In Chapter 3, a first-principles study of light-driven MET for PSI multilayer films exposed to aqueous solutions containing $[Fe(CN)_6]^{4-/3-}$ is presented. In Chapter 4, a new MET-based paradigm for biohybrid solar cells is presented, in which a PSI multilayer and an anthocyanin-coated TiO_2 photoanode are linked electrochemically by diffusible $[Fe(CN)_6]^{4-/3-}$. In Chapter 5, a rapid and gentle vapor-phase approach to constructing composite films of PSI and a wide library of intrinsically conductive polymers—that includes poly(3,4-ethylenedioxythiophene) (PEDOT), polypyrrole (PPy), polythiophene (PT), and others—is presented, and the prevalence of MET within these PSI:ICP systems is explored. Finally, Chapter 6 concludes with a summary of results and new motivations and perspectives for future endeavors within the field of PSI-based biophotovoltaics.

Works Cited

(1) Alberts, B.; Bray, D.; Hopkin, K.; Johnson, A.; Lewis, J.; Raff, M.; Roberts, K.; Walter, P. *Essential Cell Biology*, 3rd ed.; Garland Science: New York, 2010.

(2) Bolton, J. R.; Hall, D. O. Photochemical Conversion and Storage of Solar Energy. *Annu. Rev. Energy* **1979**, *4*, 353–401.

(3) Golbeck, J. H. Structure, Function and Organization of the Photosystem I Reaction Center Complex. *Biochim. Biophys. Acta* **1988**, *895*, 167–204.

(4) Nelson, N.; Yocum, C. F. Structure and Function of Photosystems I and II. *Annu. rev. Plant Biol.* **2006**, *57*, 521–565.

(5) Arnon, D. I.; Losada, M.; Nozaki, M.; Tagawa, K. Photoproduction of Hydrogen, Photofixation of Nitrogen and a Unified Concept of Photosynthesis. *Nature* **1961**, *90*, 601–606.

(6) Losada, M.; Whatley, F. R.; Arnon, D. I. Separation of Two Light Reactions in Noncyclic Photo-Phosphorylation of Green Plants. *Nature* **1961**, *190*, 606–610.

(7) Greenbaum, E. Platinized Chloroplasts: A Novel Photocatalytic Material. *Science (80-.).* **1985**, *230*, 1373–1375.

(8) Greenbaum, E. Interfacial Photoreactions at the Photosynthetic Membrane Interface: An Upper Limit for the Number of Platinum Atoms Required To Form a Hydrogen-Evolving Platinum Metal Catalyst. *J. Phys Chem.* **1988**, *92*, 4571–4574.

(9) Greenbaum, E. Vectorial Photocurrents and Photoconductivity in Metalized Chloroplasts. *J. Phys. Chem.* **1990**, *94*, 6151–6153.

(10) Greenbaum, E. Kinetlc Studies of Interfacial Photocurrents in Platinized Chloroplasts. *J. Phys. Chem.* **1992**, *96*, 514–516.

(11) Thornber, J. P. Comparison of a Chlorophyll a-Protein Complex Isolated from a Blue-Green Alga with Chlorophyll-Protein Complexes Obtained from Green Bacteria and Higher Plants. *Biochim. Biophys. Acta* **1969**, *172*, 230–241.

(12) Shiozawa, J. A.; Alberte, R. S.; Thornber, J. P. The P700-Chlorophyll a-Protein. *Arch. Biochem. Biophys.* **1974**, *165*, 388–397.

(13) Reeves, S. G.; Hall, D. O. Higher Plant Chloroplasts and Grana: General Preparative Procedures (Excluding High Carbon Dioxide Fixation Ability Chloroplasts). *Methods Enzymol.* **1980**, *69*, 85–94.

(14) Plumere, N.; Nowaczyk, M. M. Biophotoelectrochemistry of Photosynthetic Proteins. *Adv Biochem Eng Biotechnol* **2016**, 1–26.

(15) Tel-vered, R.; Willner, I. Photo-Bioelectrochemical Cells for Energy Conversion , Sensing , and Optoelectronic Applications. *ChemElectroChem* **2014**, *1*, 1778–1797.

(16) Manocchi, A. K.; Baker, D. R.; Pendley, S. S.; Nguyen, K.; Hurley, M. M.; Bruce, B. D.; Sumner, J. J.; Lundgren, C. A. Photocurrent Generation from Surface Assembled Photosystem I on Alkanethiol Modified Electrodes. *Langmuir* **2013**, *29*, 2412–2419.

(17) Munge, B.; Das, S. K.; Ilagan, R.; Pendon, Z.; Yang, J.; Frank, H. A.; Rusling, J. F. Electron Transfer Reactions of Redox Cofactors in Spinach Photosystem I Reaction Center Protein in Lipid Films on Electrodes. *JACS* **2003**, *125*, 12457–12463.

(18) Ciobanu, M.; Kincaid, H. A.; Lo, V.; Dukes, A. D.; Jennings, G. K.; Cliffel, D. E. Electrochemistry and Photoelectrochemistry of Photosystem I Adsorbed on Hydroxyl-Terminated Monolayers. *J. Electroanal. Chem.* **2007**, *599*, 72–78.

(19) Das, R.; Kiley, P. J.; Segal, M.; Norville, J.; Yu, A. A.; Wang, L.; Trammell, S. A.; Reddick, L. E.; Kumar, R.; Stellacci, F.; et al. Integration of Photosynthetic Protein Molecular Complexes in Solid-State Electronic Devices. *Nano Lett.* **2004**, *4*, 1079–1083.

(20) Simmerman, R. F.; Zhu, T.; Baker, D. R.; Wang, L.; Mishra, S. R.; Lundgren, C. A.; Bruce, B. D. Engineering Photosystem I Complexes with Metal Oxide Binding Peptides for Bioelectronic Applications. *Bioconjug. Chem.* **2015**, *26*, 2097–2105.

(21) Mershin, A.; Matsumoto, K.; Kaiser, L.; Yu, D.; Vaughn, M.; Nazeeruddin, M. K.; Bruce, B. D.; Grätzel, M.; Zhang, S. Self-Assembled Photosystem-I Biophotovoltaics on Nanostructured TiO_2 and ZnO. *Sci. Rep.* **2012**, *2*, 1–7.

(22) Faulkner, C.; Lees, S.; Ciesielski, P.; Cliffel, D.; Jennings, G. Rapid Assembly of Photosystem I Monolayers on Gold Electrodes. *Langmuir* **2008**, *24*, 8409–8412.

(23) Le, R. K.; Raeeszadeh-Sarmazdeh, M.; Boder, E. T.; Frymier, P. D. Sortase-Mediated Ligation of PsaE-Modified Photosystem I from Synechocystis Sp. PCC 6803 to a Conductive Surface for Enhanced Photocurrent Production on a Gold Electrode. *Langmuir* **2015**, *31*, 1180–1188.

(24) Grätzel, M. Photoelectrochemical Cells. *Nature* **2001**, *414*, 338–344.

(25) Hardin, B. E.; Snaith, H. J.; McGehee, M. D. The Renaissance of Dye-Sensitized Solar Cells. *Nat. Photonics* **2012**, *6*, 162–169.

(26) Richhariya, G.; Kumar, A.; Tekasakul, P.; Gupta, B. Natural Dyes for Dye Sensitized Solar Cell : A Review. *Renew. Sustain. Energy Rev.* **2017**, *69*, 705–718.

(27) Ciesielski, P. N.; Scott, A. M.; Faulkner, C. J.; Berron, B. J.; Cliffel, D. E.; Jennings, G. K. Functionalized Nanoporous Gold Leaf Electrode Films for the Immobilization of Photosystem I. *ACS Nano* **2008**, *2*, 2465–2472.

(28) Ocakoglu, K.; Krupnik, T.; van den Bosch, B.; Harputlu, E.; Gullo, M. P.; Olmos, J. D. J.; Yildirimcan, S.; Gupta, R. K.; Yakuphanoglu, F.; Barbieri, A.; et al. Photosystem I-Based Biophotovoltaics on Nanostructured Hematite. *Adv. Funct.*

Mater. **2014**, *24*, 7467–7477.

(29) Yu, D.; Wang, M.; Zhu, G.; Ge, B.; Liu, S.; Huang, F. Enhanced Photocurrent Production by Bio-Dyes of Photosynthetic Macromolecules on Designed TiO_2 Film. *Sci. Rep.* **2015**, *5*, 1–9.

(30) Peters, K.; Lokupitiya, H. N.; Sarauli, D.; Labs, M.; Pribil, M.; Kuhn, A.; Leister, D.; Stefik, M.; Fattakhova-Rohlfing, D. Nanostructured Antimony-Doped Tin Oxide Layers with Tunable Pore Architectures as Versatile Transparent Current Collectors for Biophotovoltaics. *Adv. Funct. Mater.* **2016**, *26*, 6682–6692.

(31) Gross, E. L.; Youngman, D. R.; Winemiller, S. L. An FMN-Photosystem I Photovoltaic Cell. *Photochem. Photobiol.* **1978**, *28*, 249–256.

(32) Bhardwaj, R.; Pan, R. L.; Gross, E. L. Solar Energy Conversion by Chloroplast Photoelectrochemical Cells. *Nature* **1981**, *289*, 396–398.

(33) Bhardwaj, R.; Pan, R. L.; Gross, E. L. A Photosystem I-Phenosafranine Solar Cell. *Photochem. Photobiol.* **1981**, *34*, 215–222.

(34) Pan, R. L.; Bhardwaja, R.; Gross, E. L. Photochemical Energy Conversion by a Thiazine Photosynthetic-Photoelectrochemical Cell. *J. Chem. Tech. Biotechnol.* **1983**, *33A*, 39–48.

(35) Ciesielski, P. N.; Hijazi, F. M.; Scott, A. M.; Faulkner, C. J.; Beard, L.; Emmett, K.; Rosenthal, S. J.; Cliffel, D.; Jennings, G. K. Photosystem I - Based Biohybrid Photoelectrochemical Cells. *Bioresour. Technol.* **2010**, *101*, 3047–3053.

(36) Ciesielski, P. N.; Faulkner, C. J.; Irwin, M. T.; Gregory, J. M.; Tolk, N. H.; Cliffel, D. E.; Jennings, G. K. Enhanced Photocurrent Production by Photosystem I Multilayer Assemblies. *Adv. Funct. Mater.* **2010**, *20*, 4048–4054.

(37) Badura, A.; Guschin, D.; Kothe, T.; Kopczak, M. J.; Schuhmann, W.; Rögner, M. Photocurrent Generation by Photosystem 1 Integrated in Crosslinked Redox Hydrogels. *Energy Environ. Sci.* **2011**, *4*, 2435.

(38) Kothe, T.; Pöller, S.; Zhao, F.; Fortgang, P.; Rögner, M.; Schuhmann, W.; Plumeré, N. Engineered Electron-Transfer Chain in Photosystem 1 Based Photocathodes Outperforms Electron-Transfer Rates in Natural Photosynthesis. *Chem. Eur. J.* **2014**, *20*, 1–7.

(39) Stieger, K. R.; Ciornii, D.; Kölsch, A.; Hejazi, M.; Lokstein, H.; Feifel, S. C.; Zouni, A.; Lisdat, F. Engineering of Supramolecular Photoactive Protein Architectures: The Defined Co-Assembly of Photosystem I and Cytochrome c Using a Nanoscaled DNA-Matrix. *Nanoscale* **2016**, *8*, 10695–10705.

(40) Stieger, K. R.; Feifel, S. C.; Lokstein, H.; Lisdat, F. Advanced Unidirectional Photocurrent Generation via Cytochrome c as Reaction Partner for Directed Assembly of Photosystem I. *PCCP* **2014**, *16*, 15667–15674.

(41) Gizzie, E. A.; Scott Niezgoda, J.; Robinson, M. T.; Harris, A. G.; Jennings, G. K.; Rosenthal, S. J.; Cliffel, D. E. Photosystem I-polyaniline/TiO_2 Solid-State Solar Cells: Simple Devices for Biohybrid Solar Energy Conversion. *Energy Environ. Sci.* **2015**, *8*, 3572–3576.

CHAPTER 2

EXPERIMENTAL AND ANALYTICAL TECHNIQUES

Extraction and Isolation of PSI Proteins from Spinach

The extraction procedure described herein is an adaptation of that described by Reeves and Hall[1] and Shiozawa *et al*.[2] Typically, all buffers and media (grinding medium, re-suspending medium, elution buffer, and column buffer) were made the day prior to extraction. The grinding medium consisted of 330 mM sorbitol, 10 mM sodium pyrophosphate, 4 mM magnesium chloride, and 2 mM ascorbic acid (300 mL, pH 6.5). The re-suspending medium incorporated 330 mM sorbitol, 2 mM ethylenediaminetetraacetate, 10 mM magnesium chloride, and 1 mM manganese chloride, 1% w/v Triton X-100, and 50 mM HEPES (pH 7.6) The column buffer used was a 10 mM phosphate solution (pH 7.0). The elution buffer used was a 200 mM phosphate solution with 0.05 % w/v Triton X-100 included (pH 7.0).

Store-bought baby spinach leaves were de-veined with a scalpel. De-veined leaves (150 g) were collected and were homogenized in chilled grinding medium with a household blender until the mixture had an even consistency. This mixture was iteratively filtered, first with 2 layers and then with 8 layers of cheesecloth. Next, the filtered suspension was divided into 8 centrifuge tubes and centrifuged for 1 min at 8000 x g (T = 4 °C) to pellet thylakoid membranes. The supernatant was discarded and the thylakoid-containing pellets were re-suspended in a maximum of 20 mL re-suspending medium, which lysed the thylakoids to release PSI and other proteins into the re-suspension

solution. Either cotton swabs or vortexing was used to aid in re-suspension. This suspension was reconstituted into a single centrifuge tube then centrifuged at 20 000 x g for 15 min (T = 4 °C) with a counterweight tube filled with water. The supernatant from this step was then poured over the top of a water-jacketed hydroxylapatite column (T = 4 °C) that was equilibrated with column buffer. This eluent was drawn through the column until the liquid level was just above the top of the hydroxylapatite. Next, column buffer was used to rinse the protein in the stationary phase until the eluate was clear. Elution buffer was then added to elute PSI. Eluate solution was collected as product once the solution began to turn visibly green—typically after approximately 10 mL of elution buffer + PSI was drawn off the column. To maximize concentration of the purified PSI solution, collection ceased after 50 mL. This solution was collected into 1 mL aliquots and stored at -80 °C for later use.

Spectroscopic Quantification of Purified PSI Solutions

To calculate the concentration of chlorophylls, two separate single beam absorbance measurements were made on solutions containing 50 µL of purified PSI solution and 2450 µL of a solution containing 80% v/v acetone and 20% v/v water at 645 nm and 663 nm, respectively. The concentrations of chlorophyll a and chlorophyll b are calculated first and added to quantify total chlorophyll concentration according to the formulation by Arnon *et al.*,[3]

$$[ChlA] = 0.0127A_{663} - 0.00269A_{645} \quad (1)$$

$$[ChlB] = 0.0229A_{663} - 0.00468A_{645} \quad (2)$$

$$[Chl] = [ChlA] + [ChlB] \quad (3)$$

Differential absorbance spectroscopy was used to quantify the concentration of active P_{700} in purified PSI solutions. Briefly, two cuvettes were each filled with 2275 μL of Baba assay solution (50 mM tricine, 100 mM sorbitol, 10 mM NaCl, and 0.05 % w/v Triton X-100) and 100 μL of purified PSI solution. The solutions were mixed thoroughly and a dual beam measurement between 650 nm and 750 nm was conducted and again after 5 min. 120 μL of deionized water (18.2 MΩ) was added to the reference cuvette. Simultaneously, 125 μL of a 1 M solution of $[Fe(CN)_6]^{3-}$ and 5 μL of a solution containing 0.5 M sodium ascorbate and 5 mM dithiothreitol (Cleland's Reagent) were added to the sample and reference cuvettes, respectively. A 650 nm to 750 nm scan was conducted immediately and another 15 min later. The absorbance data from this last scan were subtracted from that of the 5-min baseline. The peak absorbance was subtracted from the isosbestic point at 725 nm and used to calculate a concentration of P_{700} using Beer's Law and the molar absorptivity of P_{700} (64 000 M^{-1} cm^{-1}). Typically, this analysis yielded values for $[P_{700}]$ and $[chl]/[P_{700}]$ of 1-10 μM and 40-45, respectively.

Preparation of PSI Multilayer Films

Vacuum-assisted assembly was employed to prepare PSI multilayer films on a desired substrate.[4] Briefly, an aqueous PSI solution within a 10 000 MWCO cellulose dialysis tubing (Spectrum Labs) was dialyzed for 12 h in 2 L of deionized water (18.2 MΩ) in order to reduce concentrations of Triton X-100 and phosphate. The dialyzed

solution was then deposited atop a substrate of choice. The substrate was then placed under vacuum, stimulating water evaporation and the formation of a dense PSI film. PSI's hydrophobic domains become intermeshed during water evaporation and thus, the dried film is not removed by subsequent exposure to aqueous electrolyte.

Photoelectrochemical Analysis of PSI Films

Ciesielski *et al.* suggested that the photoactivity of an unstructured PSI multilayer film in an electrolyte containing a diffusible redox pair (*i.e.* aqueous $[Fe(CN)_6]^{4-/3-}$) derives from imbalanced electron transfer reactions between immobilized PSI co-factors in the film and nearby mediators.[4–6] Assuming the electrolyte contains a single redox pair with a formal potential intermediate to that of P_{700} and F_B, mediator concentrations within the film are modified by homogeneous reactions,

$$P_{700}^{+} + R \rightarrow P_{700} + O \tag{4}$$

$$F_B^{-} + O \rightarrow F_B + R \tag{5}$$

where R and O are the reduced and oxidized forms of a redox pair interacting with P_{700}^{+} and F_B^{-}, respectively. Provided that the rates of PSI reduction (eq 4) and PSI oxidation (eq 2) are not equal, illumination will prompt a sustained change in concentration of R and O within the PSI film and a subsequent diffusional response within the electrolyte.

A metal electrode can be used to monitor the photo-induced modification of mediator concentrations generated from a PSI film deposited on its surface. Given that PSI-electrolyte reactions—eq 4 & 5—predominate, photopotential is related directly to the relative surface concentrations of redox species *via* the Nernst expression (eq 6)[7]

$$\Delta E_p = \frac{RT}{nF} ln\left[\left(\frac{C_R^*}{C_O^*}\right)\left(\frac{C_O(0,t)}{C_R(0,t)}\right)\right] \quad (6)$$

where R is the gas constant, T is the temperature in Kelvin, F is the Faraday constant (96485 C/mol), C_R^* is the bulk concentration of reduced species, and C_O^* is the bulk concentration of oxidized species. $C_O(0,t)$ and $C_R(0,t)$ are the time-dependent surface concentrations of the oxidized and reduced species, respectively. The logarithmic dependence of ΔE_p is significant in that it reveals that even large changes in surface concentration lead to modest photopotential. Slight photopotentials (<100 mV) coupled to diffusional limitations are thus implicit evidence of a MET-based mechanism (**Figure 2.1a**).[5] In this thesis, photovoltage measurements were performed using a CH instruments

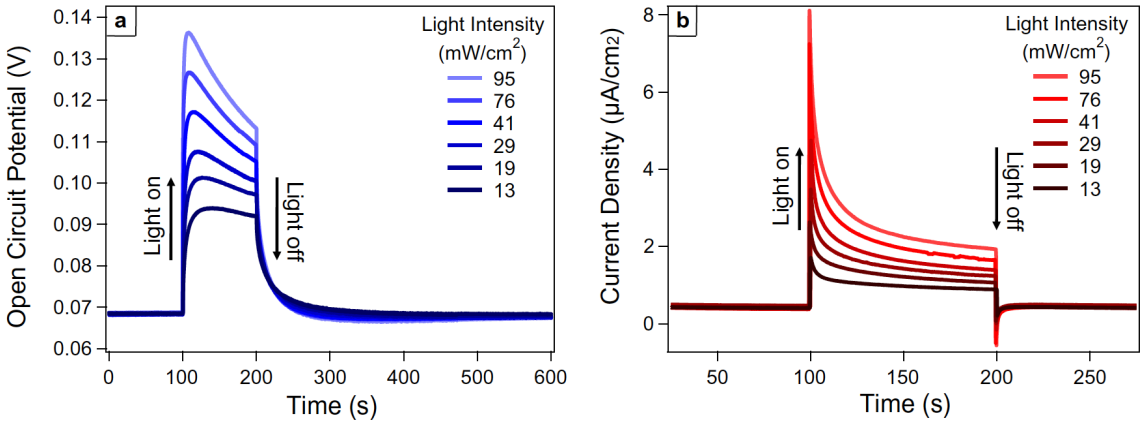

Figure 2.1 Photoresponse of a PSI Multilayer Film. When exposed to a redox electrolyte, PSI multilayers rapidly produce (a) photovoltage and (b) photocurrent due to homogeneous reaction occurring within the dense, three-dimensional film structure. Tests were conducted in an aqueous electrolyte containing 5 mM Asc, 250 μM DCPIP, 100 mM KCl, and 5 mM phosphate buffer (pH 7.0). Reprinted with permission from Ref. 5.

CH660a potentiostat that included a three-electrode setup: a Ag/AgCl reference electrode, platinum mesh counter electrode, and a specified working electrode.

The short-circuit photocurrent density (j_{sc}) supplied by a PSI multilayer is often measured using photochronoamperometry (PCA), whereby the working electrode is set to the dark open circuit potential and the compensating current is measured under illumination. Assuming a reversible redox couple, photocurrent density is related to heterogeneous kinetics as articulated by the Butler-Volmer expression (eq 7)[7]

$$j_{sc} = Fk^0 C_O^{*(1-\alpha)} C_R^{*\alpha} \left[\frac{C_O(0,t)}{C_O^*} - \frac{C_R(0,t)}{C_R^*} \right] \quad (7)$$

where k^0 is the standard rate constant and α is the transfer coefficient. Unstructured PSI films on planar metal electrodes generate photocurrents of up to 10 μA/cm^2, representing more than two orders of magnitude improvement relative to an analogous electrode-contacted PSI monolayer (**Figure 2.1b**).[8] The pronounced photoelectrochemical performance of unstructured PSI multilayer films is manifest on many electrode surfaces, including gold,[4,5,9,10] silicon,[11,12] graphene,[13] and reduced graphene oxide.[14] All PCA measurements documented in this thesis were conducted using a CH660a potentiostat with a three-electrode setup consisting of a Ag/AgCl reference electrode, platinum mesh counter electrode, and a specified working electrode.

Contact Profilometry

Contact profilometry is a scanning probe technique that provides topographical information for substrates with features of 20 nm up to 50,000 nm (50 μm). During a

profilometric scan, the deflection of a diamond-tipped cantilever is monitored as it is moved along a linear path in contact with a sample substrate to determine changes in surface height. Herein, a Veeco DEKTAK 150 contact profilometer was used to measure the thickness and surface features of prepared films of PSI, PSI/polymer composites, polymer, and TiO_2 on electrode surfaces.

Electrochemical Impedance Spectroscopy

Electrochemical impedance spectroscopy (EIS) is a widely applied technique that uses a small (5-10 mV) oscillating potential at a working electrode to probe for processes that influence current within an electrochemical cell. Typically, EIS measurements start with high frequencies ($f \geq 10$ kHz) such that only the resistance due to migration of dissolved ions is measured (R_{ct}) and progressively move to lower frequencies for which slower processes can be observed—double layer capacitance, pseudocapacitance, heterogeneous charge-transfer, and bulk reactions.[7] A subsequently applied electrical circuit model is applied to evaluate physical and chemical quantities related to these processes. In Chapter 3, EIS is used to determine a value for standard rate constant associated with gold electrode coated with the amine-terminated self-assembled monolayer (SAM), aminoethane thiol (AET), and/or a subsequently deposited PSI multilayer film when contacted with an aqueous solution containing $[Fe(CN)]^{4-/3-}$. In Chapter 5, EIS is used to monitor the psuedocapacitance of composite films of PSI and the intrinsically conductive polymer (ICP) poly(3,4-ethylenedioxythiophene) (PEDOT) to provide information about prevalence of the constituents throughout the assemblies. The circuits developed for accurate modeling of the system are presented in each representative section.

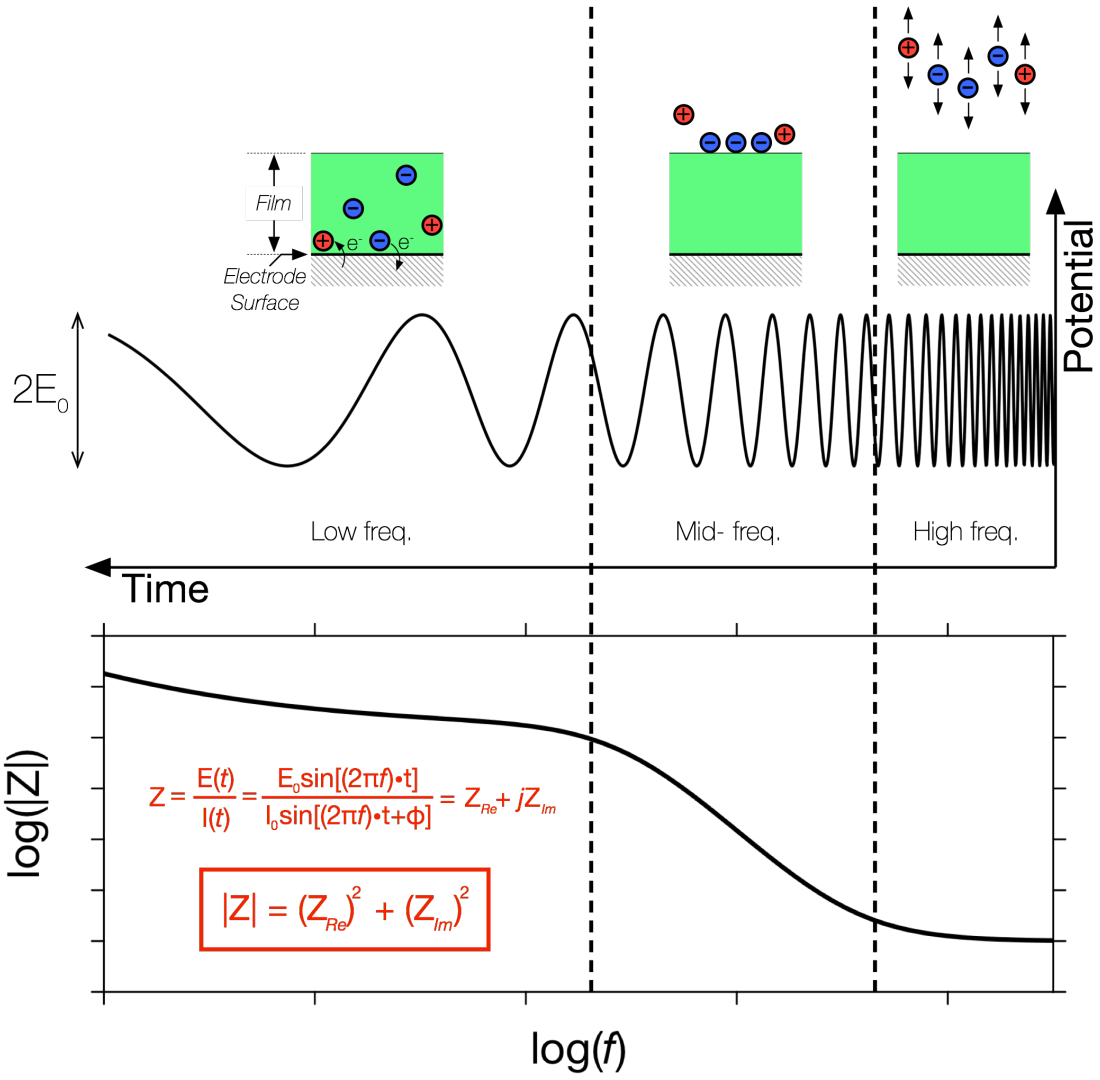

Figure 2.2. Visual Representation of Electrochemical Impedance Spectroscopy (EIS). Top: In EIS, a sinusoidal potential of decaying frequency (*f*) but constant amplitude (E_0) is applied at the working electrode of an electrochemical cell. As the voltage frequency decreases, gradually slower electrochemical processes can be monitored by changes in magnitude (I_o) and phase shift (ϕ) of measured current. Bottom: A Bode plot of the impedance magnitude ($|Z|$) of an electrochemical cell under variable applied voltage frequencies. The response is plotted in log-log format and demonstrates characteristic behavior of a Randles circuit.

Polarization Modulation-Infrared Reflection Absorption Spectroscopy (PM-IRRAS)

PM-IRRAS is an optical technique that employs infrared light to extract structural information from thin films on reflective substrates. Infrared light stimulates vibrational modes of bonds within organic molecules that are specific to the particular frequency used. In this way, absorbance peaks from PM-IRRAS are used to detect the presence, prevalence, and orientation of different types of chemical bonds. In Chapter 5, PM-IRRAS is used to probe for the secondary structure of PSI proteins included in a PSI:vpPEDOT composite film. The shape of the Amide I (1667 cm^{-1}) and Amide II peaks (1546 cm^{-1})—associated with polypeptide C=O stretching and N-H bending, respectively—are a result of the secondary structure of a protein, respectively. Deconvolution of these peaks according to known standards[15] was used to determine any changes to the prevalence of structural motifs within PSI proteins in the film—including alpha helix, beta turn, beta sheets, and unordered helix—due to processing.

Table 2.1. PSI Secondary Structure Peak Assignments PM-IRRAS Deconvolution

Component	Wavenumber (cm^{-1})
β turn	1616-1620 1680-1690
β sheet	1624-1636 1692-1697
α helix	1648-1660 1663-1667
unordered helix	1638-1645

UV-vis Spectroscopy

UV-vis spectroscopy is used to measure the ultraviolet (UV) and visible (vis) absorbance of species in solution and assembled on a substrate. Concentration information can be extracted from UV-vis data *via* application of the Beer-Lambert law,

$$A = \varepsilon c l \tag{8}$$

where A is the absorbance of a medium of interest, ε is the molar absorptivity of an absorbing species at the stimulating wavelength, and l is the path length of the sample. UV-vis spectroscopy is used in quantification of chlorophyll and P_{700} concentrations from solutions containing PSI. In Chapter 5, a reflectance-absorbance attachment was used to quantify the amount of PSI within the center regions of PSI:vpPEDOT films assembled on reflective gold substrates.

Scanning Electron Microscopy (SEM)

SEM is an imaging technique that rasters a focused beam of small wavelength electrons—primary electrons—on a sample under vacuum to provide a high-resolution image based on the sample's electron scattering properties. Secondary electrons are produced from collisions between primary electrons and the sample up to a few nanometers in depth and typically constitute the bulk of the electrons that traverse to the detector to be used in imaging. In Chapter 5, SEM is used to provide information about the hierarchical structure of PSI:vpPEDOT films; a lower PSI:vpPEDOT region and an upper vpPEDOT region present darker and brighter region in SEM images due to their lower and higher electron scattering properties, respectively.

Energy Dispersive X-ray (EDX) Spectroscopy

Primary electrons directed at a sample can stimulate a signature emission of x-rays due to stimulation of core electrons of a particular element. In EDX spectroscopy, this feature is employed to extract elemental composition of regions of solid sample in an SEM chamber. In Chapter 5, EDX spectroscopy is used to elucidate the chemical composition of the cross-sections of PSI:vpPEDOT films in order to determine the relative prevalence of protein and polymer along a line scan perpendicular to the underlying gold substrate.

Works Cited

(1) Reeves, S. G.; Hall, D. O. Higher Plant Chloroplasts and Grana: General Preparative Procedures (Excluding High Carbon Dioxide Fixation Ability Chloroplasts). *Methods Enzymol.* **1980**, *69*, 85–94.

(2) Shiozawa, J. A.; Alberte, R. S.; Thornber, J. P. The P700-Chlorophyll a-Protein. *Arch. Biochem. Biophys.* **1974**, *165*, 388–397.

(3) Arnon, D. I. Copper Enzymes in Isolated Chloroplasts. Polyphenoloxidase in Beta Vulgaris. *Plant Physiol.* **1949**, *24*, 1–15.

(4) Ciesielski, P. N.; Faulkner, C. J.; Irwin, M. T.; Gregory, J. M.; Tolk, N. H.; Cliffel, D. E.; Jennings, G. K. Enhanced Photocurrent Production by Photosystem I Multilayer Assemblies. *Adv. Funct. Mater.* **2010**, *20*, 4048–4054.

(5) Ciesielski, P. N.; Hijazi, F. M.; Scott, A. M.; Faulkner, C. J.; Beard, L.; Emmett,

K.; Rosenthal, S. J.; Cliffel, D.; Jennings, G. K. Photosystem I - Based Biohybrid Photoelectrochemical Cells. *Bioresour. Technol.* **2010**, *101*, 3047–3053.

(6) Ciesielski, P. N. PhD Thesis: Photosystem I-Based Systems for Photoelectrochemical Energy Conversion, Vanderbilt University, 2010.

(7) Bard, A. J.; Faulkner, L. R.; Swain, E.; Robey, C. *Electrochemical Methods*, Second.; John Wiley & Sons, Inc., 2001.

(8) Faulkner, C.; Lees, S.; Ciesielski, P.; Cliffel, D.; Jennings, G. Rapid Assembly of Photosystem I Monolayers on Gold Electrodes. *Langmuir* **2008**, *24*, 8409–8412.

(9) Yang, S.; Robinson, M. T.; Mwambutsa, F.; Cliffel, D. E.; Jennings, G. K. Effect of Cross-Linking on the Performance and Stability of Photocatalytic Photosystem I Films. *Electrochim. Acta* **2016**, *222*, 926–932.

(10) Chen, G.; LeBlanc, G.; Jennings, G. K.; Cliffel, D. E. Effect of Redox Mediator on the Photo-Induced Current of a Photosystem I Modified Electrode. *J. Electrochem. Soc.* **2013**, *160*, H315–H320.

(11) LeBlanc, G.; Chen, G.; Gizzie, E. A.; Jennings, G. K.; Cliffel, D. E. Enhanced Photocurrents of Photosystem I Films on P-Doped Silicon. *Adv. Mater.* **2012**, *24*, 5959–5962.

(12) LeBlanc, G.; Winter, K. M.; Crosby, W. B.; Jennings, G. K.; Cliffel, D. E. Integration of Photosystem I with Graphene Oxide for Photocurrent Enhancement. *Adv. Energy Mater.* **2014**, *4*, 1–5.

(13) Gunther, D.; LeBlanc, G.; Prasai, D.; Zhang, J. R.; Cliffel, D. E.; Bolotin, K. I.;

Jennings, G. K. Photosystem I on Graphene as a Highly Transparent, Photoactive Electrode. *Langmuir* **2013**, *29*, 4177–4180.

(14) Darby, E.; Leblanc, G.; Gizzie, E. A.; Winter, K. M.; Jennings, G. K.; Cliffel, D. E. Photoactive Films of Photosystem I on Transparent Reduced Graphene Oxide Electrodes. *Langmuir* **2014**, *30*, 8990–8994.

(15) Kincaid, H. A.; Niedringhaus, T.; Ciobanu, M.; Cliffel, D. E.; Jennings, G. K. Entrapment of Photosystem I within Self-Assembled Films. *Langmuir* **2006**, *22*, 8114–8120.

CHAPTER 3

AN ELECTROCHEMICAL REACTION-DIFFUSION MODEL OF THE PHOTOCATALYTIC EFFECT OF PHOTOSYSTEM I MULTILAYER FILMS

Introduction

Photosynthesis enables plants and cyanobacteria to globally harvest solar energy and is enabled by environmentally adapted proteins.[1] Photosystem I (PSI) is one such protein, a transmembrane photodiode that performs efficient light transduction in the thylakoid membranes of chloroplasts.[2,3] Specifically, PSI consolidates 1.1 V of sustained photopotential with nearly perfect internal quantum efficiency. PSI is also remarkably durable; long-term preservation of activity has been observed for isolated PSI suspended in solution[4] or stabilized on an electrode surface.[5–8] In the extensive effort to develop carbon-neutral energy resources, PSI has emerged as a naturally abundant alternative to the often prohibitively expensive and toxic synthetic materials used in modular 3rd generation solar cells, which includes both dye-sensitized solar cells[9] and organic photovoltaic devices.[10]

PSI's exceptional properties are the result of tightly coordinated intra-protein functions: light absorption, photogeneration, and electron transport. Briefly, PSI's peripheral chlorophylls siphon optical excitation *via* resonance energy transfer to the chlorophyll special pair (P_{700}), prompting rapid photogeneration (P^*_{700}). This excited electron then traverses an energetically stepped electron transport chain (ETC) to reach a terminal acceptor, the iron-sulfur cluster F_B.

Researchers have extracted PSI proteins from organisms for use within biohybrid photoelectrochemical cells, which are classified by the route of charge transfer between PSI and an electrode[11,12]: direct electron transfer (DET) and mediated electron transfer (MET). In biohybrid cells that exploit DET, PSI's terminal co-factors exchange charge with an electrode by way of electron tunneling or hopping[9,13] and so, the orientation of PSI proteins at the electrode surface largely dictates the direction and magnitude of generated photocurrent. In 2011, we formulated an electrochemical model for photocurrent development from biohybrid cells consisting of a PSI monolayer bound to a planar metal electrode in an electrolyte containing the reversible redox pair, $[Fe(CN)_6]^{4-/3-}$.[14] DET was determined to be the dominant mechanism underlying photocurrent; correspondingly, photocurrent intensity was predicted to be acutely dependent on the orientation of PSI at the electrode surface—with a modest upper limit of ~1 $\mu A/cm^2$ for perfectly oriented monolayers.

On the other hand, MET-based photocells facilitate charge exchange between PSI and an electrode using mediators, which include diffusible small molecules,[5,6,15–18] redox hydrogels,[19,20] oxidoreductases,[21,22] and intrinsically conductive polymers.[7,8,23] The former case is the seminal example of MET in PSI-based biophotovoltaics, and cells of this type can be constructed using a straightforward procedure. Briefly, a solution containing PSI and minimal surfactant is drop cast atop a substrate, leaving behind an unstructured PSI multilayer film that resists removal when contacted with an aqueous electrolyte containing dissolved mediator species.[24] PSI multilayers generate orders of magnitude more photocurrent than that produced by monolayers under identical testing conditions.[11] However, the fundamental mechanisms that underpin photocurrent

production from such systems have not been explored on a rigorous, first-principles basis. Herein, we formulate and optimize an electrochemical reaction-diffusion model of an electrode-contacted PSI multilayer film in the presence of an electrolyte containing the reversible redox pair, $[Fe(CN)_6]^{4-/3-}$. The fitted model accurately simulates photocurrent trends with PSI multilayer thickness and working electrode bias. The accessible computational techniques used here permit improved fundamental understanding of the light-initiated charge transfer processes in assemblies of PSI *ex vivo* but also are broadly applicable to analysis of MET within multilayer films of other light-active proteins—such as Photosystem II, bacteriorhodopsin and the various light harvesting complexes—and of light-inactive oxidoreductases, such as glucose oxidase.

Computational Methods

Model Description

We hypothesize that a PSI multilayer film atop a metal electrode and immersed in an electrolyte containing diffusible mediators generates photocurrent *via* MET, whereby imbalanced electron transfer reactions between immobilized PSI co-factors and mediators modify the concentrations of mediators at the electrode surface to stimulate a compensating photocurrent response. We formulate a 1-D electrochemical reaction-diffusion model to simulate the chemical reactions and mediator transport processes that underpin photocurrent production during a chronoamperometric experiment (**Figure 3.1**): diffusion in the bulk electrolyte ($x > H$), reaction-diffusion in the PSI film ($0 < x \leq H$), and surface reactions between mediators and the metal electrode ($x = 0$). The developed model is solved for photocurrent and concentration profiles within MATLAB's numerical

partial differential equation solver, *pdepe*.

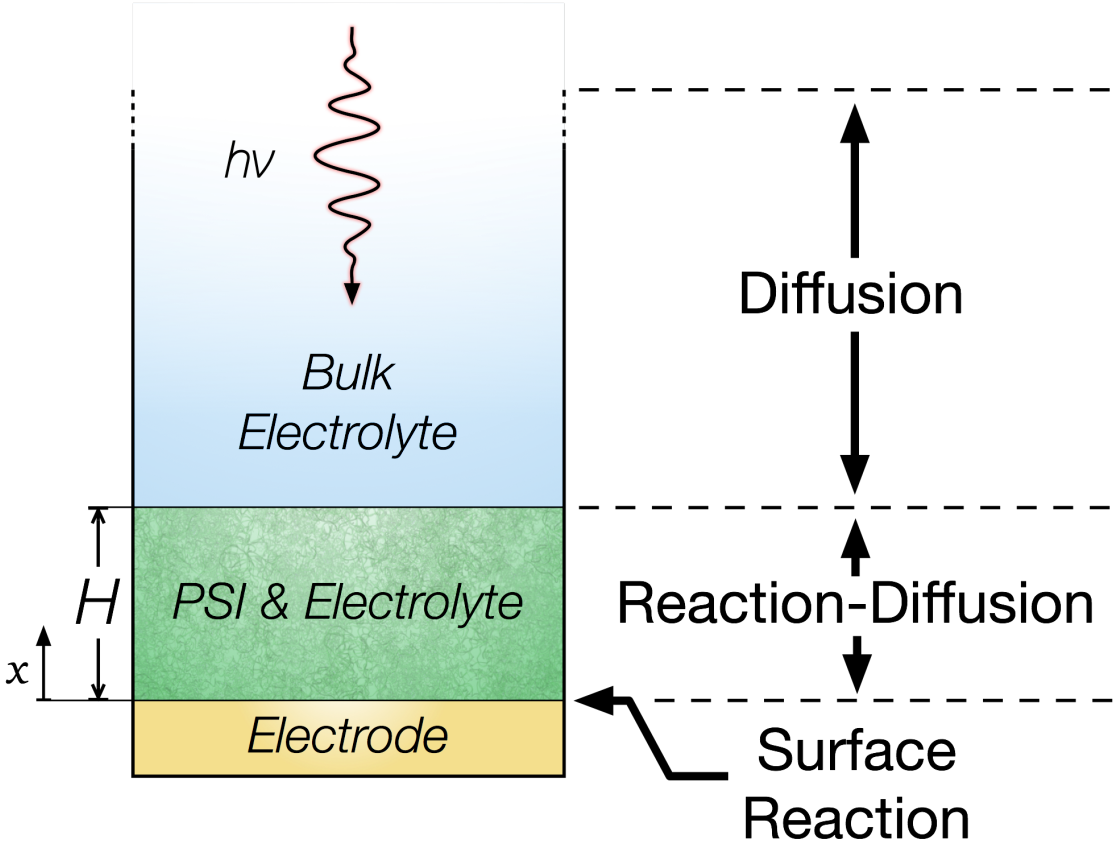

Figure 3.1. Control Volume Used in Model. The photocatalytic effect of an unstructured PSI multilayer film was modeled *via* an electrochemical, reaction-diffusion model. The overall electrochemical cell volume is subdivided into interfaces/regions: Faradaic interactions at the electrode/solution interface ($x = 0$), reaction-diffusion in the PSI film ($0 < x \leq H$), and diffusion of mediators in the electrolyte bulk ($x > H$).

To obtain values for the constants governing PSI/mediator and intra-PSI electron transfer reactions, a fitting algorithm based on MATLAB's *fminsearch* function was used to iteratively reduce the squared error between simulated and experimental chronoamperometric data from the time of illumination until 40 s after the light source was turned off. This fitting routine was employed on data extracted from a single chronoamperometric experiment in which the applied bias was zero, the thickness of the PSI multilayer film was 0.65 μm, and the electrolyte solution initially contained 0.1 mM of both $[Fe(CN)_6]^{4-}$ and $[Fe(CN)_6]^{3-}$ that served as diffusible redox mediators. All chronoamperometric measurements employed herein were conducted with half cells comprised of an electrolyte containing $[Fe(CN)_6]^{4-}$ and $[Fe(CN)_6]^{3-}$ in contact with a gold working electrode coated with the amine-terminated self-assembled monolayer (SAM), aminoethanethiol (AET), and a subsequently deposited PSI multilayer film.

Five redox-active species are defined within the model in order to replicate PSI kinetics. PSI performs electron transfer reactions with external mediators at redox co-factors on its luminal and stromal termini—P_{700} and F_B, respectively. The photoactive reaction center, P_{700} incorporates three unique electronic states namely, a depleted ground state, a reduced ground state, and a photoexcited state, which we will refer to as D^+, D, and D^*, respectively. The photo-inert iron-sulfur cluster, F_B, incorporates just two unique electronic states namely, a depleted state and a reduced state, which we will refer to as A and A^-, respectively. Each PSI protein is assumed to contain a single reaction center and terminal iron-sulfur complex and thus, the following conservation relationships apply:

$$C_{D^+} + C_D + C_{D^*} = C_{PSI} \quad (1)$$

$$C_A + C_{A^-} = C_{PSI} \quad (2)$$

where C_{D+}, C_D, C_{D*}, C_A, and C_{A-} are the concentrations of D^+, D, D^*, A, and A^-, respectively. C_{PSI} is the concentration of PSI within the packed protein film. Scanning tunneling microscopy of PSI particles at gold surfaces indicates that individual PSI proteins pack as oblate spheroids with major and minor axes of 6 nm and 5 nm, respectively; therefore, we have modeled the concentration of PSI within the film, C_{PSI}, as 17.6 mM.[25] Prior to illumination ($t \leq 0$), electrons in PSI were assumed to reside only within ground states in P_{700} and so, initially, C_{D+}, C_{D*}, and C_{A-} are zero and C_D and C_A are equal to C_{PSI}.

The modeled electrolyte includes two diffusible species, *R* and *O*, that correspond to the reduced and oxidized form of the redox mediator, $[Fe(CN)_6]^{4-}$ and $[Fe(CN)_6]^{3-}$, respectively. The concentrations of *R* and *O*—C_R and C_O—are assumed to be uniform throughout the cell volume prior to illumination; these initial values are denoted as C_R^* and C_O^*, respectively.

Bulk Diffusion, ($x > H$)

Diffusion of *R* and *O* was modeled using Fick's second law,

$$\frac{\partial C_i}{\partial t} = D_i \frac{\partial^2 C_i}{\partial x^2} \quad (3)$$

where $C_i(x,t)$ is the concentration of diffusible mediator, i, at time, t, and distance, x, from the electrode surface. D_i is the diffusion coefficient of mediator i. D_R and D_O are assigned as 7.6×10^{-6} $cm^2 \cdot s^{-1}$and 6.5×10^{-6} $cm^2 \cdot s^{-1}$, respectively, based on reported values.[26]

Reaction-Diffusion in PSI Film, ($0 < x \leq H$)

We model a PSI film as a chemically reactive, porous structure of uniform thickness. To simulate solution-phase reactions of R and O with PSI's electronic termini, as well as the diffusional response of R and O to induced concentration gradients, we applied a expanded version of Fick's second law,

$$\frac{\partial C_i}{\partial t} = \emptyset_i D_i \frac{\partial^2 C_i}{\partial x^2} + r_{v,i} \tag{4}$$

where ϕ_i quantifies the modification of the diffusion coefficient of mediator i within the PSI film, the result of decreased volume for ion diffusion as well as electrostatic interactions with the charged proteins.[27] To establish values for ϕ_R and ϕ_O, a least squares fitting routine was applied to a numerical model established within the MATLAB partial differential equation solver, *pdepe* (**Figure 3.2**). The boundary conditions were (1) Butler-Volmer kinetics at the electrode surface (x=0) and (2) zero flux condition at the length of the cell $\left(\frac{dC_i}{dx} = 0\right)$, which was made long enough (2000 μm) such that concentrations were not altered at the far boundary for any applied potential used. Within the control volume, we formulated two regions. First, within the PSI film ($0 < x \leq H$), a modified version of Fick's second law was applied that included ϕ_i. No reactive term associated with PSI/mediator electron transfer reactions, $r_{v,i}$, was included since the

measurements were conducted in the dark. Second, the bulk electrolyte ($x > H$) was modeled using Fick's second law. The fitting routine utilized *fminsearch* to search for values of ϕ_R and ϕ_O that minimized the error between experimental and modeled chronoamperometry curves (90 s duration) at various applied bias (-200 mV, -100 mV, -50 mV, -10 mV, 10 mV, 50 mV, 100 mV, 200 mV).

$r_{v,i}$ is the rate of formation of mediator i due to chemical reaction in the PSI film. We formulate individual kinetic expressions for electron transfer reactions within PSI as well as between PSI co-factors and solution-phase mediators, R and O, in order to develop overall expressions for $r_{v,R}$ and $r_{v,O}$ (**Figure 3.3**).

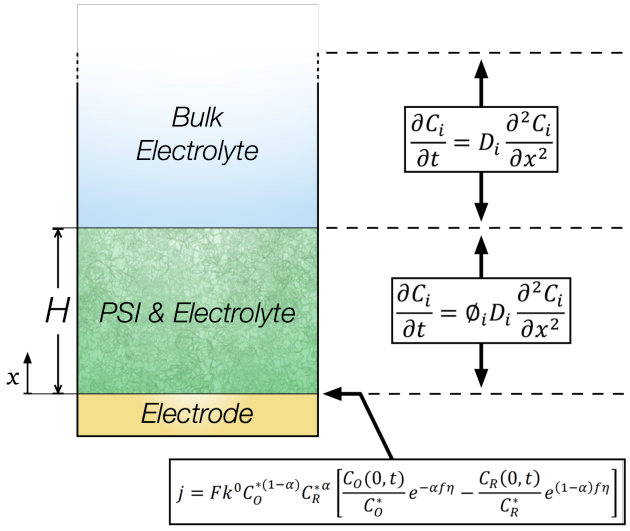

Figure 3.2. Layout and Pertinent Equations for Model Used to Extract Values of ϕ_i. Extended chronoamperometry at various applied bias of PSI multilayer films on Au/AET electrodes was performed to establish an experimental value for ϕ_R and ϕ_O which relate constraints on the diffusion coefficient due to free volume reduction and electrostatic interactions incurred by the dense protein film on the diffusion of redox ions, R and O. All tests were performed with a 0.65 μm-thick PSI multilayer film atop a Au/AET electrode that was immersed in an electrolyte containing 0.1 mM R, 0.1 mM O, 100 mM KCl, and 5 mM tris (pH 8.0). All tests were performed in the dark.

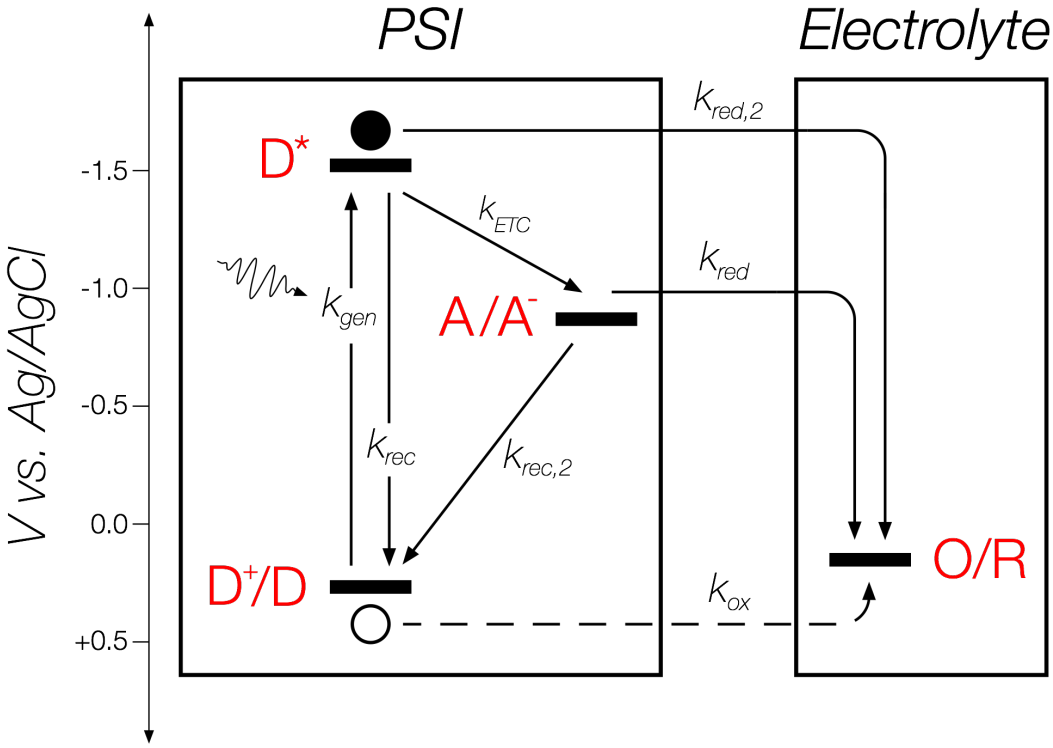

Figure 3.3. Model Energy Diagram. An energy diagram delineates the electronic states and electron transfer reactions used in the developed model. Five unique electronic states are employed to replicate the important functions of PSI's terminal co-factors, P_{700} and F_B, which include intramolecular electron photogeneration, recombination, and isolation as well as three charge-transfer reactions with diffusible mediators, R and O. ● and ○ denote an electron and hole generated due to a photoinduced charge separation event, respectively, within the PSI reaction center, P_{700}. Further, solid and dashed arrows represent the route of electron and hole transfer during a chemical reaction, respectively. The electrochemical potential indicated for the modeled PSI co-factors—D^+/D, D^*, A/A^-—reflect that of the equivalent natural co-factors—$P_{700}{}^+/P_{700}$, $P_{700}{}^*$, and $F_B/F_B{}^-$, respectively.

Intra-PSI Photogeneration

Electron transfer reactions between PSI proteins and mediators commence when electrons vacate PSI's low-energy states to occupy PSI's high-energy states. This process is precipitated by photogeneration, by which a photon excites an electron held within P_{700}. We model photogeneration as an intra-protein reaction,

$$D + h\nu \overset{k_{gen}}{\rightarrow} D^* \tag{5}$$

where k_{gen} is the proportionality constant for photogeneration that combines the true rate constant with fixed losses such as light intensity decay before striking the PSI film. The photocurrent magnitude generated by PSI multilayer films on metal electrodes is positively correlated with intensity of the light source[5] and thus, we have modeled the rate of photogeneration within a PSI multilayer film as proportional to the photon flux proximal to constituent proteins using a simple 1-D absorption model.

The emission intensity of the light source is expressed as a molar flux of photons ($mol \cdot cm^{-2} \cdot s^{-1}$)

$$N_{\lambda,s} = \frac{P\lambda}{hcN_A} \tag{6}$$

where N_A is the Avogadro constant, c is the speed of light, h is the Planck constant, P is the intensity of light emitted from the source (95 $mW \cdot cm^{-2}$), and λ is the wavelength of light absorbed by chlorophylls within the film (680 nm). Photon flux is a function of position, x, since the absorbance of chlorophylls embedded within the PSI multilayer film

will induce attenuation of photon flux as light travels from the film's furthest extent (x = H) to the electrode surface (x = 0). Furthermore, since we employed reflective gold electrodes in our experimental study, two contributions to total photon flux at x must be considered: a first pass due to direct irradiance from the light source and a second pass arising from electrode back-reflection (**Figure 3.4a**). The first pass of photons has a path length of (H-x), and therefore, its contribution to the spatially dependent photon flux is

$$N_{\lambda,1}(x) = N_{\lambda,s}\, 10^{-\varepsilon C_{chl}(H-x)} \tag{7}$$

where $N_{\lambda,1}(x)$ is the photon flux at position x due to the first pass, ε is the molar absorptivity of chlorophyll molecules bound within PSI (64 000 $M^{-1}\cdot cm^{-1}$),[16] C_{chl} is the concentration of chlorophyll within the film (84 mM, **Figure 3.5**), and H is the thickness of the PSI film. The second pass of photons has a path length of (H+x) due to a supplemental distance of 2x traveled. Assuming perfectly elastic reflection at the gold surface, the second-pass contribution to overall photon flux is

$$N_{\lambda,2}(x) = N_{\lambda,s}\, 10^{-\varepsilon C_{chl}(H+x)} \tag{8}$$

where $N_{\lambda,2}(x)$ is the photon flux at position x due to the second pass. The sum of the photon fluxes from the first and second passes provides the total photon flux with position,

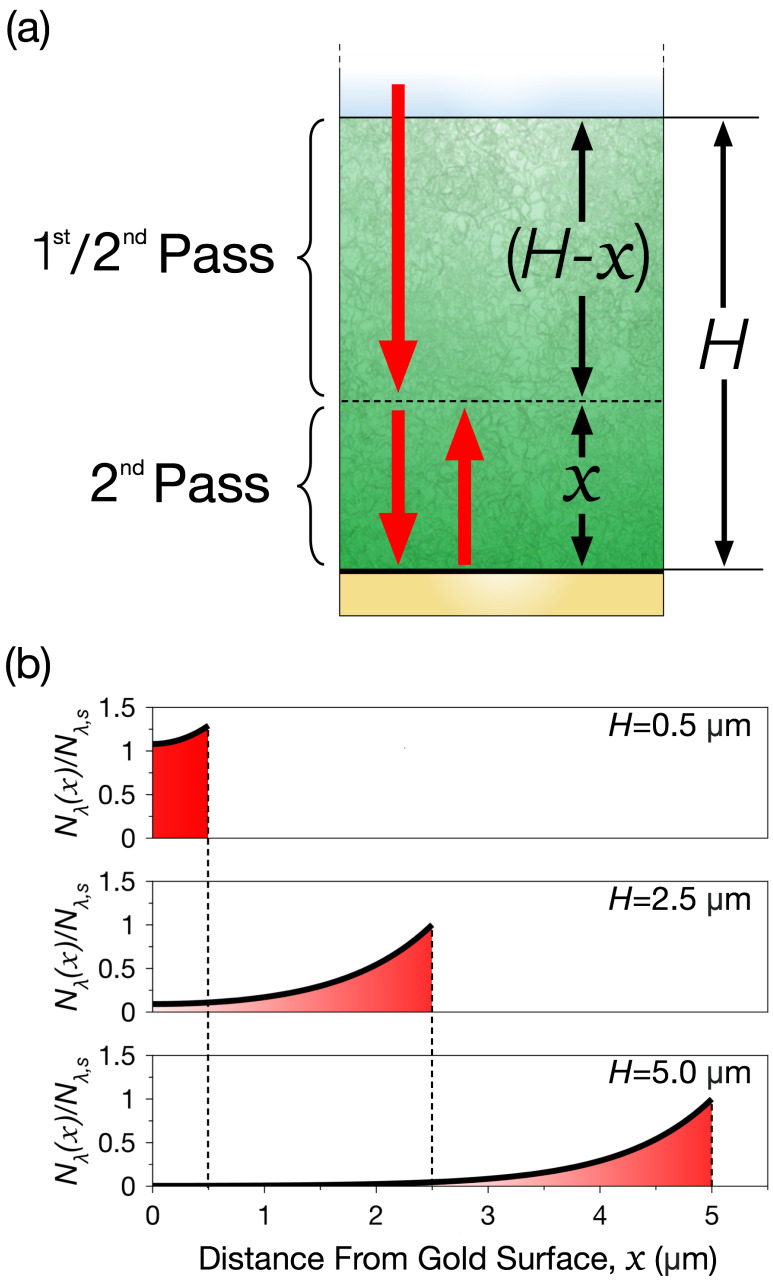

Figure 3.4. Absorption Model for Light Impinging on PSI Multilayer Films. Light absorption by embedded chlorophyll molecules causes decay in photon flux with progression into the PSI film. (a) Total photon flux includes contributions from initial photon entry into the film from the light source with a path length of (H-x) and subsequent back-reflection from the gold surface with a path length of (H+x). (b) An increase in PSI film thickness allows for increased incorporation of photon flux within the film but will eventually lead to only slight excitation of proteins near the electrode surface (x = 0). Plots of $N_\lambda/N_{\lambda,s,}(x)$ were produced assuming C_{chl} and ε of 84 mM and 64 000 $M^{-1}\cdot cm^{-1}$, respectively.

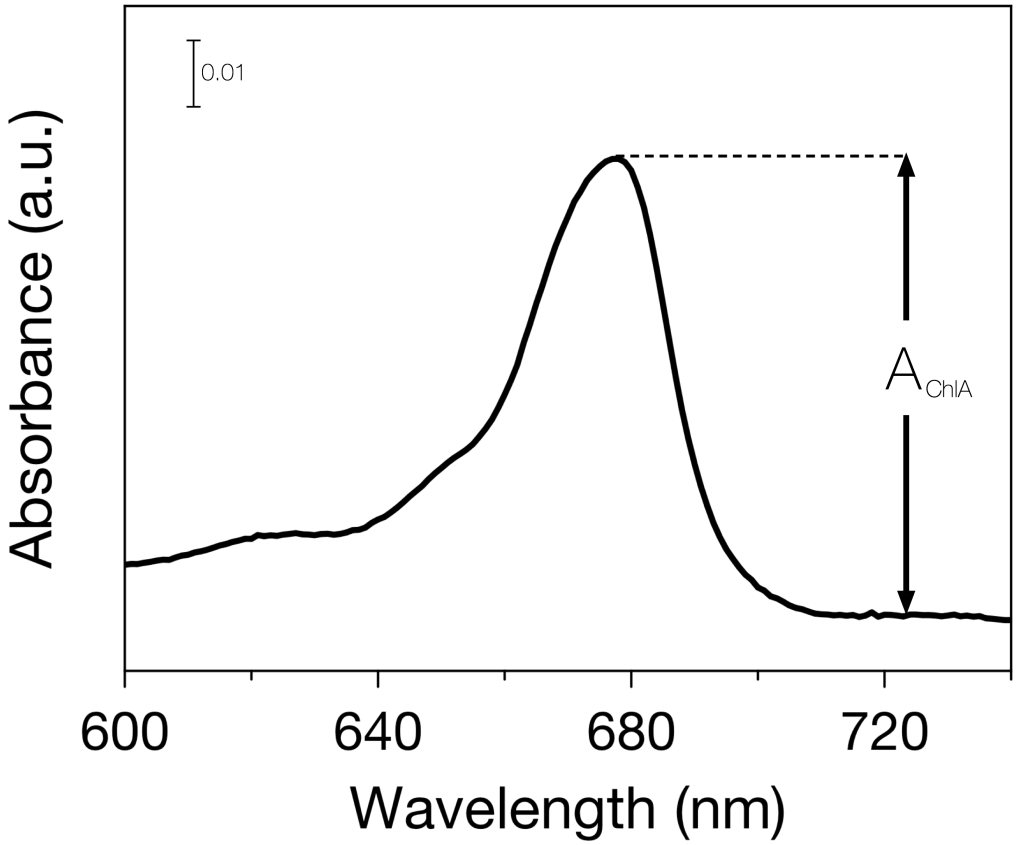

Figure 3.5. Solution Absorbance Used in C_{chl} Quantification. The concentration of chlorophyll in a PSI multilayer film, C_{chl}, was established *via* spectrophotometry of solutions used in drop casting by applying the Beer-Lambert Law to the absorbance peak of ChlA at 680 nm for PSI solutions that were diluted 50x. Above, we find this absorbance is 0.07, which equates to 84 mM in an undiluted PSI solution.

$$N_\lambda(x) = N_{\lambda,1}(x) + N_{\lambda,2}(x) \tag{9}$$

where $N_\lambda(x)$ is the total photon flux impinging on position x within the PSI film. According to this simple absorption model, a plot of $N_\lambda(x)/N_{\lambda,s}$ *vs.* x displays maximum photon flux at the film's extent and precipitous decay with progression to the electrode surface for all values of film thickness (**Figure 3.4b**). We incorporate local photon flux, $N_\lambda(x)$, into our overall expression for the rate of photogeneration,

$$r_{gen} = k_{gen} C_D N_\lambda(x) \tag{10}$$

Primary Recombination

Electrons residing within an excited reaction center, D^*, can recombine to their ground state *via*:

$$D^* \xrightarrow{k_{rec}} D \tag{11}$$

where k_{rec} is the rate constant for direct recombination. The expression for direct recombination is thus given as,

$$r_{rec}(x,t) = k_{rec} C_{D^*} \tag{12}$$

Intra-PSI Electron Transfer Chain

PSI's ETC permits an electron to navigate from luminal to stromal sides of the protein, and is made up of a series of five electron transfer reactions. We model this overall process as a second-order reaction,

$$D^* + A \xrightarrow{k_{ETC}} D^+ + A^- \tag{13}$$

where k_{ETC} is the rate constant corresponding to excited electron transport across PSI's ETC. The rate of electron transfer along the ETC is defined as,

$$r_{ETC} = k_{ETC}(C_{D^*})(C_A) \tag{14}$$

Secondary Recombination

While back electron transfer is not favored by the energetically downhill ETC, recombination has been observed for all steps along the ETC.[28] We incorporated this secondary recombination *via* a second-order reaction,

$$D^+ + A^- \xrightarrow{k_{rec,2}} D + A \tag{15}$$

where $k_{rec,2}$ is the kinetic constant for recombination of electrons along the ETC. The rate of secondary recombination is defined as,

$$r_{rec,2} = k_{rec,2}(C_{D^+})(C_{A^-}) \tag{16}$$

Electron Transfer Reactions between PSI and Diffusible Mediators

Concentration gradients for mediators, *R* and *O*, develop due to charge transfer reactions between PSI and mediators in the film. First, *R* can react with an oxidized reaction center, P_{700}^{+}, to produce *O* and a reduced reaction center, P_{700},

$$D^{+} + R \overset{k_{ox}}{\rightarrow} D + O \tag{17}$$

where k_{ox} is the corresponding rate constant. Second, after an electron is excited in P_{700} and traverses the ETC—reducing F_B—it can transfer to *O* in solution

$$A^{-} + O \overset{k_{red,1}}{\rightarrow} A + R \tag{18}$$

where $k_{red,1}$ is the rate constant. Third, P_{700}^{*} can donate its electron along the ETC but also react with O:

$$D^{*} + O \overset{k_{red,2}}{\rightarrow} D^{+} + R \tag{19}$$

where $k_{red,2}$ is the rate constant. The expressions for solution-phase reactions, $r_{v,R}$ and $r_{v,O}$ are now related as

$$r_{v,R} = -k_{ox}(C_R)(C_{D^{+}}) + k_{red1}(C_O)(C_{A^{-}}) + k_{red2}(C_O)(C_{D^{*}}) \tag{20}$$

$$r_{v,O} = -r_{v,R} \tag{21}$$

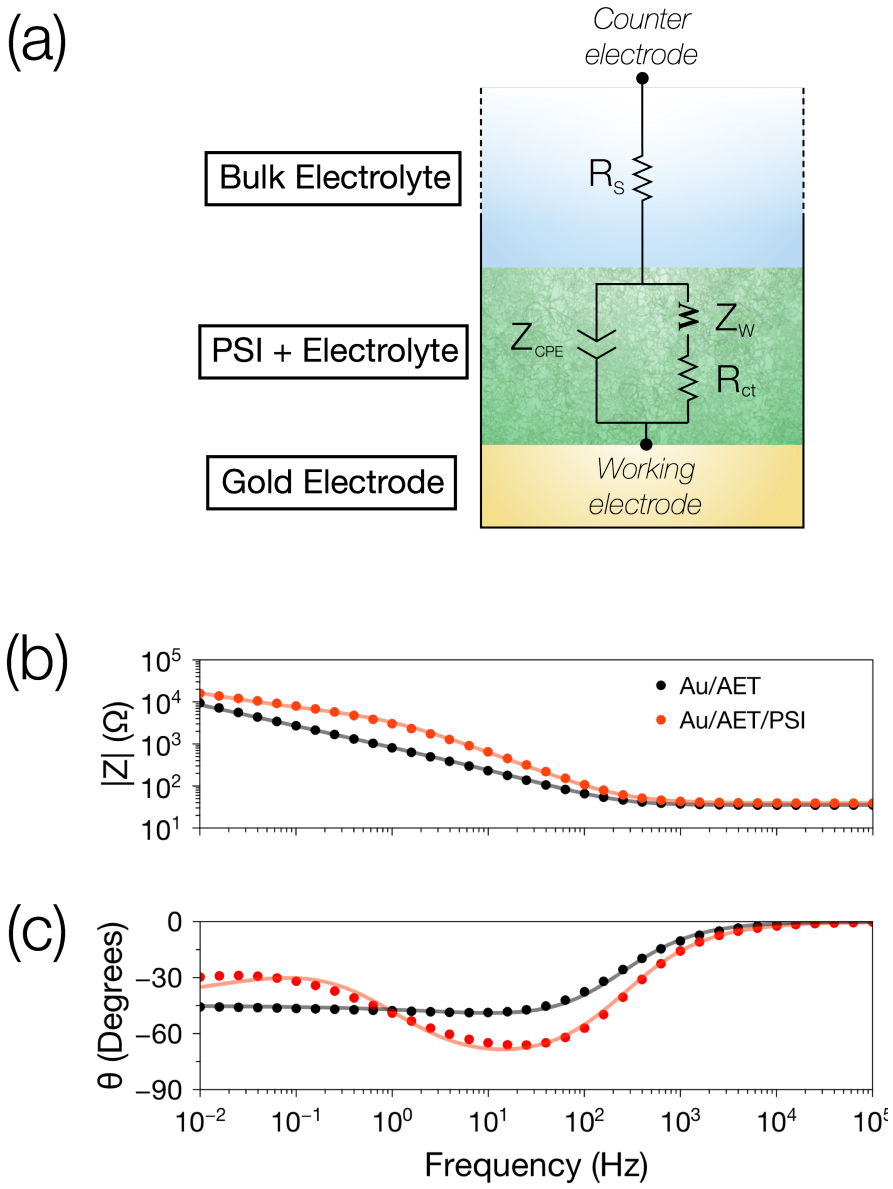

Figure 3.6. EIS for Determination of k^0 of Au/AET Electrodes Coated in a PSI Multilayer Film. (a) A Randles circuit model was used to determine the standard rate constant, k^0, of a Au/AET electrode coated by a PSI multilayer film. Plots of (b) magnitude and (c) phase angle versus frequency of a Au/AET electrode and a Au/AET/PSI electrode reveal significant differences. Bare electrodes have low R_{ct}, which is indicative of high k^0 (~.1 cm/s). The addition of a PSI multilayer occludes both the surface and the immediately surrounding volume of the electrode and thus incurs a significant increase in R_{ct} and corresponding increase in k^0 (5.0×10^{-4} cm/s). All EIS measurements were conducted using an aqueous electrolyte incorporating 0.1 mM $Fe(CN)_6^{4-}$, 0.1 mM $Fe(CN)_6^{3-}$, 100 mM KCl, and 5 mM tris (pH 8.0).

Heterogeneous Kinetics, (x = 0)

The electrode/solution interface was modeled using Butler-Volmer reversible electrode kinetics as[26]

$$j = Fk^0 C_O^{*(1-\alpha)} C_R^{*\alpha} \left[\frac{C_O(0,t)}{C_O^*} e^{-\alpha f \eta} - \frac{C_R(0,t)}{C_R^*} e^{(1-\alpha) f \eta} \right] \quad (22)$$

where j is current density, F is the Faraday constant (96,485 C/mol), k^0 is the standard rate constant (cm/s), f is nF/RT (25.693 mV^{-1}) where R is the universal gas constant and T is temperature in Kelvin, and η is overpotential—the bias supplied by the potentiostat relative to the cell's electrochemical equilibrium. $C_O(0,t)$ and $C_R(0,t)$ are the concentrations of R and O at the electrode/solution interface ($x = 0$), respectively, and α is the transfer coefficient that quantifies the symmetry of the free energy barrier between the forward and reverse heterogeneous reaction. As is convention, α was assumed to be 0.5—implying free energy parity—in lieu of rigorous assessment.[26] k^0 for a PSI multilayer-coated electrode was measured to be 5×10^{-4} cm/s using electrochemical impedance spectroscopy (EIS) (**Figure 3.6**).

Results and Discussion

Photocurrent with R and O Concentration

A comprehensive investigation of photocurrent generation from a PSI multilayer film immersed in electrolytes containing variable C_R^*/constant C_O^* and variable C_O^*/constant C_R^* was conducted (**Figure 3.7**). When C_R^* is held constant, an increase in

C_O^* promotes an increase in photocurrent. Specifically, with C_R^* fixed at 0.1 mM, anodic photocurrent is observed to increase from 0.2 μA/cm^2 to a plateau value of 1.5 μA/cm^2 for an increase in C_O^* from 0.01 mM to 100 mM. Furthermore, when C_O^* is held constant, an increase in C_R^* causes a decrease in photocurrent. In particular, with C_O^* fixed at 0.1 mM, anodic photocurrent decreases from 0.7 μA/cm^2 to below 0.1 μA/cm^2 for an increase in C_R^* from 0.01 mM to 100 mM. Both observed kinetic trends contradict those expected for a photocell in which DET is prevalent. If PSI-electrode DET was the dominant mechanism, increased C_R^* would facilitate resupply of electrons to depleted PSI ground states, promoting light-driven charge transfer reactions into the electrode and ultimately in an increase in anodic photocurrent. Furthermore, increased C_O^* would increase the rate of electron transfer reactions between PSI's high-energy states and O to curb the overall rate of DET into the electrode, lowering anodic photocurrent. These contradictory kinetic trends are thus critical evidence for the hypothesis that MET underlies photocurrent generation from a PSI multilayer film in contact with solubilized mediators.

The observed trends in photocurrent with mediator concentration are attributed to saturation/inhibition of light-driven reaction rates within the PSI film and thus, are fitted using the Michaelis-Menten model of enzyme kinetics as has been done previously for similar PSI-based assemblies.[22] A steady-state electron balance at the electrode surface yields

$$j \cong F\left[\frac{V_{m1}C_O^*}{K_{M1}\left(1+\frac{C_R^*}{K_{i1}}\right)+C_O^*}+\frac{V_{m2}C_O^*}{K_{M2}\left(1+\frac{C_R^*}{K_{i2}}\right)+C_O^*}-\frac{V_{m3}C_R^*}{K_{M3}\left(1+\frac{C_O^*}{K_{i3}}\right)+C_R^*}\right] \quad (23)$$

where V_{m1}, V_{m2}, and V_{m3} are the maximum charge transfer rates of P_{700}^*, F_B^-, and P_{700}^+ with the solubilized mediators O, O, and R, respectively. K_{M1}, K_{M2}, and K_{M3} are the concentrations of O, O, and R for which half of the maximum charge transfer rate with P_{700}^*, F_B^-, and P_{700}^+ is achieved, respectively. K_{i1}, K_{i2}, and K_{i3} are the equilibrium constants related to inhibition phenomena, whereby R, R, and O reduce charge transfer rates through formation of non-reactive coupled states. A least squares regression analysis was used to fit the photocurrent *vs.* concentration data for both the case of C_R^* constant and C_O^* constant, and the obtained values (**Table 3.1**) permit a highly representative, simultaneous fit (**Figure 3.7**).

Table 3.1. Michaelis-Menten Parameters Extracted from Photocurrent *vs.* Mediator Concentration Statistical Data

Parameter	Value	Units
V_{m1}	1.0	$\mu mol \cdot cm^{-2} \cdot s^{-1}$
K_{M1}	0.11	$\mu mol \cdot cm^{-3}$
K_{i1}	0.01	$\mu mol \cdot cm^{-3}$
V_{m2}	0.40	$\mu mol \cdot cm^{-2} \cdot s^{-1}$
K_{M2}	0.02	$\mu mol \cdot cm^{-3}$
K_{i2}	3.3	$\mu mol \cdot cm^{-3}$

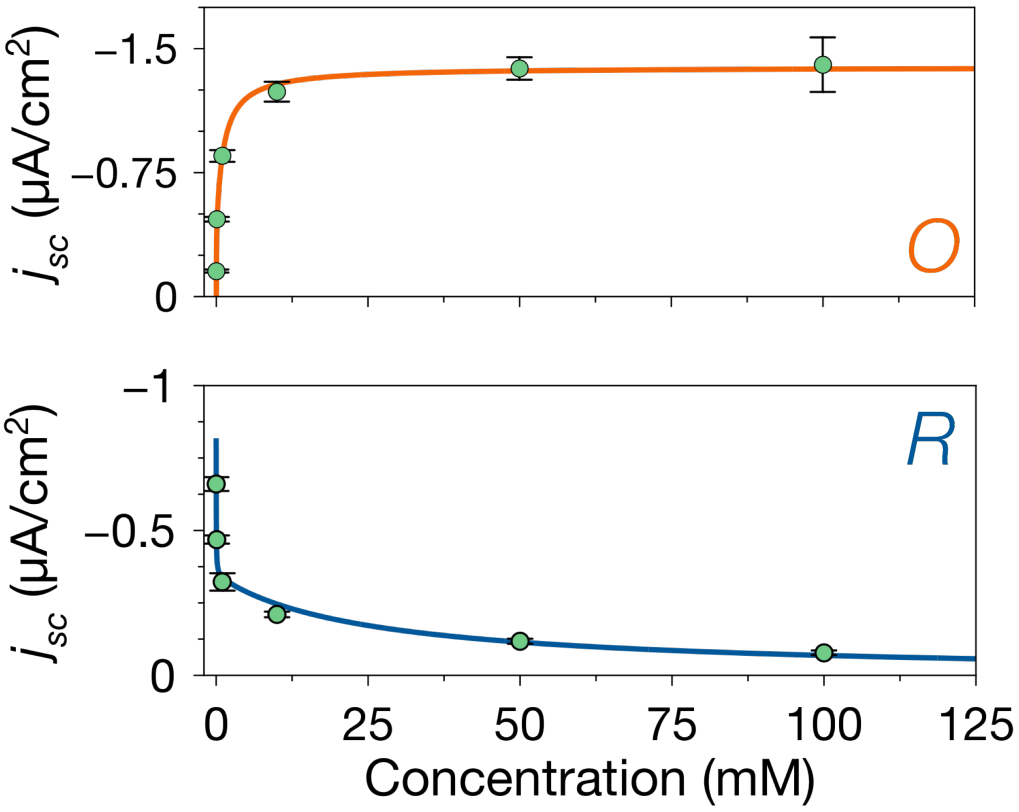

Figure 3.7. PSI Multilayer Photocurrent Trends with Mediator Concentration. Photocurrent generation from a PSI multilayer is enhanced with increased ratio of C_O^* to C_R^* (and vice versa). We employ a single Michaelis-Menten expression to simultaneously fit photocurrent progression for C_R^* constant and C_O^* variable (top, $R^2 = 0.99$) and C_O^* constant and C_R^* variable (bottom, $R^2 = 0.99$). Data were obtained for independently assembled cells that included a 0.65 μm-thick PSI multilayer film atop a Au/AET electrode that was immersed in an electrolyte containing 0.1 mM R (or O), 100 mM KCl, 5 mM tris, and an as-specified concentration of O (or R) as specified (pH 8.0).

Therefore, increased C_O^* augments the rates of electron transfer reactions between PSI's high-energy electronic states—F_B^- and P_{700}^*—and O (eqn. 18 and eqn. 19), facilitating more rapid generation of R within the PSI film (eqn. 20). This process elevates $C_R(0,t)$ and thus, increases the rate of heterogeneous reaction that is the basis for an anodic photocurrent response (eqn. 22). The limiting rates are dictated by the formation of intermediate, coupled states: O/F_B^- and O/P_{700}^*. In contrast, due to the generally low rate of charge transfer between R and P_{700}^+—V_{m3} was found to be nearly zero—increased C_R^* predominately facilitates the formation of non-reactive coupled states—R/F_B^- and R/P_{700}^*—rather than the enhancement of light-driven production of C_O^* in the film. This inhibition mechanism results in photocurrent decay to zero rather than to a cathodic (positive) value.

Numerical Fit of Time-Resolved Photocurrent and Simulation of Concentration Profiles

The values of constants obtained from the numerical fitting routine (**Table 3.2**) permit accurate replication of time-resolved photocurrent during a chronoamperometic experiment (**Figure 3.8a**), and the optimized numerical model is used to simulate concentrations of R and O with distance from the electrode surface—$C_R(x,t)$ and $C_O(x,t)$, respectively (**Figure 3.8b**, **Figure 3.9**). Specifically, the model projects that during illumination, electrons held initially in P_{700} are rapidly transferred to excited states, F_B^- and P_{700}^*, prompting charge transfer reactions between PSI co-factors and diffusible mediators (eqn. 17, eqn. 18, and eqn. 19). The overall rate of mediator reduction by PSI outpaces that of mediator oxidation by PSI (i.e. $r_{v,R} > 0$) and thus, an equivalent increase and decrease in C_R and C_O, respectively, occurs within the PSI film. Specifically, the

fitted model predicts an increase and decrease of ~6 μM in C_R and C_O within a 0.65 μm-thick PSI multilayer film, respectively, representing a 6% change in concentration of either mediator. This concentration change shifts the proximal electrode surface out of electrochemical equilibrium, and electrons are transferred into the electrode *via* heterogeneous reaction that defines the observed photocurrent (eqn. 22). Furthermore, the net conversion of O to R within the PSI film stimulates a compensating diffusional response, which transports R from within the PSI film to the bulk solution and O from the bulk solution to within the PSI film. After the light source is turned off, photogeneration ceases (r_{gen}=0) and consequently, the rate of electron transfer from PSI to mediators rapidly decreases ($r_{v,R}\rightarrow 0$). However, due to diffusion during illumination, C_R and C_O remain elevated and diminished, respectively, many hundred micrometers into the bulk solution and thus, current attenuation to zero post-illumination is limited by the heterogeneous oxidation of residual *R*.

Table 3.2. Intra-Film Kinetic Constants Fitted from Chronoamperometric Data

Parameter	Value	Units
k_{gen}	1.2	$cm^2 \cdot \mu mol^{-1}$
k_{rec}	970	s^{-1}
k_{ETC}	270	$cm^3 \cdot \mu mol^{-1} \cdot s^{-1}$
$k_{rec,2}$	8.4×10^{-3}	$cm^3 \cdot \mu mol^{-1} \cdot s^{-1}$
k_{ox}	2.6×10^{-4}	$cm^3 \cdot \mu mol^{-1} \cdot s^{-1}$
k_{red}	1.4×10^{-2}	$cm^3 \cdot \mu mol^{-1} \cdot s^{-1}$
$k_{red,2}$	1.3×10^{3}	$cm^3 \cdot \mu mol^{-1} \cdot s^{-1}$

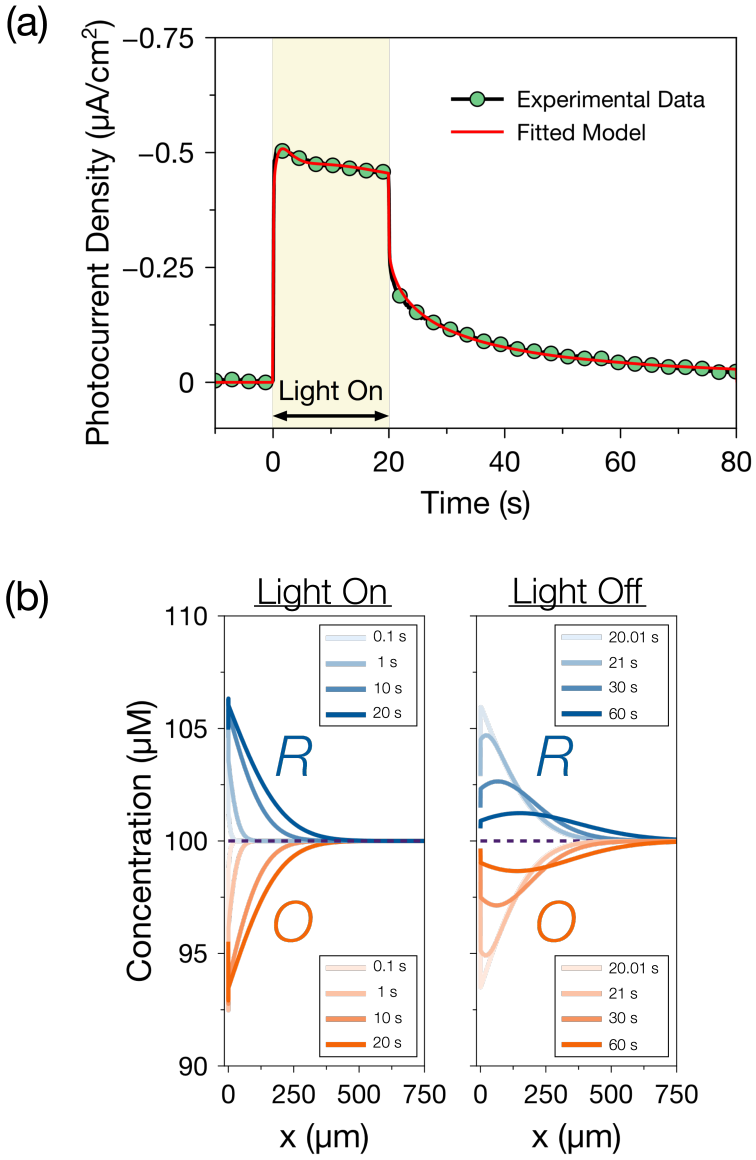

Figure 3.8. Results of Fitting Routine. An electrochemical reaction-diffusion model—based strictly on MET *via* reversible mediators—replicates photocurrent generated from PSI multilayers, and permits simulation of concentration profiles along the length of the electrochemical cell. (a) The phenomenological model simulates a time-resolved photocurrent experiment with high representation. (b) Simulations of concentration profiles of R and O during and after cell illumination suggest that PSI multilayer assemblies modify mediator concentration several hundred micrometers distant from the film surface, and that this effect continues post-illumination. The experimental photocurrent profile was measured from a 0.65 μm-thick PSI multilayer atop Au/AET that was immersed in an aqueous electrolyte incorporating 0.1 mM $Fe(CN)_6^{4-}$, 0.1 mM $Fe(CN)_6^{3-}$, 100 mM KCl, and 5 mM tris (pH 8.0).

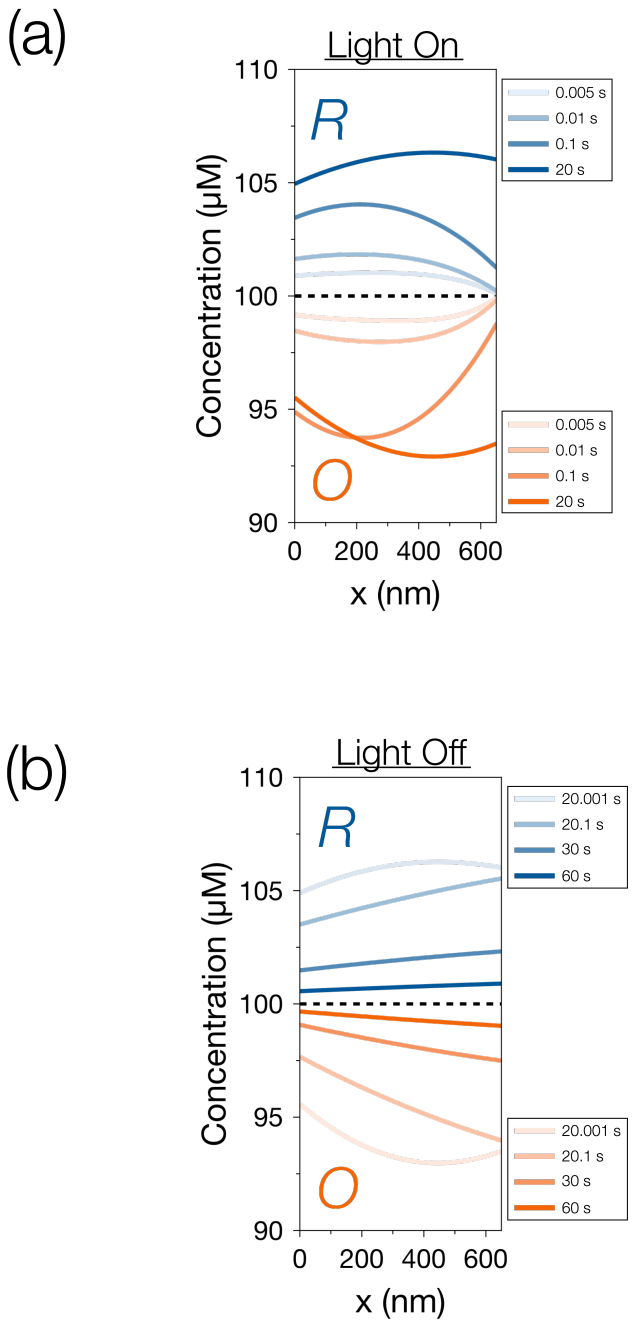

Figure 3.9. Simulated Mediator Concentration Profiles within a PSI Multilayer Film. Simulated concentration profiles of mediators—R and O—within a PSI multilayer film during a photochronoamperometric experiment. (a) Simulated mediator concentration profiles during illumination. (b) Simulated mediator concentration profiles after the light source is turned off. The data in this figure was generated from the fitted model presented in Figure 5 of the main text. The thickness of the PSI multilayer film is 0.65 μm, C_R^* = 0.1 mM, and C_O^* = 0.1 mM.

Simulation of Photocurrent with Overpotential

The fitted model accurately simulates chronoamperometry curves (**Figure 3.10a**) and photocurrent magnitudes (**Figure 3.10b**) for cells under applied bias. In each chronoamperometric experiment, a selected overpotential, η, was applied. In an initial 100 s period without illumination, the electrode drives current according to eqn. 22—anodic for $\eta > 0$, cathodic for $\eta < 0$, and zero for $\eta = 0$ (equilibrium potential). Thus, overpotential stimulates a change in mediator concentration within the PSI film prior to illumination—C_O/C_R increases for $\eta > 0$, decreases for $\eta < 0$, and remains the same for $\eta = 0$—and the photocurrent measured during the subsequent 20 s period of illumination reflects this change due to the kinetics of PSI/mediator reactions in the multilayer film. As shown in **Figure 3.7**, an increase and decrease in C_O/C_R drives increased and decreased anodic photocurrent, respectively. Since the electrolyte is composed of 0.1 mM *R* and 0.1 mM *O*, the overpotential supplied can at most provide for 0.2 mM of either *R* or *O* within the PSI film. Therefore, the modification of PSI multilayer photocurrent based on overpotential has a fundamental upper and lower bound: for the case of high positive overpotential (0.2 mM *O* in the film) and high negative overpotential (0.2 mM *R* in the film), respectively.

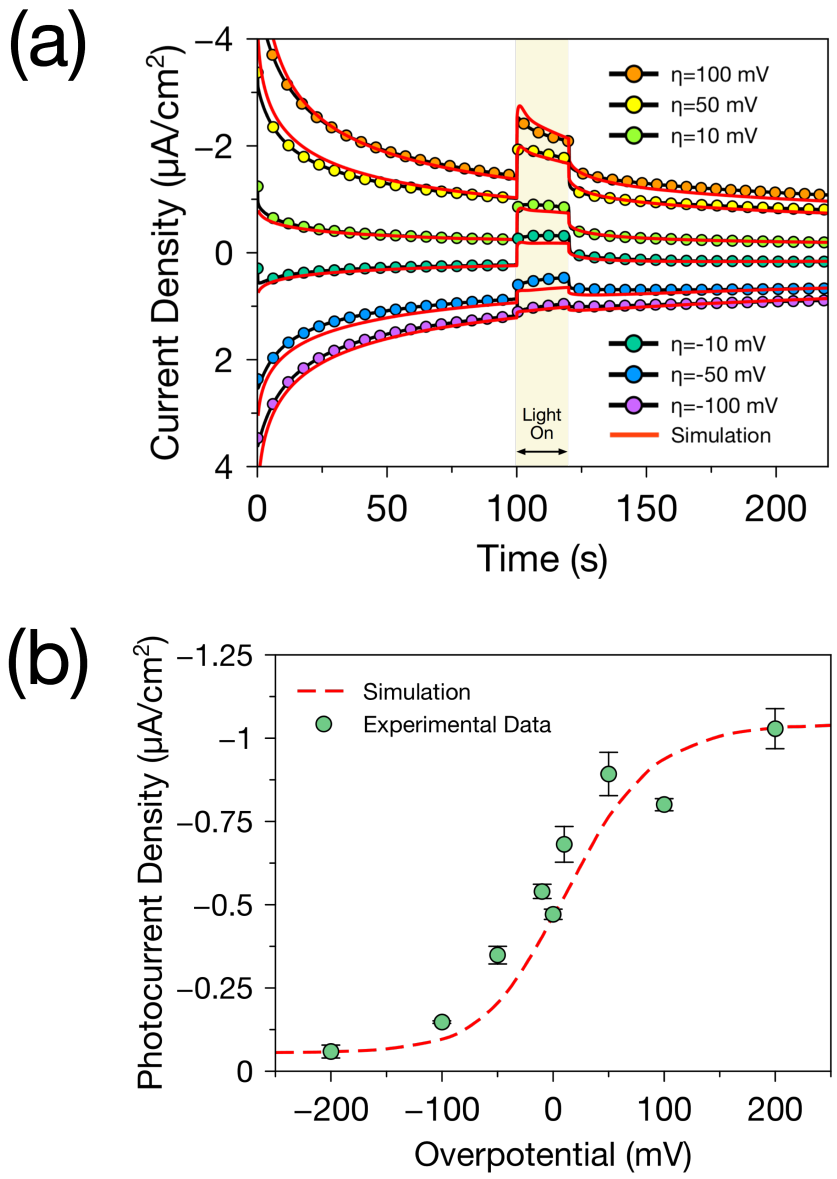

Figure 3.10. Simulation of PSI Multilayer Photocurrent with Overpotential. (a) The developed phenomenological model accurately simulates photocurrent under applied bias. Negative ($\eta < 0$) and positive ($\eta > 0$) overpotential facilitate photocurrent of lower and higher magnitude relative to that at zero overpotential ($\eta = 0$), respectively. This effect is due to changes in mediator concentrations—C_R and C_O—within the PSI film due to Butler-Volmer electrode kinetics modifying the rates of PSI/mediator electron transfer reactions that lead to anodic photocurrent development. (b) Simulated photocurrent *vs.* overpotential accurately reproduces experimental data ($R^2 = 0.88$) For all experimental data shown, the working electrode consisted of a 0.65 μm-thick PSI multilayer atop Au/AET that was immersed in an aqueous electrolyte incorporating 0.1 mM $Fe(CN)_6^{4-}$, 0.1 mM $Fe(CN)_6^{3-}$, 100 mM KCl, and 5 mM tris (pH 8.0). The dark equilibrium potential was 0.26 V *vs*. Ag/AgCl.

Simulation of Photocurrent with PSI Multilayer Thickness

Consistent with previous studies, the photocurrent generated from a PSI multilayer film is observed to be a strong function of film thickness,[16,29] and we subdivide the photocurrent *vs.* thickness behavior as a region of photocurrent increase and a subsequent region of photocurrent saturation (**Figure 3.11**, green data points). In particular, we observe an increase in anodic photocurrent from 0 $\mu A/cm^2$ to 0.84 $\mu A/cm^2$ as PSI film thickness is increased from 0 μm to 1.3 μm. This effect is due to the increased amount of PSI in thicker films; additional proteins provide supplemental electron density (1 electron/protein) for electron transfer reactions between PSI co-factors and mediators that contribute to augmented change in mediator concentrations at the electrode surface and increased photocurrent (eqn. 22). However, for PSI film thickness in excess of 1.3 μm, we observe a photocurrent plateau of approximately 0.8 $\mu A/cm^2$. This effect is attributed to the absorbance of chlorophyll molecules embedded within each PSI protein that enforce a fundamental upper limit to the magnitude of photon flux available to the inner regions of thicker PSI multilayer films (**Figure 3.4**). The fitted model simulates the shape of the observed photocurrent *vs.* film thickness profile well, predicting a maximum photocurrent that is 80% of that from experiment (**Figure 3.11**, red curve). In contrast, when our model is retooled to incorporate a spatially static photon flux ($N_\lambda = N_{\lambda,s}$), it does not exhibit photocurrent saturation behavior and thus provides a significant over-estimate of photocurrent for thicker PSI films (**Figure 3.11**, black curve).

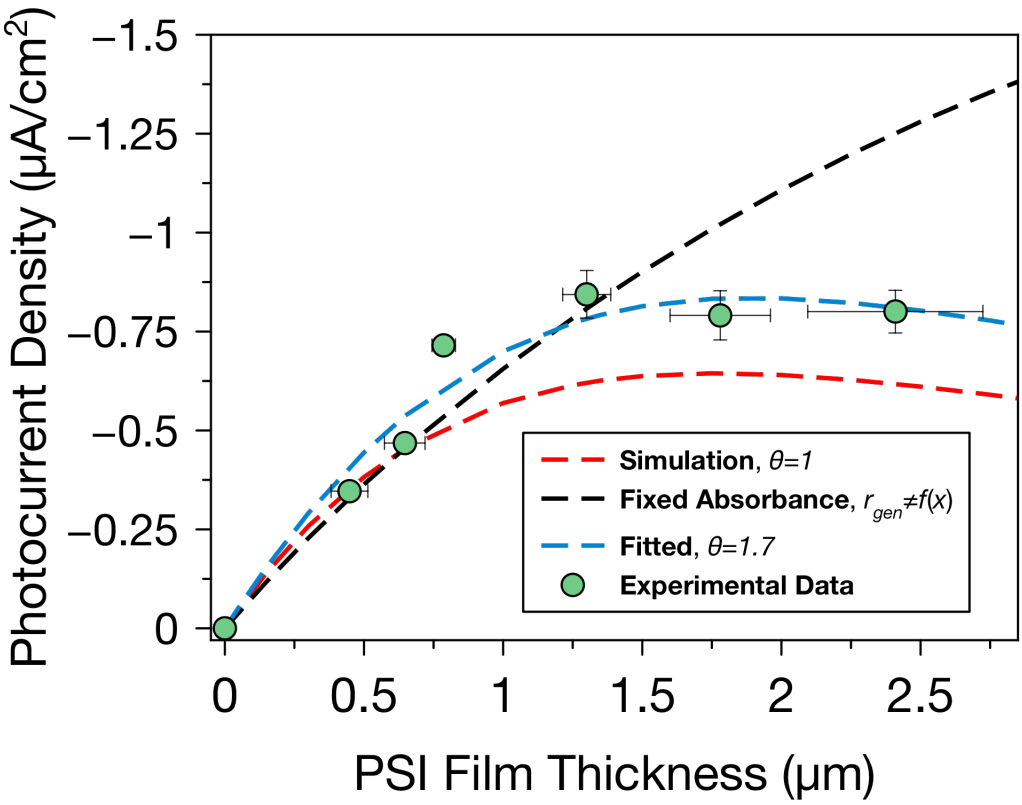

Figure 3.11. Simulation of PSI Multilayer Photocurrent with Variable Film Thickness. Photocurrent density is observed to increase with supplemental PSI thickness until saturation for $H > 1.3$ μm (green). By incorporating a spatially dependent photon flux term within the overall rate expression for photogeneration, the reaction-diffusion model closely simulates the overall photocurrent *vs*. film thickness trend (red curve, $R^2 = 0.75$). In contrast, if r_{gen} is not spatially dependent, the model does not predict photocurrent saturation and thus significantly over-predicts photocurrent for thicker PSI films (black curve, $R^2 = 0.50$). By incorporating the scaling factor, θ—that approximates film-based Rayleigh scattering and photon re-emission—to the expression for r_{gen} the model can accurately represent the photocurrent response for thicker PSI films (blue curve, $R^2 = 0.96$). All photocurrents were measured from cells that included a PSI multilayer film of specified thickness atop Au/AET and immersed in an aqueous electrolyte incorporating 0.1 mM $Fe(CN)_6^{4-}$, 0.1 mM $Fe(CN)_6^{3-}$, 100 mM KCl, and 5 mM tris (pH 8.0).

Finally, we ascribe the under-prediction of photocurrents of our fitted model to the absence of an accounting for Rayleigh scattering from PSI particles and photon re-emission from chlorophyll molecules embedded within the film, which would augment the film-resident photon flux relative to that permitted by our simple absorption model (**Figure 3.4**). We have approximated this effect by applying a scaling factor, θ, to the previously developed expression for r_{gen}:

$$r_{gen}(x,t) = \theta k_{gen} C_{P_{700}} N_{\lambda}(x) \tag{24}$$

With all constants from **Table 3.1** fixed, we utilized a least squares fitting routine to find that θ=1.7 permits an accurate representation of photocurrent for thicker films (**Figure 3.11**, blue curve).

Conclusions

We have formulated and optimized an electrochemical reaction-diffusion model to replicate MET-based photocurrent generation from a PSI multilayer film atop a metal electrode that is exposed to diffusible redox mediators. The model was fitted to experimental photocurrent data and then used to predict concentration profiles during and after cell illumination. Additionally, the model accurately simulates photocurrent production for cells under positive and negative applied bias. Furthermore, by incorporating photon flux decay along the path of illumination due to intra-film chlorophyll absorbance, the model replicates the observed photocurrent saturation for PSI multilayer films of sufficient thickness. A key prediction of this computational study is

that the diffusion of mediators in response to electron transfer reactions within a photoresponsive PSI film quickly alters mediator concentrations many hundred micrometers away from the film's furthest extent. This phenomenon could be harnessed in coupled systems in which the mediator concentration perturbation afforded by a PSI multilayer film is used to modify the rates of electrochemical reactions in distant regions of a combined electrochemical assembly—such as curbing recombination rates within a physically separated photoanode of a dye-sensitized solar cell. The MATLAB-based computational framework provided herein is an accessible foundation for electrochemical analysis of multilayer films of a wide library of chemically reactive proteins, and is suitable for future modeling studies of charge transfer in composite films containing PSI and an electrically conductive scaffold that may include redox hydrogels, intrinsically conductive polymers, or oxidoreductases.

Experimental Methods

PSI Extraction

PSI was extracted from spinach leaves using a previously described procedure,[30] and dialysis was performed to reduce salt and surfactant concentrations.[16] Succinctly, baby spinach leaves were de-veined, immersed in buffer, and then macerated using a blender. Resulting solutions were centrifuged at 8 000 g to pellet out thylakoid membranes, which were lysed by subsequent exposure to aqueous Triton X-100. The resulting solution was centrifuged at 20 000 g, and the resulting supernatant was carefully added to the top of a hydroxylapatite column at 4 °C. Column chromatography as described by Shiozawa et. al. was performed to procure a purified PSI solution.[31] This

solution was divided into 1 mL aliquots and stored at -80 °C. Dialysis was performed for 12 h using 10 000 MWCO dialysis tubing (Spectrum Labs). Using the method of Baba et. al., the concentration of P_{700} was determined to be 1 μM with 45 chlorophylls per reaction center.[32]

Electrode Preparation

Sequential thermal deposition of chromium (10 nm) and gold (125 nm) was used to prepare a gold surface atop a <100> silicon support. Next, these substrates were cut into 1.4 cm x 2.5 cm pieces, rinsed vigorously in water and ethanol, dried under a stream of N_2, and placed in an ethanol solution containing 1 mM aminoethane thiol (AET, Acros). Gold electrodes were left in AET solutions for 12 h to prepare a hydrophilic surface for subsequent drop casting.

PSI Multilayer Assembly

Gold electrodes immersed in AET solution were removed, rinsed in ethanol, and dried with a stream of N_2. Hole-punched plater's tape was applied to the surface of the AET-modified gold to provide a confined area for drop casting (0.28 cm^2). 30 μL of dialyzed PSI solution was deposited into this mask, and the sample was placed under vacuum to evaporate water and leave behind a multilayer film. To provide for thinner PSI films, volumes less than 30 μL were applied; thicker films were assembled by sequential deposition of 30 μL of PSI solution, as described previously.[16] Assembled films were placed in a petri dish that was subsequently covered in aluminum foil.

Chronoamperometric Characterization

A CHI660A potentiostat with a three-electrode assembly was used to perform photochronoamperometry (PCA) of PSI films. A PSI-coated gold electrode served as the working electrode. A platinum mesh counter electrode and a Ag/AgCl reference electrode were used in all measurements. A 250 W cold light source (Leica KL 2500 LCD, 140 mW/cm^2) providing a 380-790 nm spectral emission was used. An optical low-pass filter with a 633 nm cutoff (95 mW/cm^2) was applied to narrow the spectral window for red light illumination for all PCA experiments. Unless otherwise specified, PCA measurements were performed using an aqueous electrolyte containing 0.1 mM $K_4Fe(CN)_6$, 0.1 mM $K_3Fe(CN)_6$, 100 mM KCl, and 5 mM tris buffer adjusted to pH 8.0 by dropwise addition of 1 M HCl. An open circuit potential measurement (400 s) was used to determine the equilibrium potential of the cell. For measurements under zero applied bias, the measured equilibrium potential was applied during a subsequent chronoamperometric experiment. Values different than the equilibrium potential were applied to enforce a selected overpotential. All PCA experiments were 400 s in duration with red light illumination from 100 s to 120 s.

Electrochemical Impedance Spectroscopy (EIS)

A Gamry Instruments CMS300 impedance system was used for all EIS experiments. A three-electrode setup was used, including a Ag/AgCl reference electrode and a platinum counter electrode, and a film-contacted gold electrode serving as the working electrode. As described in the PSI multilayer preparation procedure, the electrochemically accessible area was constrained to 0.28 cm^2. EIS measurements were

performed in a redox electrolyte incorporating 0.1 mM $K_4Fe(CN)_6$, 0.1 mM $K_3Fe(CN)_6$, 100 mM KCl, and 5 mM tris buffer adjusted to pH 8.0 by dropwise addition of HCl.

Profilometry

PSI multilayer thickness was assessed on gold electrode surfaces using a Veeco DEKTAK 150 profilometer with an applied force of 3 mg and scan rate of 0.012 cm/s. For each sample, the plater's tape mask was removed and a line scan was conducted through the center of the film and spanned from approximately 500 μm to the proximal edge of the film to approximately 500 μm from the far edge of the film.

Works Cited

(1) Alberts, B.; Bray, D.; Hopkin, K.; Johnson, A.; Lewis, J.; Raff, M.; Roberts, K.; Walter, P. *Essential Cell Biology*, 3rd ed.; Garland Science: New York, 2010.

(2) Golbeck, J. H. Structure, Function and Organization of the Photosystem I Reaction Center Complex. *Biochim. Biophys. Acta* **1988**, *895*, 167–204.

(3) Nelson, N.; Yocum, C. F. Structure and Function of Photosystems I and II. *Annu. Rev. Plant Biol.* **2006**, *57*, 521–565.

(4) Iwuchukwu, I. J.; Vaughn, M.; Myers, N.; Neill, H. O.; Frymier, P.; Bruce, B. D. Self-Organized Photosynthetic Nanoparticle for Cell-Free Hydrogen Production. *Nat. Nanotechnol.* **2010**, *5*, 73–79.

(5) Ciesielski, P. N.; Hijazi, F. M.; Scott, A. M.; Faulkner, C. J.; Beard, L.; Emmett, K.; Rosenthal, S. J.; Cliffel, D.; Jennings, G. K. Photosystem I - Based Biohybrid Photoelectrochemical Cells. *Bioresour. Technol.* **2010**, *101*, 3047–3053.

(6) Manocchi, A. K.; Baker, D. R.; Pendley, S. S.; Nguyen, K.; Hurley, M. M.; Bruce, B. D.; Sumner, J. J.; Lundgren, C. A. Photocurrent Generation from Surface Assembled Photosystem I on Alkanethiol Modified Electrodes. *Langmuir* **2013**, *29*, 2412–2419.

(7) Gizzie, E. A.; LeBlanc, G.; Jennings, G. K.; Cliffel, D. E. Electrochemical Preparation of Photosystem I-Polyaniline Composite Films for Biohybrid Solar Energy Conversion. *ACS Appl. Mater. Interfaces* **2015**, *7*, 9328–9335.

(8) Gizzie, E. A.; Scott Niezgoda, J.; Robinson, M. T.; Harris, A. G.; Jennings, G. K.; Rosenthal, S. J.; Cliffel, D. E. Photosystem I-polyaniline/TiO_2 Solid-State Solar Cells: Simple Devices for Biohybrid Solar Energy Conversion. *Energy Environ. Sci.* **2015**, *8*, 3572–3576.

(9) Mershin, A.; Matsumoto, K.; Kaiser, L.; Yu, D.; Vaughn, M.; Nazeeruddin, M. K.; Bruce, B. D.; Grätzel, M.; Zhang, S. Self-Assembled Photosystem-I Biophotovoltaics on Nanostructured TiO2 and ZnO. *Sci. Rep.* **2012**, *2*, 1–7.

(10) Gordiichuk, P. I.; Wetzelaer, G.-J. A. H.; Rimmerman, D.; Gruszka, A.; de Vries, J. W.; Saller, M.; Gautier, D. A.; Catarci, S.; Pesce, D.; Richter, S.; et al. Solid-State Biophotovoltaic Cells Containing Photosystem I. *Adv. Mater.* **2014**, *26*, 4863–4869.

(11) Robinson, M. T.; Gizzie, E. A.; Mwambutsa, F.; Cliffel, D. E.; Jennings, G. K. Mediated Approaches to Photosystem I-Based Biophotovoltaics. *Curr. Opin. Electrochem.* **2017**, 1–7.

(12) Plumeré, N.; Nowaczyk, M. M. Biophotoelectrochemistry of Photosynthetic Proteins; Springer Berlin: Berlin, Heidelberg, 2016; pp 1–26.

(13) Das, R.; Kiley, P. J.; Segal, M.; Norville, J.; Yu, a. A.; Wang, L.; Trammell, S. a.; Reddick, L. E.; Kumar, R.; Stellacci, F.; et al. Integration of Photosynthetic Protein Molecular Complexes in Solid-State Electronic Devices. *Nano Lett.* **2004**, *4*, 1079–1083.

(14) Ciesielski, P. N.; Cliffel, D. E.; Jennings, G. K. Kinetic Model of the Photocatalytic Effect of a Photosystem I Monolayer on a Planar Electrode Surface. *J. Phys. Chem. A* **2011**, *115*, 3326–3334.

(15) Gross, E. L.; Youngman, D. R.; Winemiller, S. L. An FMN-Photosystem I Photovoltaic Cell. *Photochem. Photobiol.* **1978**, *28*, 249–256.

(16) Ciesielski, P. N.; Faulkner, C. J.; Irwin, M. T.; Gregory, J. M.; Tolk, N. H.; Cliffel, D. E.; Jennings, G. K. Enhanced Photocurrent Production by Photosystem I Multilayer Assemblies. *Adv. Funct. Mater.* **2010**, *20*, 4048–4054.

(17) Chen, G.; LeBlanc, G.; Jennings, G. K.; Cliffel, D. E. Effect of Redox Mediator on the Photo-Induced Current of a Photosystem I Modified Electrode. *J. Electrochem. Soc.* **2013**, *160*, H315–H320.

(18) Darby, E.; Leblanc, G.; Gizzie, E. A.; Winter, K. M.; Jennings, G. K.; Cliffel, D. E. Photoactive Films of Photosystem I on Transparent Reduced Graphene Oxide Electrodes. *Langmuir* **2014**, *30*, 8990–8994.

(19) Kothe, T.; Pöller, S.; Zhao, F.; Fortgang, P.; Rögner, M.; Schuhmann, W.; Plumeré, N. Engineered Electron-Transfer Chain in Photosystem 1 Based Photocathodes Outperforms Electron-Transfer Rates in Natural Photosynthesis. *Chem. - A Eur. J.* **2014**, *20*, 11029–11034.

(20) Badura, A.; Guschin, D.; Kothe, T.; Kopczak, M. J.; Schuhmann, W.; Rögner, M.

Photocurrent Generation by Photosystem 1 Integrated in Crosslinked Redox Hydrogels. *Energy Environ. Sci.* **2011**, *4*, 2435.

(21) Stieger, K. R.; Feifel, S. C.; Lokstein, H.; Lisdat, F. Advanced Unidirectional Photocurrent Generation via Cytochrome c as Reaction Partner for Directed Assembly of Photosystem I. *PCCP* **2014**, *16*, 15667–15674.

(22) Stieger, K. R.; Ciornii, D.; Kölsch, A.; Hejazi, M.; Lokstein, H.; Feifel, S. C.; Zouni, A.; Lisdat, F. Engineering of Supramolecular Photoactive Protein Architectures: The Defined Co-Assembly of Photosystem I and Cytochrome c Using a Nanoscaled DNA-Matrix. *Nanoscale* **2016**, *8*, 10695–10705.

(23) Robinson, M. T.; Simons, C. E.; Cliffel, D. E.; Jennings, G. K. Photocatalytic Photosystem I/PEDOT Composite Films Prepared by Vapor-Phase Polymerization. *Nanoscale* **2017**, *9*, 6158–6166.

(24) Yang, S.; Robinson, M. T.; Mwambutsa, F.; Cliffel, D. E.; Jennings, G. K. Effect of Cross-Linking on the Performance and Stability of Photocatalytic Photosystem I Films. *Electrochim. Acta* **2016**, *222*, 926–932.

(25) Lee, J. W.; Lee, I.; Philip, D.; Owens, T. G.; Greenbaum, E. Chemical Platinization and Its Effect on Excitation Transfer Dynamics and P700 Photooxidation Kinetics in Isolated Photosystem I. *Biophys. J.* **1995**, *69*, 652–659.

(26) Bard, A. J.; Faulkner, L. R.; Swain, E.; Robey, C. *Electrochemical Methods*, Second.; John Wiley & Sons, Inc., 2001.

(27) Liu, J.; Zhang, X.; Wang, M.; Liu, J.; Cao, M.; Lu, J.; Cui, Z. Characterization of Photosystem I from Spinach: Effect of Solution pH. *Photosynth. Res.* **2012**, *112*, 63–70.

(28) Chitnis, P. R. Photosystem I: Function and Physiology. *Annu. Rev. Plant Physiol. Plant Mol. Biol.* **2001**, *52*, 593–626.

(29) LeBlanc, G.; Chen, G.; Gizzie, E. A.; Jennings, G. K.; Cliffel, D. E. Enhanced Photocurrents of Photosystem I Films on P-Doped Silicon. *Adv. Mater.* **2012**, *24*, 5959–5962.

(30) Kincaid, H. A.; Niedringhaus, T.; Ciobanu, M.; Cliffel, D. E.; Jennings, G. K. Entrapment of Photosystem I within Self-Assembled Films. *Langmuir* **2006**, *22*, 8114–8120.

(31) Shiozawa, J. A.; Alberte, R. S.; Thornber, J. P. The P700-Chlorophyll a-Protein. *Arch. Biochem. Biophys.* **1974**, *165*, 388–397.

(32) Baba, K.; Itoh, S.; Hastings, G.; Hoshina, S. Photoinhibition of Photosystem I Electron Transfer Activity in Isolated Photosystem I Preparations with Different Chlorophyll Contents. *Photosynth. Res.* **1996**, *47*, 121–130.

CHAPTER 4

PHOTOSYSTEM I MULTILAYER FILMS FOR PHOTOVOLTAGE ENHANCEMENT IN NATURAL DYE-SENSITIZED SOLAR CELLS

Introduction

Evolution has provided the myriad chemistries and robust energy transformations that are the enduring basis for life. Likewise, concepts inspired by these natural archetypes mold human societies healthier, more connected, and crucially, more powered. Consequently, as climate change hastens global efforts to efficiently harvest solar energy, we turn to nature for answers.

The dye-sensitized solar cell (DSSC) imitates the function of photosystems—protein photodiodes contained within all green photosynthetic organisms.[1] DSSCs achieve power conversion efficiencies of up to 12%[2] whilst maintaining favorable purity and energy-of-assembly requirements relative to conventional silicon p-n junctions. Efficiency improvements parallel development of sophisticated and often expensive metal coordination complexes.[2,3] However, a library of natural compounds—the anthocyanins (ACs)—fills the role of molecular dye in a DSSC for a fraction of the cost.[4]

Byproducts of plants, ACs promote the most vibrant hues in nature[5] and also exhibit serendipitous chemical affinity for the metal-oxides of DSSC photoanodes.[6] While DSSCs utilizing these natural dyes (n-DSSCs) are not as efficient as their synthetic analogues, their enticements—simple fabrication, lower cost, and benign chemistry—remain.[7]

Electrolytic recombination—by which excited states in the adsorbed dye are oxidized by solubilized redox mediators—is a major contributor to the lower efficiency of n-DSSCs (≤ 2%) relative to DSSCs incorporating synthetic dyes. The electrolytic recombination reaction proceeds as:[6]

$$O + D^* \xrightarrow{k_{rec}} R + D^+ \quad (1)$$

where D^* and D^+ are the excited and electron-depleted states of an adsorbed dye molecule and k_{rec} is the rate constant for electrolytic recombination. R and O denote the reduced and oxidized states of a solubilized redox molecule, respectively. Electrolytic recombination reduces the number of electrons available for injection into the dye-sensitized semiconductor *via*

$$D^* \xrightarrow{k_{inj}} D^+ + e \quad (2)$$

where k_{inj} is the rate constant for electron injection.[8] Electron-depleted dye molecules are replenished through reaction with reduced mediator species,

$$R + D^+ \xrightarrow{k_{red}} O + D^* \quad (3)$$

where k_{red} is the rate constant associated with dye reduction. Given the generally high k_{rec} of AC sensitizers,[6] fewer electrons accumulate in the coupled semiconductor conduction band to contribute to observed photovoltage. Accordingly, methods that curb electrolytic recombination reactions—by decreasing the concentration of O within the dye-sensitized photoanode—or augment dye reduction reactions—by increasing the concentration of R within the photoanode—will increase the photovoltage of n-DSSCs. Here, we couple the

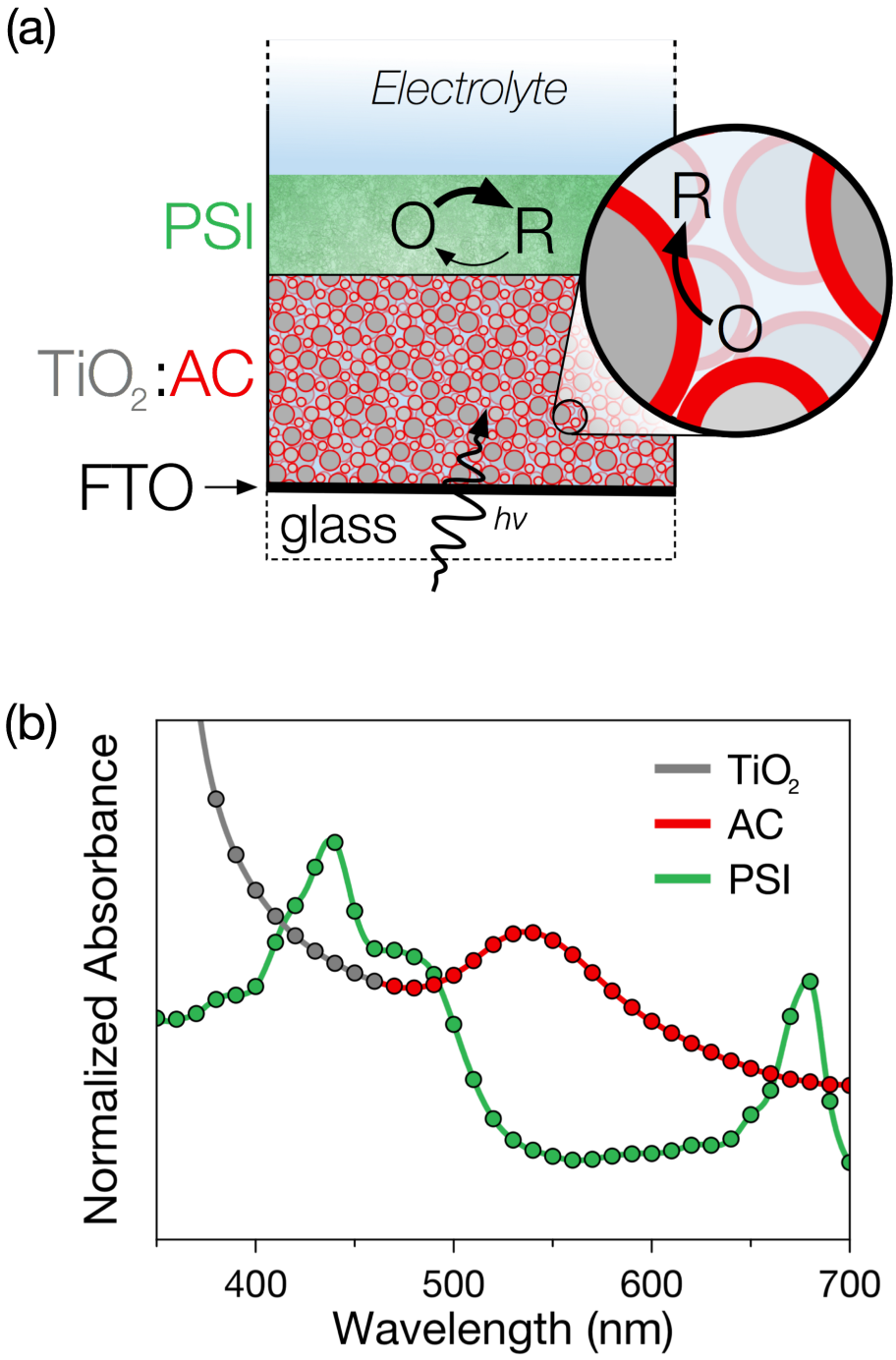

Figure 4.1. Cell Schematic and Coupled Absorbance Profile. (a) A PSI multilayer film is assembled atop a mesoporous film of TiO_2 nanoparticles sensitized by natural anthocyanin molecules to construct a hierarchical n-DSSC photoanode. Rapid vacuum-assisted assembly minimizes PSI penetration into the mesoporous substrate and so, integrity of the underlying photoanode is maintained. (b) The incorporation of PSI within an n-DSSC improves overall light utilization, as PSI and AC have complementary absorbances.

photo-induced kinetics of a film of Photosystem I (PSI) proteins to an n-DSSC photoanode (**Figure 5.1a**) to address these aims and boost cell photovoltage. Furthermore, the purple, blue, and red absorbance of PSI complements the green absorbance of ACs and thus, this coupled cell architecture expands utilization of the solar spectrum (**Figure 5.1b**).

Results and Discussion

In organisms, PSI coordinates electron excitation and isolation to provide a 1.1 V reduction potential with nearly perfect internal quantum efficiency.[9] Ex vivo, isolated PSI is employed within biohybrid solar cells that merge the protein's photo-induced chemistry with an electrochemical circuit. In the case of PSI multilayer films, electro-active mediators—polymers, proteins, or ions—provide connection between electronic states of PSI distributed throughout the film and those of an underlying electrode.[10] In this way, a PSI multilayer film immersed in an aqueous electrolyte containing the diffusible mediators $Fe(CN)_6^{4-}$ and $Fe(CN)_6^{3-}$—which we will refer to as R and O, respectively—stimulates a potential difference at an electrode surface as described by the Nernst Equation:[11]

$$V_{PSI} = 25.7\ mV \times ln\left(\frac{C_{R,B}}{C_{O,B}}\frac{C_O(0,t)}{C_R(0,t)}\right) \quad (4)$$

where $C_{R,B}$ and $C_{O,B}$ are the initial bulk concentrations of reduced and oxidized mediator, respectively, and $C_R(0,t)$ and $C_O(0,t)$ are the altered concentrations of reduced and oxidized mediator at the electrode surface at time, t, respectively. Incorporation of concentration conservation statements—$C_T = C_{O,B} + C_{R,B} = C_O(0,t) + C_R(0,t)$—and a definition of change in reduced mediator concentration—$\Delta C_R(0,t) = C_R(0,t) - C_{R,B}$—

permits eqn. 4 to be rearranged for an estimate of concentration modification at an electrode surface:

$$\frac{\Delta C_R(0,t)}{C_T} = \left(\frac{C_{R,B}C_{O,B}}{C_{R,B}+C_{O,B}}\right)\left(\frac{1-exp[0.039V_{PSI}]}{C_{R,B}+C_{O,B}exp[0.039V_{PSI}]}\right) \quad (1)$$

where $\Delta C_R(0,t)/C_T$ is the time-dependent change in reduced mediator at the electrode surface generated by a PSI multilayer under illumination as a fraction of C_T, the total concentration of mediators. Note that V_{PSI} is in mV and $\Delta C_R(0,t) = -\Delta C_O(0,t)$.

With $C_{O,B}$ held constant at 0.1 mM, photopotential attenuates from -25 mV to -1 mV with increase in $C_{R,B}$ from 0.01 mM to 100 mM (**Figure 4.2b**, black curve). The associated modification in mediator concentration, calculated via eqn. 5, is revealed to be positive across all $C_{R,B}$ tested; this implies that mediator reduction events generally outpace mediator oxidation events in the illuminated PSI film, leading to increase and decrease in C_R and C_O, respectively, in the surrounding regions of the electrochemical cell. Therefore, by employing the electrolyte as a conduit, a PSI multilayer film coupled to an n-DSSC will simultaneously decrease C_O and increase C_R within a proximal photoanode to ease electrolytic recombination (eqn. 1) and raise dye reduction (eqn. 3) reactions, respectively, to increase the number of electrons injected into the semiconductor conduction band (eqn. 2) and ultimately magnify overall cell photovoltage (**Figure 4.3**).

To this end, we employ vacuum-assisted drop casting[10] to assemble a PSI multilayer film atop an n-DSSC photoanode, composed of a TiO_2 film coated with ACs derived from the extract of blackberries—containing approximately 90% w/w cyanidin-3-glucoside and 10% w/w cyanidin-3-glucosylmalonate (**Figure 4.3**).[12] PSI's large hydrodynamic diameter ($d_h \geq 40$ nm)[13] prevents it from incorporating from solution to

within mesoporous substrates ($d_{pore} \leq 50$ nm)—including gold[14] and TiO_2[15]—on timescales of less than 24 h. Thus, the short evaporation time associated with vacuum-assisted drop casting—less than 30 min—permits deposition of a multilayer film of PSI proteins atop an AC-sensitized TiO_2 anode (TiO_2:AC) with minimal protein penetration into the underlying structure. As a result, PSI in this cell architecture does not obstruct the surfaces of TiO_2:AC.

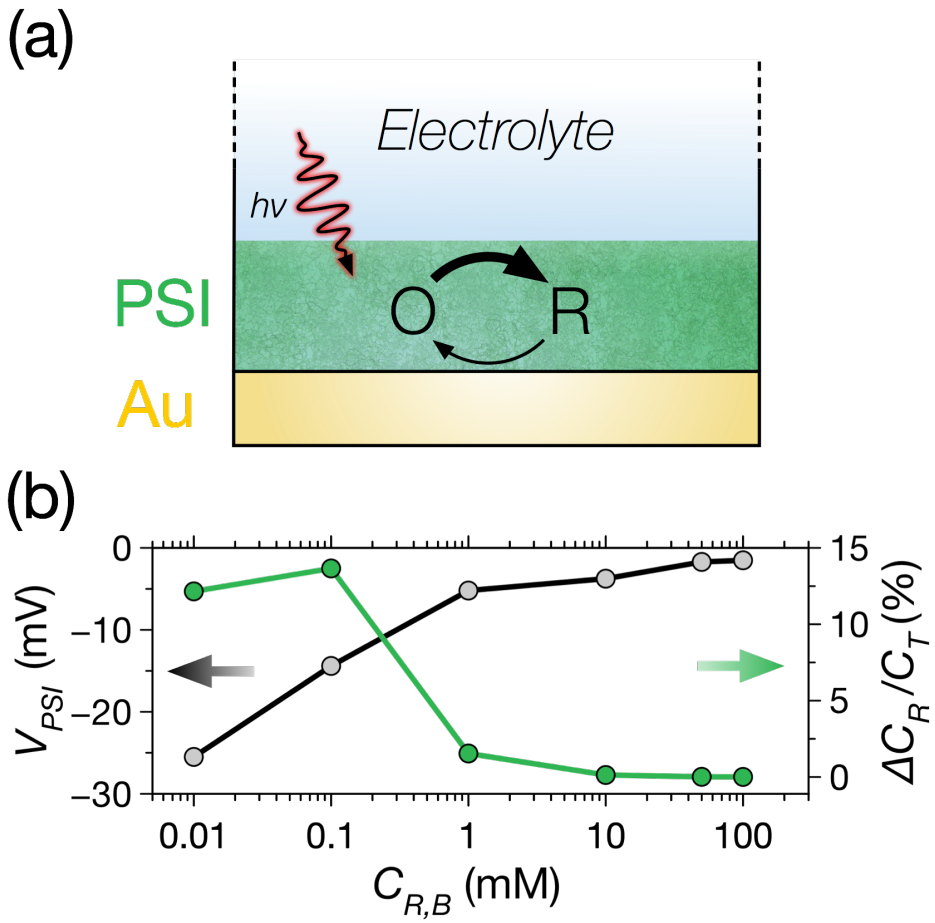

Figure 4.2. Photovoltage Contributed by PSI Multilayer Films on Gold Electrodes. (a) A PSI multilayer film deposited atop a gold electrode and immersed in an electrolyte with solubilized $Fe(CN)_6^{4-/3-}$ promotes a photo-response based on the rapid reduction kinetics of PSI under illumination. (b) Electrochemical potentiometry is used to monitor photovoltage generated by a film of PSI proteins with varying $C_{R,B}$ ($C_{O,B} = 0.1$ mM), and the extent of concentration polarization is calculated via the Nernst Equation. We find that PSI films perturb mediator concentrations most effectively with $C_{R,B} \leq 0.1$ mM.

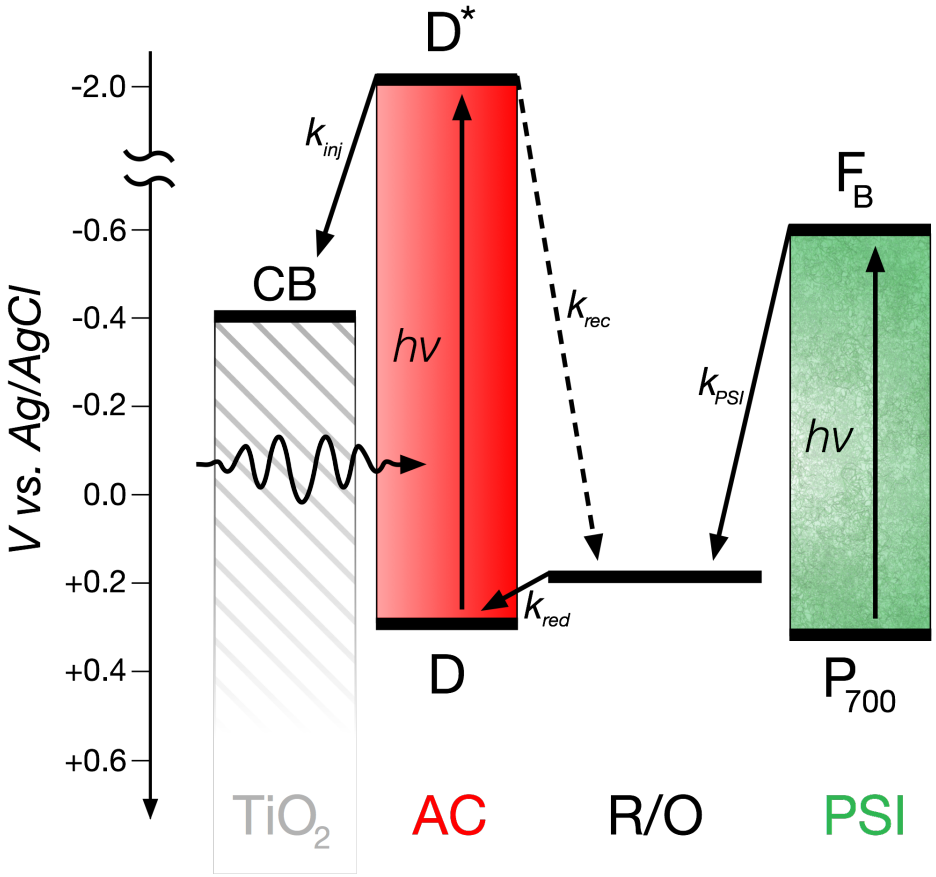

Figure 4.3. Energy Diagram of an n-DSSC Photoanode with Addition of a Discrete PSI Multilayer Film. The photo-induced kinetic activity of a PSI multilayer film increases and decreases the concentration of R and O, respectively, to promote an increased rate of dye reduction and decreased rate of electrolytic recombination within distant regions of the AC-sensitized photoanode. This leads to augmented electron injection into TiO_2 and improved photovoltage.

Our strategy to employ PSI proteins within a DSSC framework is an adaptive departure from past efforts to adsorb the large protein within mesoporous TiO_2 to fashion a PSI-sensitized solar cell (PSI-SSC). The supramolecular PSI occupies more than an order of magnitude more surface area relative to the molecular ACs when adsorbed to a surface—approximately 30 nm^2 [16] vs. 1 nm^2, respectively—and so, PSI-SSCs are intrinsically restricted in the maximum number of sites available for electron injection into TiO_2 during device operation. This size factor—coupled to orientation heterogeneity of adsorbed PSI—is largely responsible for the 6-fold contrast in presently achievable efficiencies between optimized PSI-SSCs and AC-based n-DSSCs (0.3%[15] vs. 1.9%[17]). Therefore, by removing PSI from within the anode and positioning it in an exterior role as a dense multilayer, we permit both natural species to perform practical, synergistic functions within the overall cell.

To test the proposed mechanism, three-electrode potentiometry was used to measure the time-resolved photovoltage of TiO_2, TiO_2/PSI, TiO_2:AC, and TiO_2:AC/PSI photoanodes (**Figure 4.4a**). Tests were conducted in an aqueous electrolyte with $C_{R,B}$ and $C_{O,B}$ set to 0.1 mM and 0.1 mM, respectively, which corresponds to the maximum measured $\Delta C_R(0,t)/C_T$ of PSI films on gold electrodes (**Figure 4.2b**). Cells were illuminated using a white light source with minimum and maximum wavelengths of 380 nm and 790 nm, respectively. Predictably, in absence of appreciable absorption within the spectral window of illumination and electron injection from an adsorbed sensitizer, TiO_2 generates modest photovoltage of -5 mV. The addition of a PSI multilayer to the surface of the TiO_2 permits an improved photovoltage of -15 mV, consistent with PSI's provision of Nernst-type photopotential (eqn. 4). However, sensitization of TiO_2 with AC

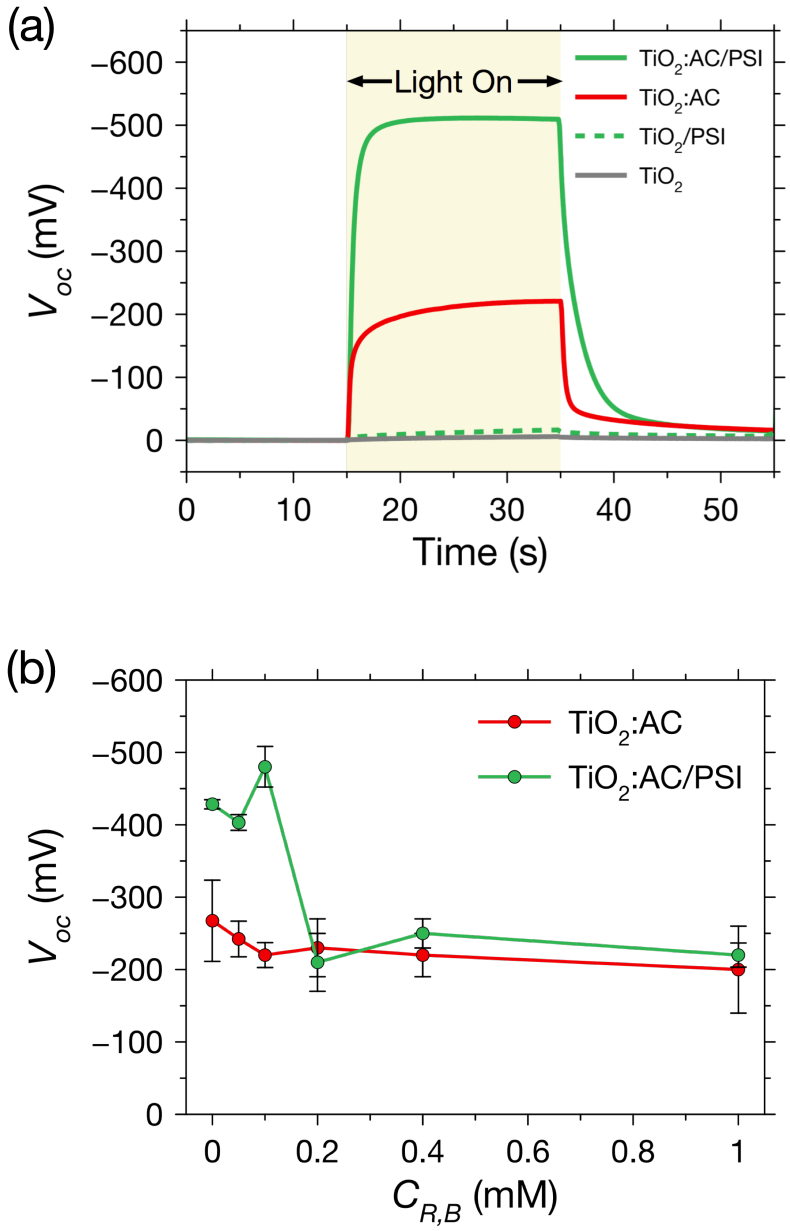

Figure 4.4. Photovoltage of Unmodified and PSI Multilayer-Contacted n-DSSC Photoanodes. (a) Even when coupled to a PSI multilayer film, TiO_2 photoanodes not sensitized by AC provide modest photopotential. However, when assembled above a n-DSSC photoanode, a PSI multilayer promotes a more than two-fold increase in steady-state photovoltage relative to a non-contacted TiO_2:AC film. The rapid photoreduction of O within the PSI film translates to reduced C_O within the underlying TiO_2:AC, resulting in attenuated recombination and augmented photopotential. Tests were all conducted with an aqueous electrolyte containing 0.1 mM R, 0.1 mM O, 100 mM KCl, and 5 mM tris (pH 8.0). (b) Steady-state photovoltage is assessed for n-DSSCs comprised of TiO_2:AC and TiO_2:AC/PSI under variable electrolyte composition. Mirroring the enhancements of PSI on gold electrodes, PSI multilayer films were observed to perform best with $C_{R,B} \leq$ 0.1 mM.

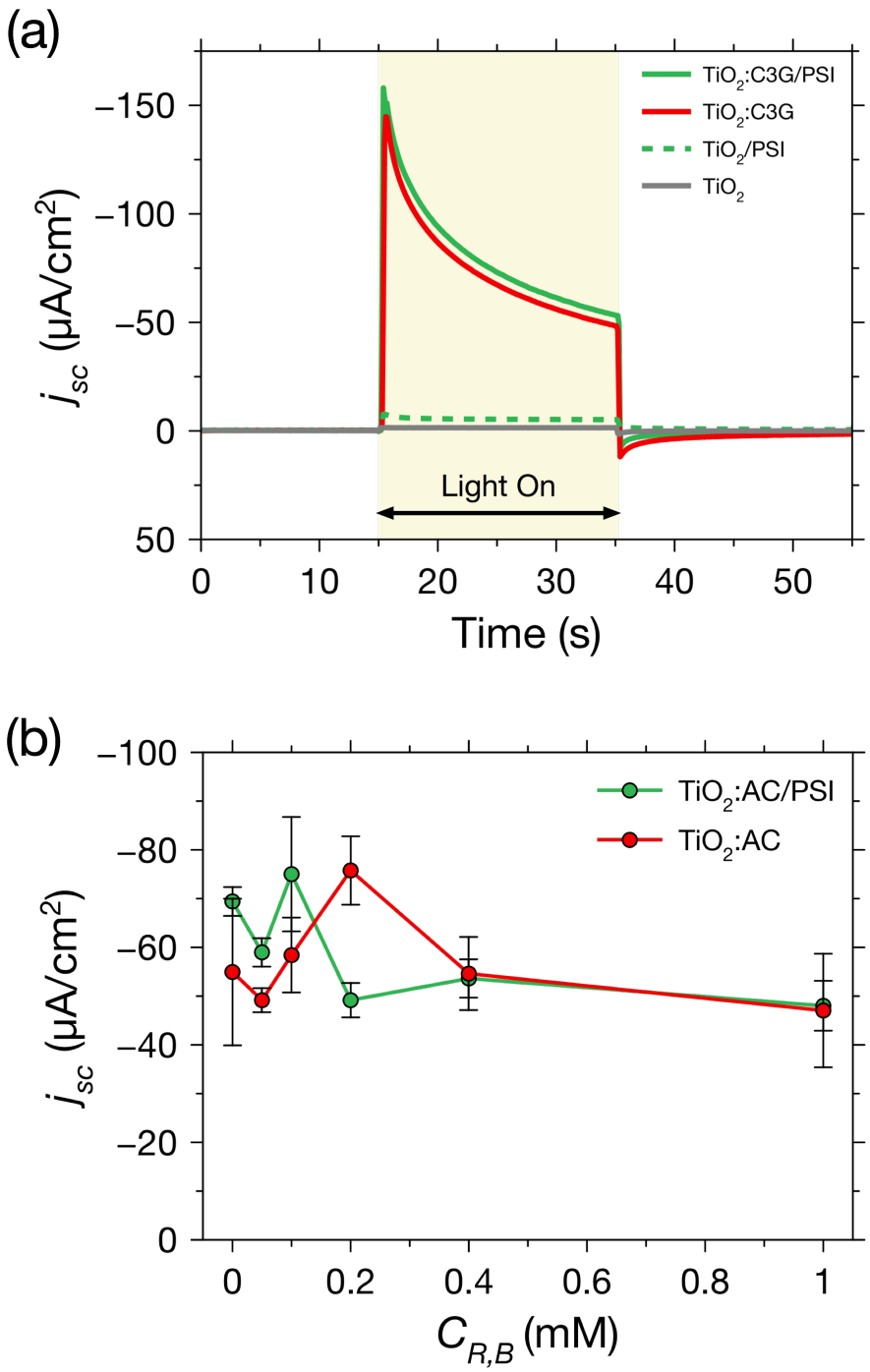

Figure 4.5. Photocurrent of Unmodified and PSI Multilayer-Contacted n-DSSC Photoanodes. (a) TiO_2 photoanodes with adsorbed AC molecules (TiO_2:AC) promote significantly improved photocurrent relative to unmodified TiO_2 and TiO_2/PSI. However, photocurrent of an AC-sensitized TiO_2 anode is largely unchanged by addition of a drop cast PSI multilayer film. Photochronoamperometry was conducted using an electrolyte containing 0.1 mM R, 0.1 mM O, 100 mM KCl, 5 mM tris (pH 8). (b) Photocurrent is not significantly affected by augmented $C_{R,B}$. Even so, peak photocurrent for PSI multilayer-coated photoanodes occurs for $C_{R,B} \leq$ 0.1 mM and at $C_{R,B}$ = 0.2 mM for the uncoated control. $C_{O,B}$ was 0.1 mM for all photocurrent tests.

to form TiO_2:AC permits ample photoelectron generation and injection into the TiO_2 resulting in an enhanced photovoltage of -220 mV. Finally, TiO_2:AC/PSI photoanodes provide -500 mV of sustained photopotential, representing a more than two-fold improvement over uncoated TiO_2:AC.

Furthermore, we measured the photopotential of TiO_2:AC and TiO_2:AC/PSI under variable $C_{R,B}$ with $C_{O,B}$ held constant at 0.1 mM (**Figure 4.4b**). TiO_2:AC anodes provided approximately constant photovoltage for all values of $C_{R,B}$ tested. For $C_{R,B} \leq 0.1$ mM—within the range that PSI contributes strong concentration polarization (**Figure 4.2b**)—TiO2:AC/PSI anodes provide 400-500 mV of photovoltage. For $C_{R,B} > 0.1$ mM—outside the range of optimal concentration polarization—photovoltages between non-coated and PSI-coated anodes were statistically equivalent (~-200 mV).

Finally, photocurrent was measured for TiO_2, TiO_2/PSI, TiO_2:AC, and TiO_2:AC/PSI photoanodes for $C_{R,B} = 0.1$ mM and $C_{O,B} = 0.1$ mM (**Figure 4.5a**). As for photovoltage measurements, photocurrent for TiO_2 and TiO_2/PSI photoanodes was meager—1 $\mu A/cm^2$ and 5 $\mu A/cm^2$, respectively. Furthermore, TiO_2:AC photoanodes promote significantly improved photocurrents (50 $\mu A/cm^2$). In contrast to photovoltage, TiO_2:AC/PSI does not provide statistically significant improvements in photocurrent relative to TiO_2:AC, even across a spectrum of $C_{R,B}$ (**Figure 4.5b**).

Conclusions

We employed a stacked photoanode configuration—consisting of a PSI multilayer atop natural dye-sensitized TiO_2—for substantial photovoltage enhancement over uncoated substrates. We assert that PSI photoelectrochemically biases the redox state of

$[Fe(CN)_6]^{4-/3-}$ throughout the dye-sensitized, mesoporous anode, forcing higher observed potential by changing the dye-electrolyte recombination kinetics. Our method provides improvements without adding complication to construction of the underlying anode, as is the case for co-sensitization approaches. Due to complementary light absorbances, the combination of PSI and AC improves utilization of the visible spectrum. Our work advances the pursuit of effective utilization of PSI as a cost-effective additive within existing photovoltaic systems.

Experimental Methods

Photosystem I Extraction

PSI was extracted from baby spinach leaves as described previously,[18] and the resulting solutions were dialyzed to remove salts and surfactants prior to film assembly.[10] Thylakoid membranes were isolated by consecutive maceration and centrifugation at 8 000 g. The resulting supernatant was removed and the pellet resuspended in Triton X-100 to lyse the thylakoid membranes. This solution was centrifuged at 20 000 g and the supernatant was purified by hydroxylapatite column chromatography and stored at -80 ^{o}C. Dialysis was performed using 10000 MWCO dialysis tubing (Spectrapore) for 12 h. Using the methods of Baba et. al.,[19] P_{700} concentration was determined to be 3.3 μM with a chl/P_{700} ratio of 42.

Preparation of TiO_2 Films

Fluorine doped tin-oxide substrates (TEC15, MTI corporation) were rinsed vigorously in water and ethanol and subsequently dried in a stream of nitrogen gas. The

films were then treated with ozone plasma for 15 min to obtain a hydrophilic surface for spin coating. A 3:1 ethanol/TiO_2 paste (dyesol NRT18) mixture was subsequently spin coated atop the substrates (3500 RPM, 1 min). The films were sintered at 500 ^oC for 30 min in a muffle furnace to convert the TiO_2 to its anatase crystalline phase and cooled overnight. The average thickness of TiO_2 films was determined to be ~700 nm using a stylus profilometer (Dektak).

TiO_2 Sensitization

20 g of raw blackberries (Dole® brand) were pulverized with mortar and pestle. 20 mL of ethanol was added, and the resulting mixture was stirred, filtered and finally poured over the TiO_2 films. The container was sealed to prevent ethanol evaporation and left in the dark for 24 h to allow adsorption of AC to the mesoporous TiO_2. The resulting films were rinsed carefully in ethanol and dried using a stream of nitrogen.

PSI Multilayer Deposition on Dye-Sensitized Anodes

PSI was drop cast directly atop sensitized TiO_2 films following previously described procedures by this lab.[10] Briefly, 50 μL of a dialyzed PSI solution was pipetted atop AC-sensitized TiO_2. Vacuum was subsequently applied to evaporate water, leaving a dry PSI multilayer film behind in ~30 min. Films were circular with a surface area of approximately 1 cm^2 and thickness of ~300 nm as measured by profilometry (Dektak).

Electrochemical Measurements

All electrochemical characterization was performed using a CH instruments

CH660a workstation equipped with a Faraday cage. All measurements employed an FTO/TiO_2 working electrode, a platinum mesh counter electrode and Ag/AgCl aqueous reference electrode. Solutions consisted of 100 mM KCl supporting electrolyte and 5 mM tris buffer adjusted to pH 8 via dropwise addition of 1M HCl. Charge transfer was mediated by a $K_4Fe(CN)_6/K_3Fe(CN)_6$ redox shuttle at variable concentrations.

Photochronoamperometric measurements were performed at the cell's steady state open circuit potential (approximately +200mV vs. Ag/AgCl), which was established after 200 s. The photopotentials of cells were subsequently characterized by time-resolved open circuit potential measurements. Photocurrent/potential values used for statistical comparison were obtained through subtraction of the dark value from that after 20 s of illumination. The light source used in all measurements was a 250 W cold light source (Leica KL 2500 LCD), which emitted a light intensity of 140 mW/cm^2 and spectral range of 380-790 nm. Photocurrent measurements were normalized to the illuminated area of the electrode (0.28 cm^2), constrained using a hole-punched mask applied to the nonconducting glass surface of the FTO/TiO_2:AC electrode. As is convention, illumination for all studies was directed incident on the FTO such that the TiO_2 surface received maximal photon flux.

Works Cited

(1) Grätzel, M. Photoelectrochemical Cells. *Nature* **2001**, *414*, 338–344.

(2) Hishikawa, Y.; Warta, W.; Green, M. A.; Levi, D. H.; Hohl, J.; Anita, E.; Baillie, W. Y. H.; Dunlop, E. D. Solar Cell Efficiency Tables. *Prog Photovolt Res Appl* **2017**, *25*, 668–676.

(3) Nazeeruddin, M. K.; Kay, A.; Rodicio, I.; Humphry-Baker, R.; Müller, E.; Liska, P.; Vlachopoulos, N.; Grätzel, M. Conversion of Light to Electricity by Cis-X_2Bis(2,2'-bipyridyl-r,r'-dicarboxylate)ruthenium(II) Charge-Transfer Sensitizers (X= Cl-, Br-, I-, CN-, and SCN-) on Nanocrystalline TiO_2 Electrodes. *J. Am. Chem. Soc.* **1993**, *115*, 6382–6390.

(4) Calogero, G.; Yum, J.; Sinopoli, A.; Di Marco, G.; Grätzel, M. Anthocyanins and Betalains as Light-Harvesting Pigments for Dye-Sensitized Solar Cells. *Sol. Energy* **2012**, *86*, 1563–1575.

(5) Markarkis, P. *Anthocyanins as Food Colors*; Academic Press Incorporated, 1982.

(6) Cherepy, N. J.; Smestad, G. P.; Grätzel, M.; Zhang, J. Z. Ultrafast Electron Injection : Implications for a Photoelectrochemical Cell Utilizing an Anthocyanin Dye-Sensitized TiO2 Nanocrystalline Electrode. *J. Phys. Chem. B* **1997**, *5647*, 9342–9351.

(7) Narayan, M. R. Review: Dye Sensitized Solar Cells Based on Natural Photosensitizers. *Renew. Sustain. Energy Rev.* **2011**, *16*, 208–215.

(8) Gómez, R.; Salvador, P. Photovoltage Dependence on Film Thickness and Type of Illumination in Nanoporous Thin Film Electrodes according to a Simple Diffusion Model. *Sol. Energy Mater. Sol. Cells* **2005**, *88*, 377–388.

(9) Nelson, N.; Yocum, C. F. Structure and Function of Photosystems I and II. *Annu. Rev. Plant Biol.* **2006**, *57*, 521–565.

(10) Ciesielski, P. N.; Faulkner, C. J.; Irwin, M. T.; Gregory, J. M.; Tolk, N. H.; Cliffel, D. E.; Jennings, G. K. Enhanced Photocurrent Production by Photosystem I Multilayer Assemblies. *Adv. Funct. Mater.* **2010**, *20*, 4048–4054.

(11) Bard, A. J.; Faulkner, L. R.; Swain, E.; Robey, C. *Electrochemical Methods*, Second.; John Wiley & Sons, Inc., 2001.

(12) Bowen-Forbes, C. S.; Zhang, Y.; Nair, Muraleedharan, G. Anthocyanin Content, Antioxidant, Anti-Inflammatory and Anticancer Properties of Blackberry and Raspberry Fruits. *J. Food Compos. Anal.* **2010**, *23*, 554–560.

(13) Liu, J.; Zhang, X.; Wang, M.; Liu, J.; Cao, M.; Lu, J.; Cui, Z. Characterization of Photosystem I from Spinach: Effect of Solution pH. *Photosynth. Res.* **2012**, *112*, 63–70.

(14) Ciesielski, P. N.; Scott, A. M.; Faulkner, C. J.; Berron, B. J.; Cliffel, D. E.; Jennings, G. K. Functionalized Nanoporous Gold Leaf Electrode Films for the Immobilization of Photosystem I. *ACS Nano* **2008**, *2*, 2465–2472.

(15) Yu, D.; Wang, M.; Zhu, G.; Ge, B.; Liu, S.; Huang, F. Enhanced Photocurrent Production by Bio-Dyes of Photosynthetic Macromolecules on Design TiO_2 Film. *Sci. Rep.* **2015**, *5*, 1–9.

(16) Lee, J. W.; Lee, I.; Philip, D.; Owens, T. G.; Greenbaum, E. Chemical Platinization and Its Effect on Excitation Transfer Dynamics and P700 Photooxidation Kinetics in Isolated Photosystem I. *Biophys. J.* **1995**, *69*, 652–659.

(17) Singh, L. K.; Karlo, T.; Pandey, A. Begonia Dye as an Efficient Anthocyanin Sensitizer. *J. Renew. Sustain. Energy* **2013**, *5*, 1–11.

(18) Reeves, S. G.; Hall, D. O. Higher Plant Chloroplasts and Grana: General Preparative Procedures (Excluding High Carbon Dioxide Fixation Ability Chloroplasts). *Methods Enzymol.* **1980**, *69*, 85–94.

(19) Baba, K.; Itoh, S.; Hastings, G.; Hoshina, S. Photoinhibition of Photosystem I

Electron Transfer Activity in Isolated Photosystem I Preparations with Different Chlorophyll Contents. *Photosynth. Res.* **1996**, *47*, 121–130.

CHAPTER 5

PHOTOCATALYTIC PHOTOSYSTEM I/PEDOT COMPOSITE FILMS PREPARED BY VAPOR-PHASE POLYMERIZATION

Introduction

Photosystem I (PSI) is a photosynthetic protein that efficiently converts visible light into sustained reduction potential. *In vivo*, PSI facilitates electron excitation and cross-membrane transport necessary for carbon fixation in living cells.[1,2] Briefly, chlorophylls absorb photons and transfer harvested energy to an embedded chlorophyll A dimer, P_{700}. Receipt of sufficient energy prompts an energetic transition (P_{700}^{*}) and subsequent electron transfer along an internal electron transport chain to a redox-active iron–sulfur complex, F_B.

Due to its natural abundance and near-unity internal quantum efficiency, isolated PSI has been used as a photodiode to augment heterogeneous photoelectrochemistry, including photocatalytic hydrogen evolution[3,4] and light harvesting in dye-sensitized solar cells.[5–7] Through application of specialized surface chemistries[8,9] and genetic modification,[10] monolayers of PSI proteins have been coupled to conductive substrates to promote direct charge exchange.[11] Furthermore, our group has employed multilayers of spinach-derived PSI toward significant improvements in photocurrents over monolayer-based systems on planar gold,[12–14] silicon,[15,16] and graphene[17] electrodes. Multilayer enhancements in photocurrent persist for many months[13]—well in excess of plant growing seasons—and increase with the amount of protein deposited.[12]

More recently, PSI has been introduced within ion- or electron-conductive matrices toward more effective charge mediation in multilayer assemblies. Badura *et al.* incorporated PSI proteins within an osmium-based redox hydrogel to achieve PSI turnover rates nearly seven times that of natural photosynthesis.[18,19] Stieger *et al.* assembled films containing PSI and cytochrome c atop electrode surfaces to produce efficient and stable photocurrents enabled via charge mediation by cytochrome c.[20,21]

Recently, we entrapped PSI within electrochemically-grown polyaniline (PAni) and observed enhanced photocurrents due to amplified electron transfer throughout a well-integrated PAni scaffold.[22] Solid-state PAni:PSI devices produce the highest power conversion efficiency (PCE) reported thus far in the solid state PSI literature and are remarkably resilient under prolonged on/off cycling owing to the environmental stability of PAni and entrapped PSI.[23]

We now seek to consolidate PSI within other intrinsically conductive polymer (ICP) scaffolds to investigate the effects of polymer attributes—including HOMO/LUMO energetics and side-chain chemistries—on the performance of solid-state PSI:ICP assemblies. However, electrochemical polymerization procedures are not sufficiently adaptable to achieve these aims in isolation. First, aqueous electrochemical polymerization—preferred given PSI's biological origin—is incompatible with many potentially interesting ICPs due to monomer insolubility. Second, PSI uptake within electrochemically-prepared composite films is meager, a function of generally ineffective attractive interactions between PSI and migrating monomer species during assembly; for our PAni:PSI films this upper limit was less than 1.5% PSI by film volume despite prevalent aniline/PSI hydrogen bonding. Therefore, we seek to develop a complementary

technique for PSI:ICP preparation that is: (1) adaptable to an extensive catalog of ICPs and surfaces and (2) permits PSI film loading to approach that of our previously reported multilayer assemblies.

Vapor-phase polymerization (VPP) provides a route to polymer growth that is simple, rapid, and tunable. VPP achieves growth of numerous ICPs—including PAni,[24] polypyrrole (PPy),[25,26] poly(3,4-ethylenedioxythiophene) (PEDOT),[27,28] and numerous polythiophenes[29,30]—without the use of a reaction solvent. A thin layer of Friedel Crafts catalyst—$CuCl_2$, $FeCl_3$, or $MoCl_5$—is deposited on a surface of choice, and subsequent exposure to monomer vapor stimulates >100 nm of film growth in minutes. In particular, vapor-polymerized PEDOT (vpPEDOT) is highly stable under ambient conditions and benefits from more than a decade of academic and industrial study.[31,32] vpPEDOT is also remarkably biocompatible.[33–35] Bongo *et al.* incorporated gelatin into vpPEDOT and used these assemblies as electrically-responsive substrates for endothelial cell attachment and growth; PEDOT and gelatin were observed to retain their conductive and connective functionalities, respectively.[36] Furthermore, vpPEDOT can be grafted to aromatic substrates in a straightforward manner. Im *et al.* demonstrated covalent grafting of vpPEDOT to aromatic surfaces—including polystyrene, polyethylene terephthalate, and polyurethane[37]—via a radical cation coupling mechanism first identified by Kovacic *et al.*[38] Accordingly, vpPEDOT films grafted to polystyrene substrates resist delamination when subjected to intense ultrasonication.

Herein, we report incorporation of PSI proteins within an ICP scaffold through consolidation of VPP and vacuum-assisted PSI multilayer assembly. PSI solutions containing $FeCl_3$ are drop cast atop a substrate of choice, and subsequent exposure to

monomer vapor prompts rapid growth of a chosen ICP. We observe robust growth of vpPEDOT (**Figure 5.1**) and vpPPy (**Figure 5.2**) from catalyst-replete PSI multilayers on glass, fluorine-doped tin oxide (FTO), and gold substrates upon exposure to ICP monomer vapor. Furthermore, we hypothesize that PSI's many aromatic moieties—representing >15% of its peptide side-chains[39]—provide sites for grafted initiation and attachment that promote intimate interconnectivity between PSI and the included polymer. As evidence, while vpPEDOT films on FTO substrates delaminate rapidly upon aqueous rinsing, PSI:vpPEDOT films do not. We assembled PSI:vpPEDOT films on gold substrates to assess the optical, structural, and electrochemical characteristics of our VPP composite films. We find our method neither incurs significant modification of PSI secondary structure nor disturbs the packing of formed PSI multilayers. This simple and highly adaptable vapor-phase technique is a viable tool for study and optimization of solid-state PSI:ICP film assemblies.

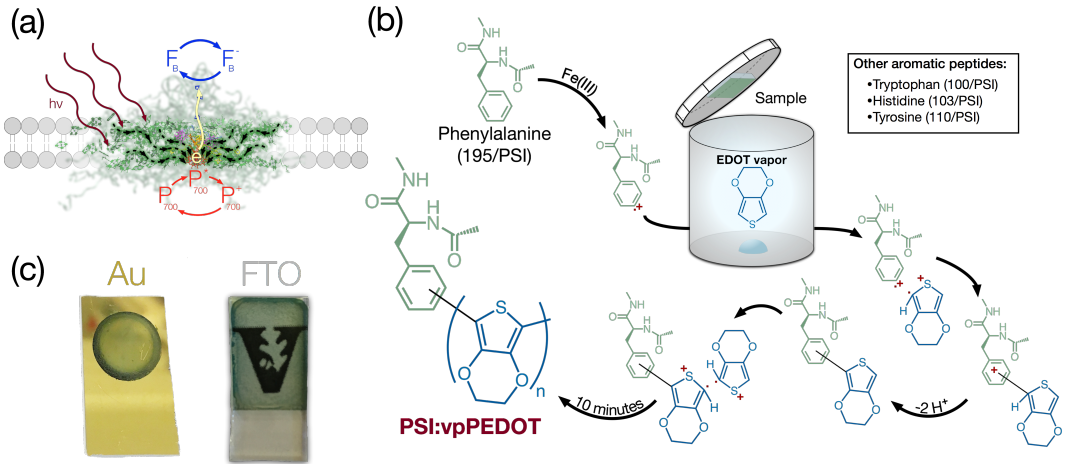

Figure 5.1. Vapor-Phase Assembly of PSI:vpPEDOT. PSI is a highly stable, naturally abundant photodiode that efficiently converts sunlight into prolonged reduction potential. (b) PSI can be incorporated into ICP films through a straightforward vapor-phase polymerization procedure. Drop cast films of PSI proteins replete with a Friedel–Crafts catalyst are exposed to EDOT monomer vapor to achieve rapid polymer growth. Radical cations formed on PSI's many aromatic side chains during polymerization can act as grafting points to monomer species for intimate polymer/protein association. (c) Our technique permits fabrication of composite PSI:ICP films on many substrates, including gold and FTO.

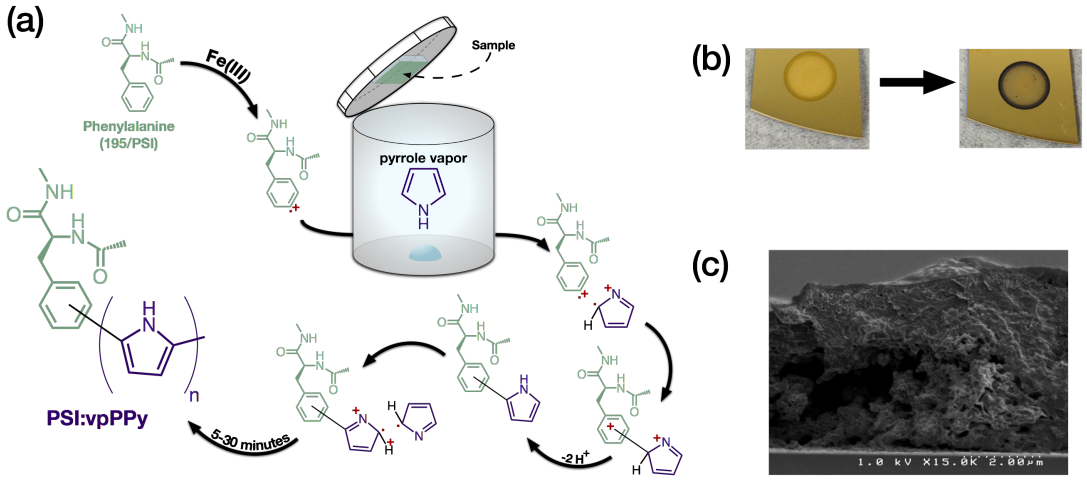

Figure 5.2. Vapor-Phase Assembly of PSI:vpPPy. (a) We propose that a similar 'grafting-from' mechanism applies to vpPPy films grown in the presence of PSI to form PSI:vpPPy. (b) We successfully grew dense PPy from catalyst-replete PSI multilayer films in minutes using our technique. (c) Cross-sectional SEM of composite film.

Results and Discussion

PM-IRRAS of PSI:vpPEDOT

PM-IRRAS was used to characterize the chemical composition and structural features of PSI, vpPEDOT, and PSI:vpPEDOT films on gold substrates functionalized with a SAM from AET (**Figure 5.3**). PEDOT's inter-ring stretching at 1525 cm^{-1} is evident in films of both vpPEDOT and PSI:vpPEDOT.[34,37,40,41] Additionally, composite films assimilate PSI's Amide I and Amide II peaks that represent protein C=O and N–H/C–N vibrational modes with maximum absorption at 1662 cm^{-1} and 1545 cm^{-1}, respectively.[42–44] We deconvolved the Amide I peaks into contributions from structural elements including alpha-helix, beta-sheet, beta-turn, and unordered helix, as described previously by this group.[8] We observe limited deviation in secondary structure between PSI stabilized in a multilayer film and that in a composite PSI:vpPEDOT assembly and conclude that

prerequisite processing conditions—including the introduction of $FeCl_3$ to PSI solutions and rapid PEDOT growth within dry films—have only minor effects on PSI secondary structure.

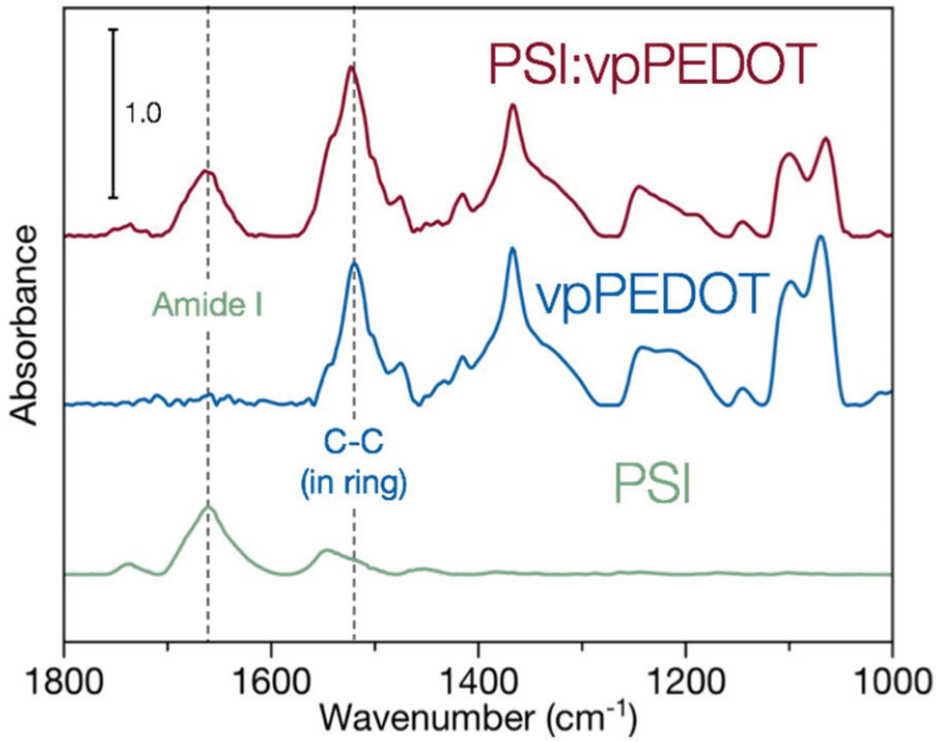

Structural Element	PSI	PSI:vpPEDOT
α-helix	37±2%	32±2%
β-sheet	37±2%	38±3%
β-turn	18±1%	22±1%
Unordered helix	9±1%	8±1%

Figure 5.3. PM-IRRAS of PSI:vpPEDOT, vpPEDOT, and PSI Films. (a) Scans reveal incorporation of PSI amide structure and PEDOT inter-ring stretching. (b) Deconvolution of Amide I into its component structural elements reveals limited modification of protein secondary structure.

Visible Absorbance and Thickness

We characterized the absorbance spectra of the center regions of vpPEDOT, PSI, and PSI:vpPEDOT films in red light (**Figure 5.4a**). vpPEDOT films exhibit limited red absorbance, as π–π* and polaronic optical transitions occur for yellow/orange (580–600 nm) and infrared (830–950 nm) light, respectively.[37] PSI and PSI:vpPEDOT films incorporate the characteristic absorbance of bound chlorophyll A (ChlA). Water evaporation during film assembly stimulates capillary flows within the drying droplet that displace PSI macromolecules to the three-phase contact line. As a result, PSI accumulation within the dry film interior is attenuated and a so-called coffee ring is formed.[45,46] Accordingly, the normalized absorbance at 672 nm suggests low PSI thickness in the center of the film at a PSI concentration of ~0.6 μM in the drop cast solution. Absorbance increases linearly with PSI concentration from 0.6 μM to 2.4 μM, consistent with the formation of a multilayer film (**Figure 5.4b**).

We used the Beer–Lambert Law to calculate concentrations of ChlA within composite films and related this concentration to a uniform PSI film thickness (t) (eqn (1)),

$$t = \frac{V_{PSI} N_A cos\theta_i}{2\varepsilon\alpha\gamma} A \qquad (1)$$

where ε is the molar absorptivity for ChlA molecules bound within dried PSI multilayer films (64 000 M^{-1} cm^{-1}),[47] θ_i is the angle of light incident at the sample surface (8°), and γ is the fraction of red absorbance that remains after oxidation by Fe^{3+} during film assembly. We determine that ~40% of ChlA absorbance remains after film assembly based on time-resolved observation of solutions containing PSI and $FeCl_3$ (**Figure 5.5**). A is the measured ChlA to PSI ratio (45), N_A is Avogadro's number, and V_{PSI} is the per-unit

volume of PSI packed in a multilayer assembly (954 nm^3).[12]

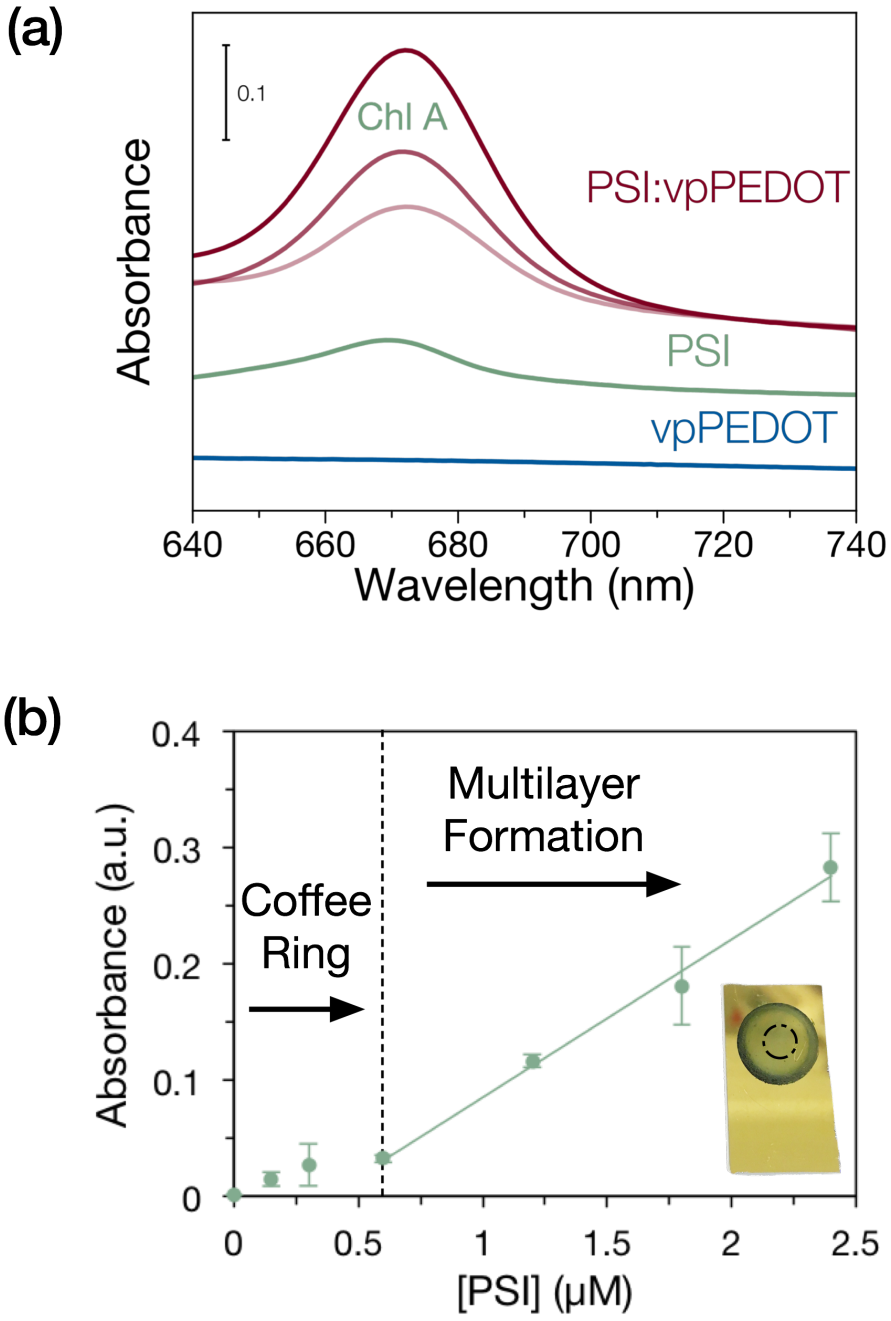

Figure 5.4. Red Light Absorbance of PSI:vpPEDOT, PSI, and PEDOT Films. PSI:vpPEDOT films incorporate the red absorption of antenna ChlA embedded within PSI. Absorbance is proportional to the amount of PSI included in the drop casting solution. (b) Normalized absorbance at 672 nm indicates limited PSI incorporation within the center of films due to coffee ring formation until 0.6 μM PSI, after which films demonstrate linear absorbance change indicative of a densely packed multilayer film.

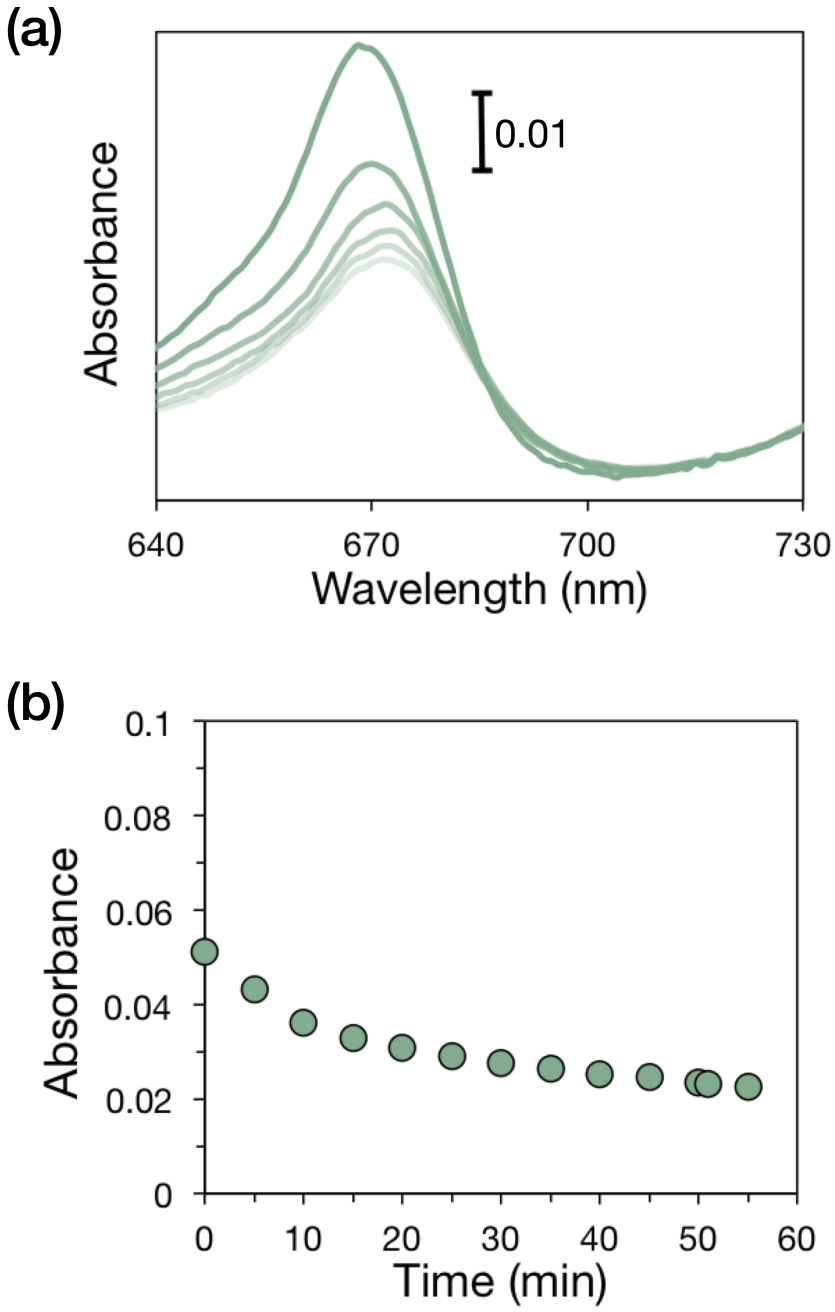

Figure 5.5. PSI Absorbance Decay with Exposure to $FeCl_3$. (a) Visible absorbance measurements of PSI solutions containing $FeCl_3$ reveal transient decay of red absorbance due to peripheral ChlA in PSI proteins. (b) Time-resolved peak red absorbance of a solution containing PSI and $FeCl_3$ oxidant demonstrates oxidation of PSI's chlorophyll network before film assembly. The cuvette contained 2450 µL of a 10 mM $FeCl_3$ and 0.025% w/v Triton X-100 solution and 50 µL dialyzed PSI solution.

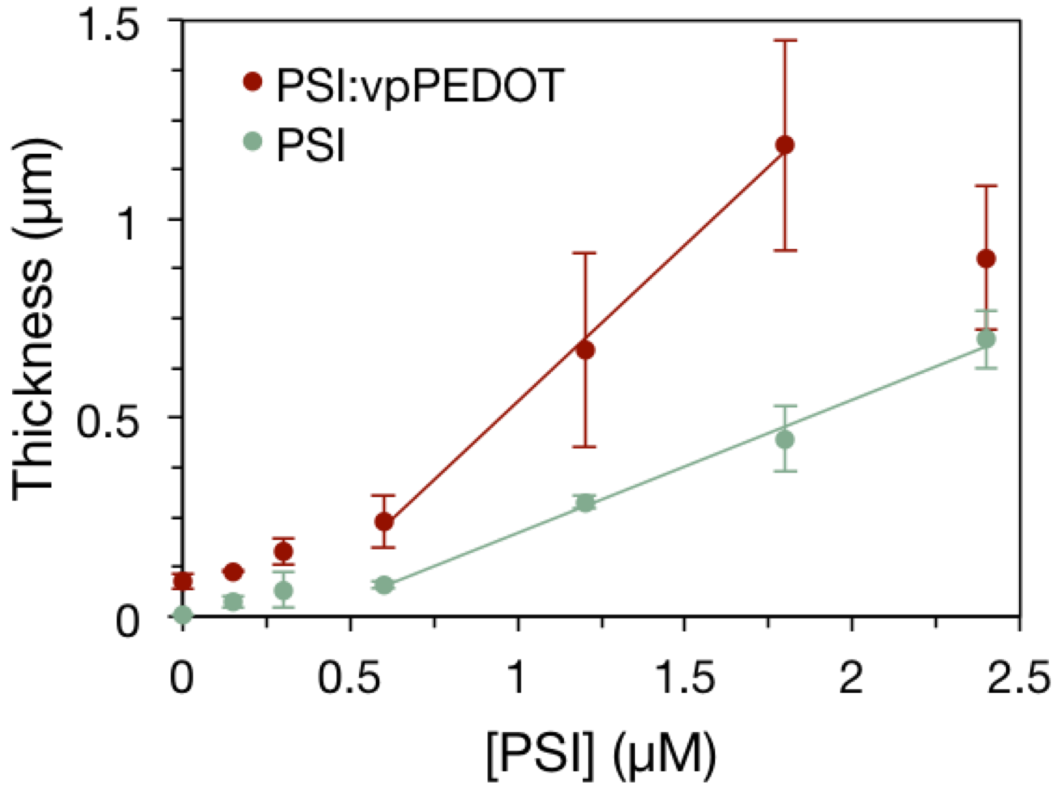

Figure 5.6. Thickness Comparison of PSI:vpPEDOT and Incorporated PSI. Absorbance data are used to calculate the thicknesses of the underlying PSI film within PSI:vpPEDOT films prepared with varying concentrations of PSI in the drop cast solution. We find that higher incorporation of PSI leads to increases in composite thickness, which we attribute to PEDOT grown during vapor-phase polymerization.

We measured the thickness of PSI:vpPEDOT films using profilometry and observed that this overall thickness exceeds that of the incorporated PSI film as determined by absorbance (**Figure 5.6**). We propose that this thickness disparity is the result of robust polymer growth, facilitated by three-dimensional dispersal of $FeCl_3$ within the PSI film during drop casting. Polymer growth could conceivably promote various film structures, including bilayer, heterojunction, or mixed morphology. We used EDX spectroscopy to characterize the cross-sectional morphology of composite films

prepared with solutions containing 1.8 μM and 2.4 μM PSI (**Figure 5.7a**). The location and relative prevalence of PSI and PEDOT were resolved by probing for atomic concentrations of nitrogen and sulfur, respectively, along line scans starting at the gold surface and ending at the composite film's extent. The y-axis of our line scan analysis is presented as N/(S + N); accordingly, unmixed PEDOT and PSI regions will yield approximate values of 0 and 1, respectively. For the composite film prepared with 1.8 μM PSI, we observe two distinct regions: a lower region corresponding to a mixed sulfur/nitrogen region and an upper layer incorporating negligible nitrogen. Given the matchup between the thickness of elemental transition in EDX and the predicted uniform PSI multilayer thickness from visible absorbance measurements, we conclude that this lower film region is a packed PSI multilayer film with PEDOT incorporated throughout. PEDOT overgrowth is also supported by SEM of PSI:vpPEDOT films, which reveal films to be composed of distinct layers of disparate electron emissivity (**Figure 5.7b**).

For the film prepared with 2.4 μM PSI, EDX linescans reveal constant N/(S + N) throughout that is approximately equal to that of the lower film region for composite films prepared with 1.8 μM PSI (0.8). This observation is consistent with negligible thickness difference between the PSI multilayer and overall composite thickness for films prepared with 2.4 μM PSI (**Figure 5.6**). We conclude that the PEDOT overlayer was removed by post-polymerization rinse, and that in this case the profilometric thickness approximates the thickness of the PEDOT-permeated PSI multilayer film.

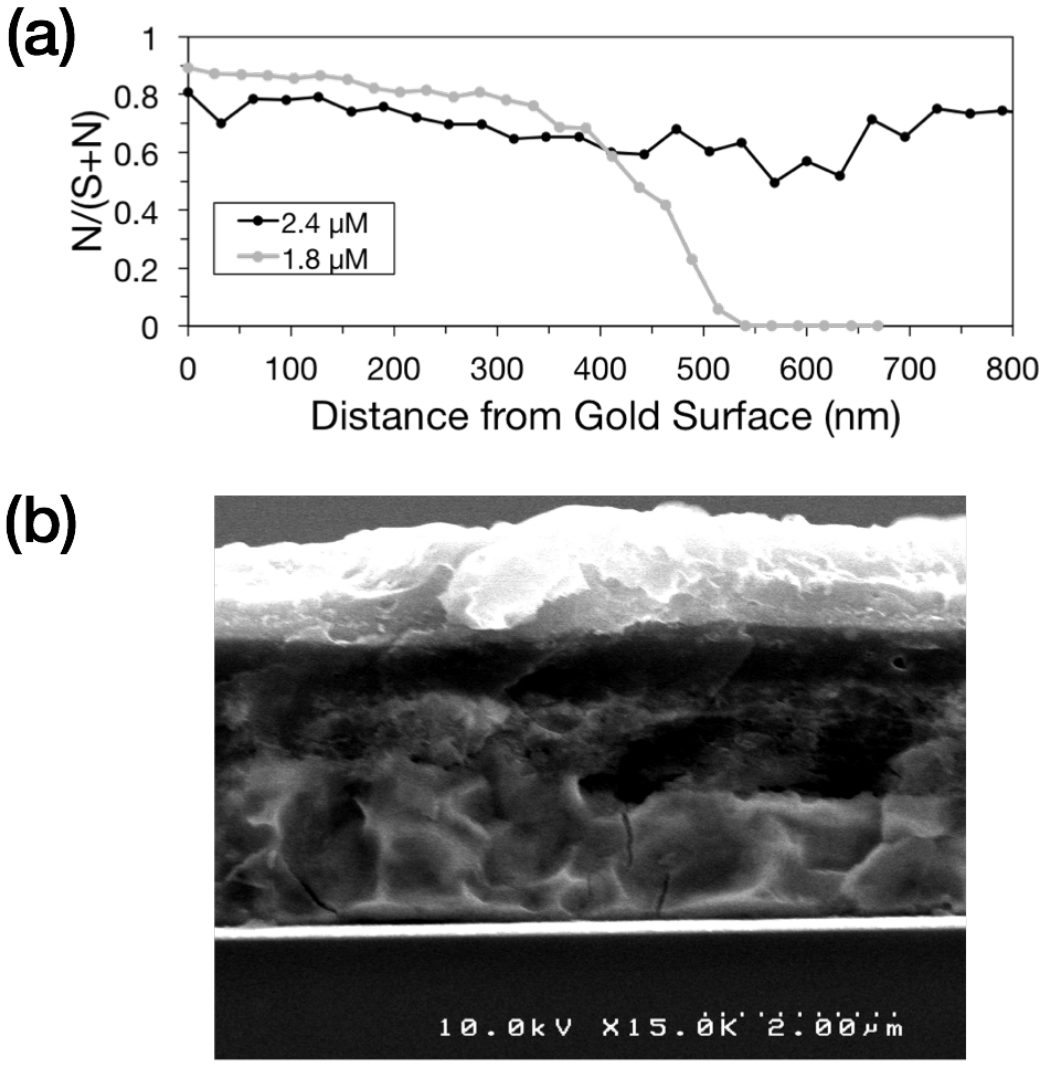

Figure 5.7. EDX of PSI:vpPEDOT Films. (a) EDX line scans indicate PEDOT growth throughout and above a catalyst-replete PSI multilayer film. (b) Cross-sectional SEM images of PSI:vpPEDOT films reveal highly electron-emissive PEDOT overgrowth atop a less-emissive region containing PSI and PEDOT.

Electrochemical Impedance Spectroscopy of PSI:vpPEDOT Films

EIS spectra for Au/AET, Au/AET/PSI, Au/AET/vpPEDOT, and Au/AET/PSI:vpPEDOT films were collected in aqueous KCl (**Figure 5.8**). Scans reveal a common high frequency resistance of the bulk solution (~40 Ω) and a capacitance related to ion adsorption to the underlying electrode and within the film structure. Therefore, we model our electrochemical cells as series circuits consisting of a resistor for the solution and a constant phase element for the film. A constant phase element accounts for coupled phenomena that result in non-ideal capacitance (eqn (2)).

$$Z_{CPE} = \frac{1}{Y_O(j\omega)^n} \quad (2)$$

The ideality constant, n, restricts the phase angle of capacitive behavior to a constant below the 90° threshold for a pure capacitor. Specifically, n = 1 indicates ideal capacitance (90°), n = 0.5 corresponds to a diffusion-controlled response (45°), and n = 0 represents a pure resistor (0°). For all films examined, we observe ideality constants near 1, and will thus refer to Y_o as the capacitance throughout the remainder of the text.

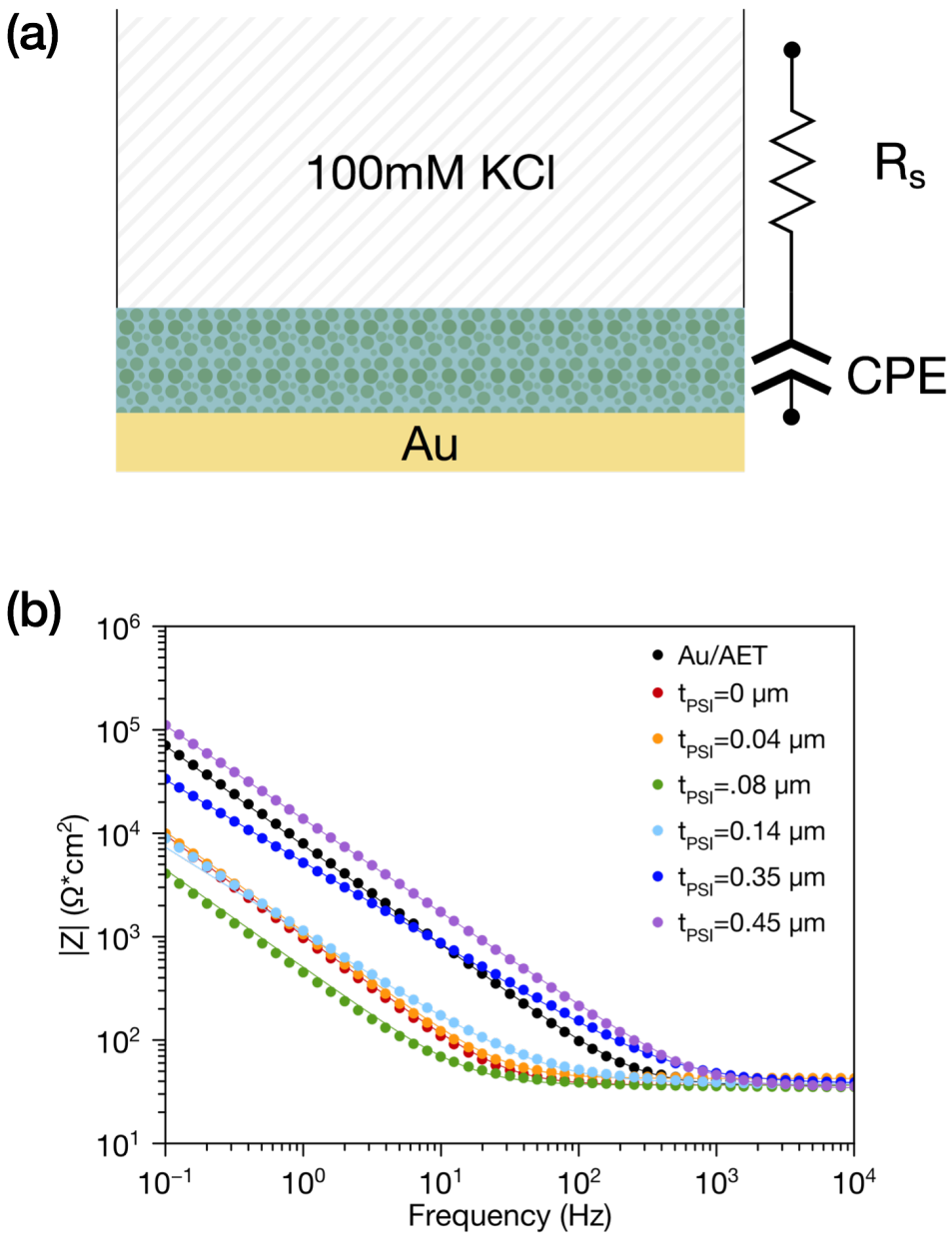

Figure 5.8. EIS of PSI:vpPEDOT Films. (a) Spectra were fit to a series circuit consisting of a resistor corresponding to pure solution resistance and a constant phase element (CPE) which models the pseudocapacitance of incorporated PEDOT. (b) PSI incorporation significantly modifies the psuedocapacitance of a vpPEDOT film. All spectra were collected in 100 mM KCl.

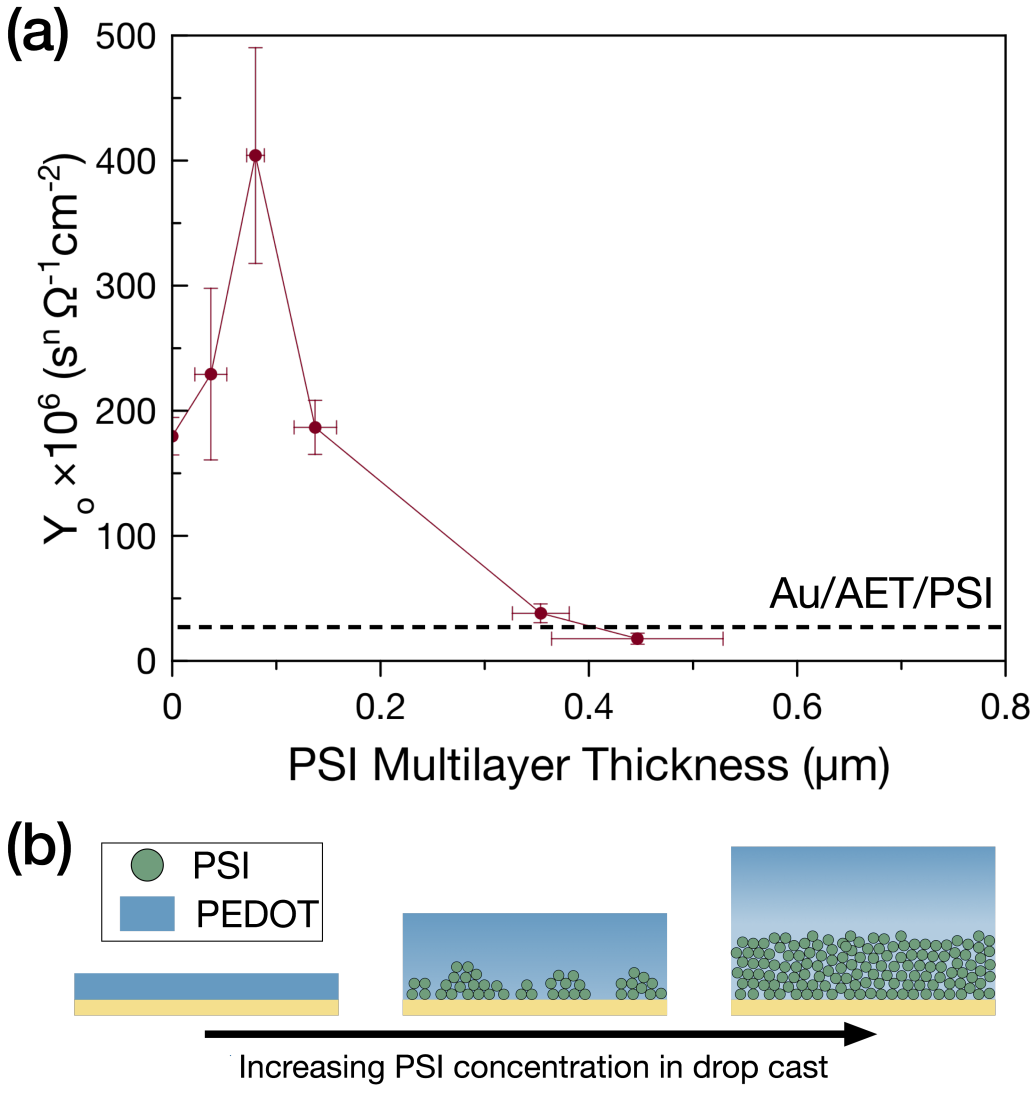

Figure 5.9. PSI:vpPEDOT Capacitance with Variable PSI Incorporation. PSI incorporation within PSI:vpPEDOT films has significant effects on the pseudo-capacitance of grown PEDOT. (a) Thin PSI films include pinholes that permit augmented polymer growth but also robust connection to the underlying electrode. Thicker films decrease the density and length of polymer chains within the PSI film and occlude a PEDOT/electrode connection, which reduces the pseudo-capacitance of these films. (b) Visual model of changes in composite structure with increasing PSI multilayer thickness.

Due to their high porosity[48] and wettability,[49] PSI films do not exhibit capacitance significantly different than that of an AET-modified surface. However, PSI:vpPEDOT films demonstrate capacitance many times that of a PSI film due to pseudo-capacitance (**Figure 5.9**). Electrons injected into a PEDOT film can stimulate doping/de-doping reactions by which anions from a contacting solution are reversibly adsorbed to and desorbed from PEDOT's positively charged backbone.[50,51] In this way, the potential sweep of a PEDOT-modified electrode captures much more charge relative to its unmodified equivalent, and a greatly enhanced capacitance is observed.

We relate the capacitance of PSI:vpPEDOT films prepared with constant $FeCl_3$ and variable PSI concentration to the density and location of PEDOT within the composite film structure. Based on our analysis of absorbance and EDX, we assume that incremental increase in PSI loading in drop cast films contributes to a thicker PSI multilayer at the base of the grown PEDOT. We identify two unique capacitance regions and discuss each in order of incorporated PSI film thickness.

First, between 0 μm and 0.1 μm PSI film thickness, PSI:vpPEDOT capacitance increases due to enhanced polymer surface area available for doping/de-doping interactions (eqn (3)),

$$C = \varepsilon_r \varepsilon_o \frac{A}{d} \tag{3}$$

where C is the film capacitance, ε_r is the relative permittivity, ε_o is the vacuum permittivity (8.854 x 10^{-12} F m^{-1}), d is the film thickness, and A is the total surface area available for ion interaction. This first thickness region is below the threshold for the formation of a well-packed PSI multilayer assembly (**Figure 5.6**), and thus, the prevalence of pinholes throughout the sparse PSI film contributes to a robust coupling

between PEDOT and the gold electrode beneath (**Figure 5.9b**).

However, in excess of 0.1 μm PSI film thickness, PSI:vpPEDOT capacitance decreases rapidly, an observation that runs counter to numerous studies of PEDOT films in which psuedo-capacitance is observed to increase with thickness in excess of 10 μm.[52–54] We attribute reduced capacitance to PSI's imposed spatial constraints on polymer growth; a packed PSI film occludes electrode/PEDOT connection while also minimizing the free volume for polymer growth. In addition, PSI's polypeptide chains include numerous aromatic side-chains with which a polymer-terminating grafting reaction can occur, leading to short-chain PEDOT oligomers with diminished pseudo-capacitive capability. During polymerization, $FeCl_3$ stimulates radical cation formation in many aromatic moieties, including EDOT monomers and PEDOT oligomers but also aromatic polypeptide side-chains.[55] Thus, the ~2000 aromatic side-chains per PSI[39] can conceivably act as sites for polymer initiation (grafting-from) but also irreversible polymer termination (grafting-to) that yields reduction in polymer molecular weight in the PSI film relative to those grown unobstructed. Chain discontinuities in the underlying PSI:vpPEDOT layer diminish electron transfer from the underlying gold electrode to the enveloping PEDOT layer and thus lower this upper layer's pseudo-capacitive response.

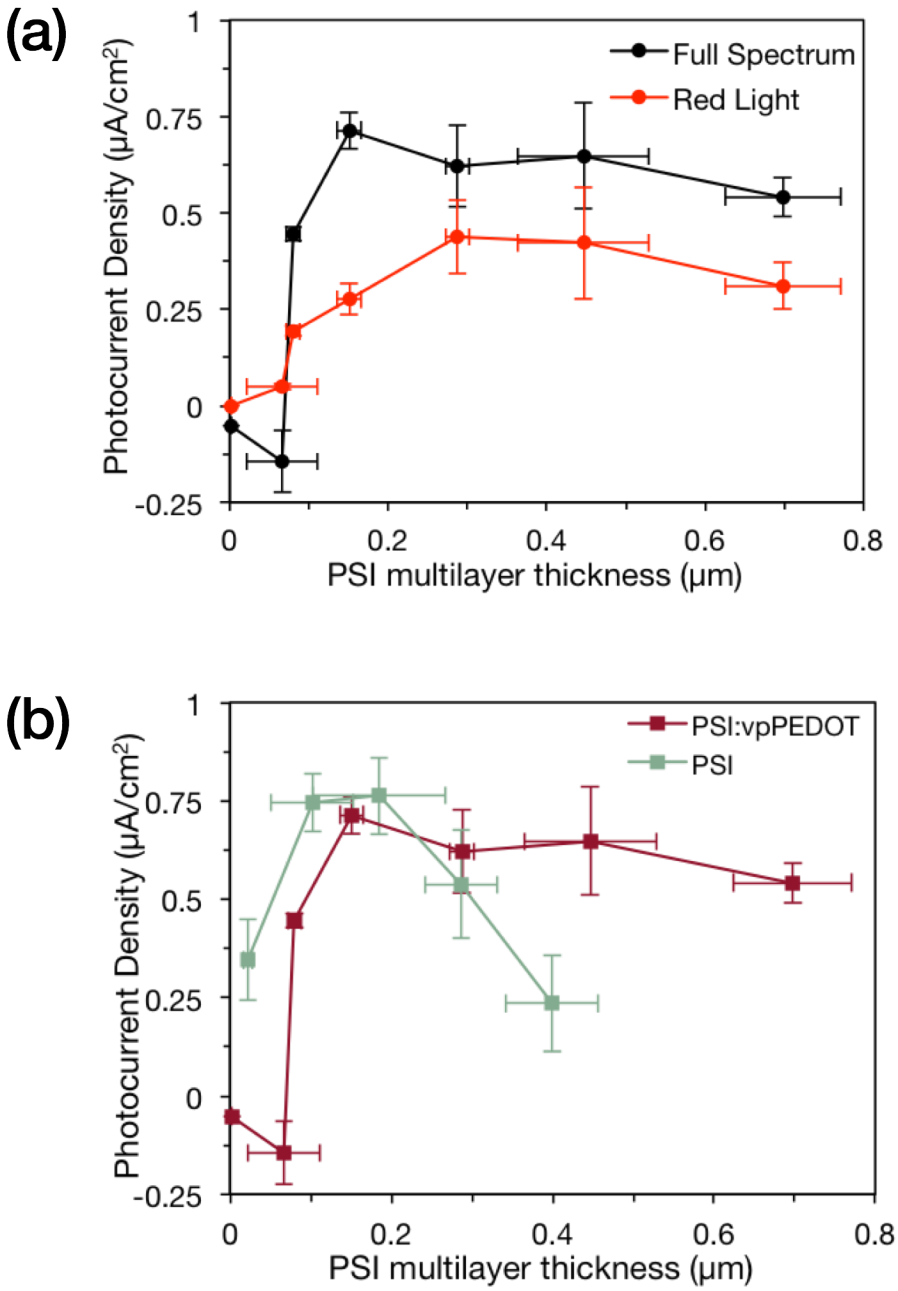

Figure 5.10. PSI:vpPEDOT Photocurrent *vs.* Incorporated PSI Multilayer Thickness. PSI:vpPEDOT films demonstrate photoresponse akin to that of unmodified PSI multilayer assemblies. (a) We observe a relationship between PSI loading and cathodic photocurrents under full spectrum and filtered red light. (b) Composite films sustain near-maximum photocurrents for PSI films many hundred nanometers in excess of that of unmodified PSI films, which we attribute to PEDOT behaving as an extension of the underlying gold electrode to permit more rapid supply of electrons to PSI proteins. All films were tested in an aqueous electrolyte containing 20 mM sodium ascorbate, 1 mM DCPIP, and 100 mM KCl.

Photoelectrochemical Performance of Composite Films

We tested PSI:vpPEDOT films in an Asc/DCPIP electrolyte to elucidate their photocathodic response (**Figure 5.10**).[13,14,49,56,57] Briefly, the purple, blue, and red light absorption of a PSI film stimulates rapid photoelectron generation and charge injection into water-soluble mediators, modifying their concentrations at the electrode surface such that a potential change develops as described by the Nernst equation (eqn (4)),[58]

$$\Delta E = \frac{RT}{nF} ln \left[\left(\frac{C_R^*}{C_O^*} \right) \left(\frac{C_O(t,0)}{C_R(t,0)} \right) \right] \quad (4)$$

where C_O and C_R are the concentrations of oxidized and reduced mediator species at the electrode surface, respectively. C_O^* and C_R^* are the bulk concentrations of oxidized and reduced mediator species, respectively.

Under controlled electrode potential, the potentiostat drives current to compensate for the changes in reduced and oxidized species, as expressed by the heterogeneous current–overpotential relationship for a reversible redox couple (eqn (5)),[58]

$$j = j_o \left[\frac{C_O(t,0)}{C_O^*} e^{-\alpha f \eta} - \frac{C_R(t,0)}{C_R^*} e^{(1-\alpha) f \eta} \right] \quad (6)$$

where j_o is the exchange current density, α is the transfer coefficient, η is overpotential, and f is nF/RT.

With no PSI included in the polymer layer, we observe small anodic photocurrent under full spectrum (~−0.05 μA cm^{-2}) attributed to PEDOT's π–π* transition (~580–600 nm). At low loadings of PSI within the vpPEDOT layer, we observe an increase in anodic photocurrent due to an increase in PEDOT density near the electrode surface, consistent with our discussion of capacitance. However, further PSI incorporation yields a cathodic response that reaches a limiting value of 0.7 μA cm^{-2} for composite films incorporating a

~150 nm thick PSI multilayer. A decrease in PEDOT density—the result of imposed limits on free volume and polymer growth kinetics—decreases the conjugation length of PEDOT near the surface and diminishes PEDOT's contributions to the photoresponse of the film.

The application of a low-pass red light filter permits us to study the photocatalytic response of PSI within composite films without stimulating PEDOT's optical transitions. We observe a ~70% decrease in the photocurrent response of PSI:vpPEDOT that is proportional to the decrease in the intensity of the light source with filtering. Provided the pronounced red light absorption of PSI:vpPEDOT films (**Figure 5.10**), our photocurrent response is attributed overwhelmingly to PSI embedded within the film. Additionally, PCA with composite films containing PSI inactivated by exposure to high intensity UV light demonstrate negligible photocurrent (**Figure 5.11**).

We compared PSI:vpPEDOT and unmodified PSI multilayer film photocurrents with varying PSI film thickness (**Figure 5.10b**). In an Asc/DCPIP redox electrolyte, unmodified PSI multilayer films generate maximum photocurrent at ~150 nm film thickness; thicker films result in photocurrent attenuation. On the other hand, PSI:vpPEDOT films are observed to follow a similar upward photocurrent trend with thickness, but maintain near-maximum photocurrent for several hundred nanometers in excess of unmodified PSI films. We attribute this to integrated PEDOT extending the electrode surface within the film, thereby reducing distance-dependent photocurrent attenuation. PSI:vpPEDOT films were also tested for photocurrent in electrolyte solutions containing KCl, dissolved O_2, and methyl viologen—a well-known electron acceptor from F_B—and solutions containing only KCl and dissolved O_2. For both of

these electrolytes, PSI:vpPEDOT films demonstrate cathodic photocurrents not present for either pure PEDOT or pure PSI films; this demonstrates that the included PEDOT does indeed provide a route of electron transfer from the underlying gold electrode to P_{700}^{+} in PSI incorporated within the composite film (**Figure 5.12**).

Conclusions

We have successfully incorporated PEDOT, a highly conductive and environmentally stable ICP, within PSI multilayer films using a rapid vapor-phase technique that is an adaptation of our previously developed vacuum-assisted method. We find that the additional processing required neither disrupts the secondary structure of a PSI film nor compromises its photocatalytic capacity. We find that composite films are comprised of a PEDOT-inundated PSI multilayer film and an enveloping PEDOT layer with thickness commensurate to the PSI loading. PSI:vpPEDOT films demonstrate pseudo-capacitance due to incorporated PEDOT that depends strongly on the PSI loading within the film. Finally, we observe that PSI:vpPEDOT films produce more photocurrent than unmodified PSI films at higher thickness due to incorporated PEDOT's extension of the electrode surface. We suggest that this novel and highly adaptable PSI:ICP preparation technique is a tool toward optimized solid-state biophotovoltaic design.

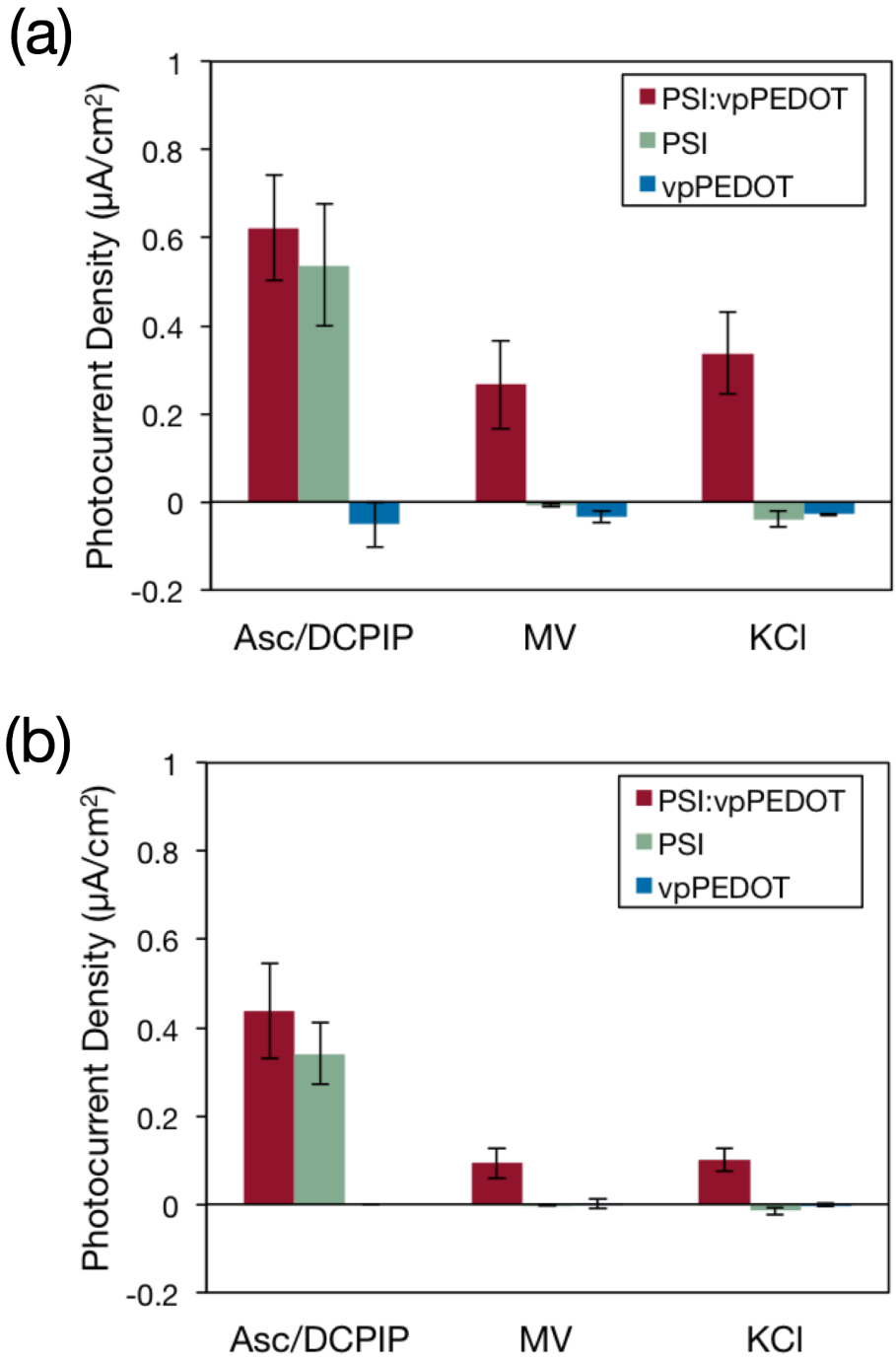

Figure 5.11. PSI:vpPEDOT Photocurrent with Different Mediators. Photocurrent measurements were performed on PSI:vpPEDOT (tPSI~300 nm), PSI (t_{PSI}~300 nm), and vpPEDOT films prepared on Au/AET electrodes in 20 mM Asc/1 mM DCPIP, 0.5 mM methyl viologen (MV), and with no added redox mediator. All solutions contain 100 mM KCl as supporting electrolyte and were performed in air. Both (a) full spectrum and (b) red light responses indicate that the addition of PSI within a PEDOT scaffold facilitates a photocathodic response.

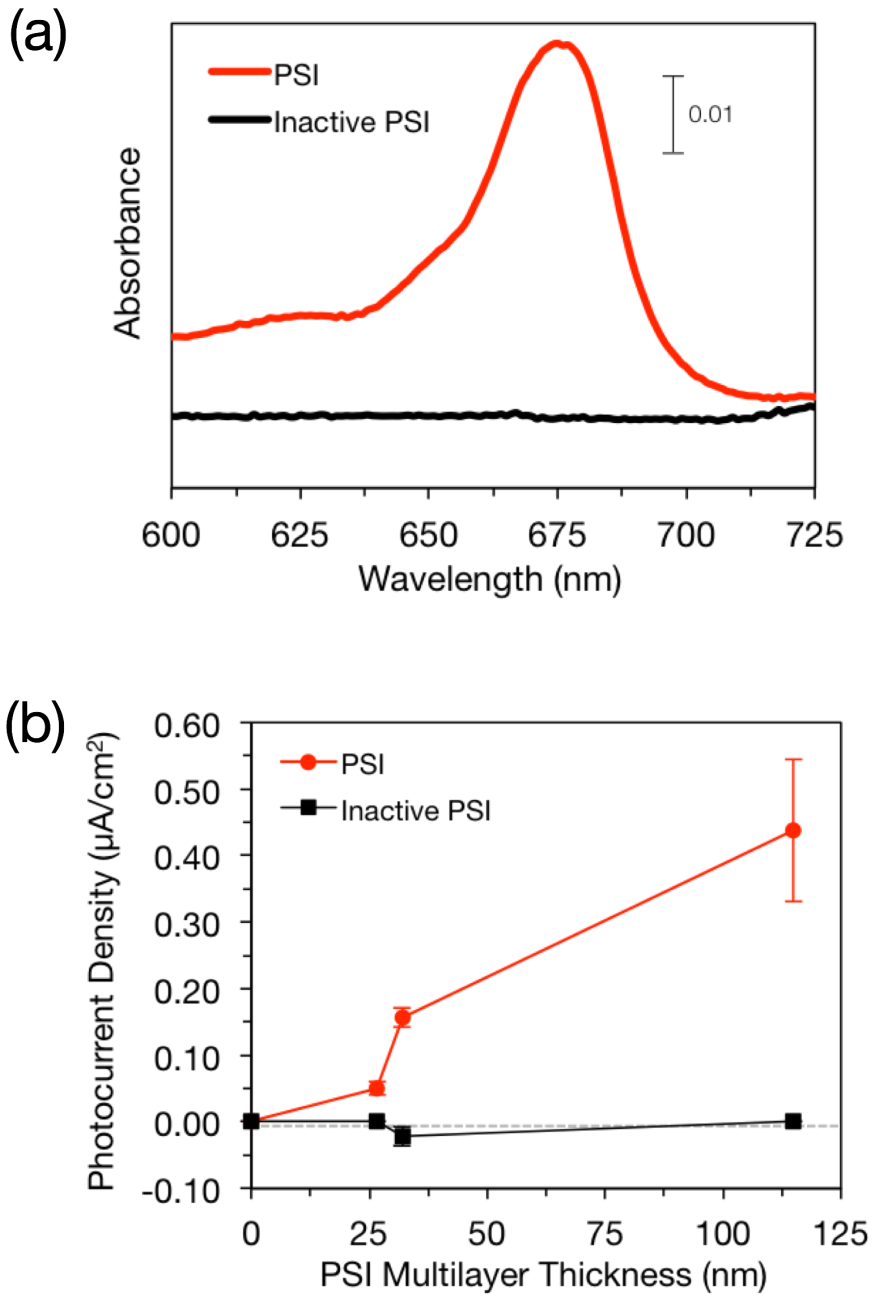

Figure 5.12. Photocurrent Comparison Between PSI:vpPEDOT Films Prepared with Active and Inactive PSI Proteins. To provide further evidence for PSI-based photocurrent in composite films, PSI:vpPEDOT films were prepared with both active and inactive PSI (inPSI). (a) Solution absorbance comparison of unmodified PSI and inactive PSI prepared by prolonged UV-irradiation of PSI solution. Measurements were collected for a mixture of 50 µL inactive/unmodified PSI solution and 2450 µL phosphate buffer (pH 7). (b) Near-zero and cathodic photocurrents are observed for inPSI:vpPEDOT and PSI:vpPEDOT films, respectively, tested under filtered red light in an electrolyte solution containing 20 mM Asc, 1 mM DCPIP, and 100 mM KCl.

Experimental Methods

PSI Extraction and Isolation

PSI was extracted from commercially available spinach as described previously.[8] Solutions were subsequently dialyzed to decrease concentrations of salts and surfactants. Briefly, baby spinach leaves were de-veined and macerated. Filtered solutions were centrifuged at 8000 g, and the pellet was resuspended in Triton X-100 to lyse thylakoid membranes. This solution was centrifuged at 20 000 g and the supernatant was introduced slowly atop a chilled hydroxylapatite column. Purified protein solutions were removed in 1 mL aliquots and stored at −80 °C. Solutions were dialyzed for 12 h using 10 000 MWCO dialysis tubing (Spectrum Labs). Using a previously described method, [P_{700}] was determined to be 1 μM with 45 chlorophylls per reaction center.[59]

Gold Electrode Preparation

Chromium (10 nm) and gold (125 nm) were deposited sequentially atop a <100> silicon support using a previously described thermal deposition process.[49,56] Gold electrodes were rinsed vigorously in ethanol and placed in a vial containing a ~1 mM aminoethane thiol (AET, Acros) solution in ethanol for 12 h to provide a hydrophilic surface for film deposition.

Control of PSI Concentration

180 μL of freshly dialyzed PSI solution was centrifuged at 16 000 g for 30 min and the pellet resuspended in a variable volume of an aqueous solution containing 10 mM $FeCl_3$ and 0.025% w/v Triton X-100. PSI concentration was subsequently quantified

using the methods of Baba *et al.* for solutions resuspended in deionized water.[60]

PSI/Catalyst Film Deposition

A solution containing 10 mM $FeCl_3$, 0.025% w/v Triton X-100, and a chosen PSI concentration was drop cast atop AET/gold substrates masked with plater's tape (Gamry Instruments) with an exposed area of 1 cm^2. Vacuum was applied to leave behind a film of PSI, catalyst, and surfactant. The plater's tape mask was removed before subsequent polymerization.

Vapor-Phase Growth of PEDOT

20 μL of EDOT monomer was deposited into a 25 mL glass vial. A dried, drop cast film containing PSI, $FeCl_3$, and Triton X-100 were introduced into the vial at room temperature. The vials were sealed and lowered into a water bath at 40 °C to stimulate vapor-phase growth. After 10 min, the reaction vials were removed from the water bath and opened. The resulting films were rinsed vigorously in deionized water and dried under a stream of nitrogen.

Electrochemical Impedance Spectroscopy (EIS)

All impedance measurements were conducted in the dark using a Gamry Instruments CMS300 impedance system. A three-electrode assembly was used with a platinum counter electrode, Ag/AgCl reference electrode, and custom-built sample holder. The tested film/gold sample served as the working electrode, and the electrochemically accessible area was constrained to 0.28 cm^2 using hole-punched

plater's tape. All measurements were performed in 100 mM KCl in deionized water (18.2 MΩ).

Structural Deconvolution from Polarization Modulation-Infrared Reflection Absorption Spectroscopy (PM-IRRAS)

PM-IRRAS was conducted on films atop reflective gold substrates using a Bruker FTIR spectrometer with a liquid nitrogen-cooled, mercury-cadmium-telluride detector and light incident at 80° from the substrate surface normal. Spectra were collected at 4 cm^{-1} resolution and deconvoluted using the Lorentzian fitting software available from the University of Maryland.[61]

Scanning Electron Microscopy (SEM)

SEMs of PSI:vpPEDOT film cross-sections were taken with a Hitachi S-4200 SEM using an accelerating voltage of 10 kV.

Energy Dispersive X-ray (EDX) Spectroscopy

Cross-sectional EDX was carried out on PSI:vpPEDOT samples using a Zeiss Merlin scanning electron microscope equipped with an Oxford Instruments X-ray detector (Model: 51-XMX1025). All linescans were taken at 10 kV accelerating voltage and a current of 4 nA.

Photoelectrochemical Characterization

Photochronoamperometry (PCA) was performed using a three-electrode assembly

and a CH660a potentiostat equipped with a Faraday cage. Ag/AgCl reference and platinum mesh counter electrodes were used in combination with the film/gold sample, which served as the working electrode. The photoelectrochemically active area during experiments was constrained to 0.28 cm^2 using plater's tape. A 250 W cold light source (Leica KL 2500 LCD, 140 mW cm^{-2}) with a spectral window of 380–790 nm was used to irradiate films. Red light measurements were conducted by applying an optical low-pass filter with a 633 nm cutoff (95 mW cm^{-2}). All PCA measurements were performed using a redox electrolyte containing 20 mM sodium ascorbate (Asc), 1 mM dichloroindophenol (DCPIP), and 100 mM KCl.

Works Cited

(1) Hogewoning, S. W.; Wientjes, E.; Douwstra, P.; Trouwborst, G.; van Ieperen, W.; Croce, R.; Harbinson, J. Photosynthetic Quantum Yield Dynamics: From Photosystems to Leaves. *Plant Cell* **2012**, *24*, 1921–1935.

(2) Nelson, N.; Yocum, C. F. Structure and Function of Photosystems I and II. *Annu. Rev. Plant Biol.* **2006**, *57*, 521–565.

(3) Krassen, H.; Schwarze, A.; Friedrich, B.; Ataka, K.; Lenz, O.; Heberle, J. Photosynthetic Hydrogen Production by a Hybrid Complex of Photosystem I and [NiFe]-Hydrogenase. *ACS Nano* **2009**, *3*, 4055–4061.

(4) LeBlanc, G.; Chen, G.; Jennings, G. K.; Cliffel, D. E. Photoreduction of Catalytic Platinum Particles Using Immobilized Multilayers of Photosystem I. *Langmuir* **2012**, *28*, 7952–7956.

(5) Mershin, A.; Matsumoto, K.; Kaiser, L.; Yu, D.; Vaughn, M.; Nazeeruddin, M. K.;

Bruce, B. D.; Grätzel, M.; Zhang, S. Self-Assembled Photosystem-I Biophotovoltaics on Nanostructured TiO_2 and ZnO. *Sci. Rep.* **2012**, *2*, 1–7.

(6) Yu, D.; Wang, M.; Zhu, G.; Ge, B.; Liu, S.; Huang, F. Enhanced Photocurrent Production by Bio-Dyes of Photosynthetic Macromolecules on Design TiO_2 Film. *Sci. Rep.* **2015**, *5*, 1–9.

(7) Shah, V. B.; Henson, W. R.; Chadha, T. S.; Lakin, G.; Liu, H.; Blankenship, R. E.; Biswas, P. Linker-Free Deposition and Adhesion of Photosystem I onto Nanostructured TiO_2 for Biohybrid Photoelectrochemical Cells. *Langmuir* **2015**, *31*, 1675–1682.

(8) Kincaid, H. A.; Niedringhaus, T.; Ciobanu, M.; Cliffel, D. E.; Jennings, G. K. Entrapment of Photosystem I within Self-Assembled Films. *Langmuir* **2006**, *22*, 8114–8120.

(9) Feifel, S. C.; Lokstein, H.; Hejazi, M.; Zouni, A.; Lisdat, F. Unidirectional Photocurrent of Photosystem I on π-System-Modified Graphene Electrodes: Nanobionic Approaches for the Construction of Photobiohybrid Systems. *Langmuir* **2015**, *31*, 10590–10598.

(10) Simmerman, R. F.; Zhu, T.; Baker, D. R.; Wang, L.; Mishra, S. R.; Lundgren, C. A.; Bruce, B. D. Engineering Photosystem I Complexes with Metal Oxide Binding Peptides for Bioelectronic Applications. *Bioconjug. Chem.* **2015**, *26*, 2097–2105.

(11) Szewczyk, S.; Giera, W.; Haene, S. D.; Grondelle, R. Van. Comparison of Excitation Energy Transfer in Cyanobacterial Photosystem I in Solution and Immobilized on Conducting Glass. *Photosynth. Res.* **2016**.

(12) Ciesielski, P. N.; Faulkner, C. J.; Irwin, M. T.; Gregory, J. M.; Tolk, N. H.; Cliffel,

D. E.; Jennings, G. K. Enhanced Photocurrent Production by Photosystem I Multilayer Assemblies. *Adv. Funct. Mater.* **2010**, *20*, 4048–4054.

(13) Ciesielski, P. N.; Hijazi, F. M.; Scott, A. M.; Faulkner, C. J.; Beard, L.; Emmett, K.; Rosenthal, S. J.; Cliffel, D.; Jennings, G. K. Photosystem I - Based Biohybrid Photoelectrochemical Cells. *Bioresour. Technol.* **2010**, *101*, 3047–3053.

(14) Chen, G.; LeBlanc, G.; Jennings, G. K.; Cliffel, D. E. Effect of Redox Mediator on the Photo-Induced Current of a Photosystem I Modified Electrode. *J. Electrochem. Soc.* **2013**, *160*, H315–H320.

(15) LeBlanc, G.; Chen, G.; Gizzie, E. A.; Jennings, G. K.; Cliffel, D. E. Enhanced Photocurrents of Photosystem I Films on P-Doped Silicon. *Adv. Mater.* **2012**, *24*, 5959–5962.

(16) LeBlanc, G.; Winter, K. M.; Crosby, W. B.; Jennings, G. K.; Cliffel, D. E. Integration of Photosystem I with Graphene Oxide for Photocurrent Enhancement. *Adv. Energy Mater.* **2014**, *4*, 1–5.

(17) Gunther, D.; LeBlanc, G.; Prasai, D.; Zhang, J. R.; Cliffel, D. E.; Bolotin, K. I.; Jennings, G. K. Photosystem I on Graphene as a Highly Transparent, Photoactive Electrode. *Langmuir* **2013**, *29*, 4177–4180.

(18) Badura, A.; Guschin, D.; Kothe, T.; Kopczak, M. J.; Schuhmann, W.; Rögner, M. Photocurrent Generation by Photosystem 1 Integrated in Crosslinked Redox Hydrogels. *Energy Environ. Sci.* **2011**, *4*, 2435.

(19) Kothe, T.; Pöller, S.; Zhao, F.; Fortgang, P.; Rögner, M.; Schuhmann, W.; Plumeré, N. Engineered Electron-Transfer Chain in Photosystem 1 Based Photocathodes Outperforms Electron-Transfer Rates in Natural Photosynthesis.

Chem. Eur. J. **2014**, *20*, 1–7.

(20) Stieger, K. R.; Ciornii, D.; Kölsch, A.; Hejazi, M.; Lokstein, H.; Feifel, S. C.; Zouni, A.; Lisdat, F. Engineering of Supramolecular Photoactive Protein Architectures: The Defined Co-Assembly of Photosystem I and Cytochrome c Using a Nanoscaled DNA-Matrix. *Nanoscale* **2016**, *8*, 10695–10705.

(21) Stieger, K. R.; Feifel, S. C.; Lokstein, H.; Lisdat, F. Advanced Unidirectional Photocurrent Generation via Cytochrome c as Reaction Partner for Directed Assembly of Photosystem I. *PCCP* **2014**, *16*, 15667–15674.

(22) Gizzie, E. A.; LeBlanc, G.; Jennings, G. K.; Cliffel, D. E. Electrochemical Preparation of Photosystem I-Polyaniline Composite Films for Biohybrid Solar Energy Conversion. *ACS Appl. Mater. Interfaces* **2015**, *7*, 9328–9335.

(23) Gizzie, E. A.; Scott Niezgoda, J.; Robinson, M. T.; Harris, A. G.; Jennings, G. K.; Rosenthal, S. J.; Cliffel, D. E. Photosystem I-polyaniline/TiO_2 Solid-State Solar Cells: Simple Devices for Biohybrid Solar Energy Conversion. *Energy Environ. Sci.* **2015**, *8*, 3572–3576.

(24) Cho, J.; Shin, K.; Jang, J. Polyaniline Micropattern onto Flexible Substrate by Vapor Deposition Polymerization-Mediated Inkjet Printing. *Thin Solid Films* **2010**, *518* (18), 5066–5070.

(25) Acqua, L. D.; Tonin, C.; Varesano, A.; Canetti, M.; Porzio, W.; Catellani, M. Vapour Phase Polymerisation of Pyrrole on Cellulose-Based Textile Substrates. **2006**, *156*, 379–386.

(26) Khedkar, S. P.; Radhakrishnan, S. Application of Dip-Coating Process for Depositing Conducting Polypyrrole Films. *Thin Solid Films* **1997**, *303*, 167–172.

(27) Li, X.; Lu, W.; Dong, W.; Chen, Q.; Wu, D.; Zhou, W.; Chen, L. Si/PEDOT Hybrid Core/shell Nanowire Arrays as Photoelectrodes for Photoelectrochemical Water- Splitting. *Nanoscale* **2013**, *5*, 5257–5261.

(28) Zuber, K.; Fabretto, M.; Hall, C.; Murphy, P. Improved PEDOT Conductivity via Suppression of Crystallite Formation in Fe(III) Tosylate During Vapor Phase Polymerization. *Macromol. Rapid Commun.* **2008**, *29*, 1503–1508.

(29) Winther-Jensen, B.; Chen, J.; West, K.; Wallace, G. Vapor Phase Polymerization of Pyrrole and Thiophene Using Iron(III) Sulfonates as Oxidizing Agents. *Macromolecules* **2004**, *37* (Iii), 5930–5935.

(30) Nejati, S.; Lau, K. K. S. Chemical Vapor Deposition Synthesis of Tunable Unsubstituted Polythiophene. *Langmuir* **2011**, *27*, 15223–15229.

(31) Kirchmeyer, S.; Reuter, K. Scientific Importance, Properties and Growing Applications of poly(3,4-Ethylenedioxythiophene). *J. Mater. Chem.* **2005**, *15*, 2077.

(32) Bhattacharyya, D.; Howden, R. M.; Borrelli, D. C.; Gleason, K. K. Vapor Phase Oxidative Synthesis of Conjugated Polymers and Applications. *Polym. Phys.* **2012**, *50*, 1329–1351.

(33) Vreeland, R. F.; Atcherley, C. W.; Russell, W. S.; Xie, J. Y.; Laude, N. D.; Porreca, F.; Heien, M. L. Thin Biocompatible PEDOT:Nafion Composite Electrode Coatings for Selective Detection of Neurotransmitters. *Anal Chem.* **2016**, *87*, 2600–2607.

(34) Bhattacharyya, D.; Gleason, K. Single-Step Oxidative Chemical Vapor Deposition of −COOH Functional Conducting Copolymer and Immobilization of Biomolecule

for Sensor Application. *Chem. Mater.* **2011**, *23*, 2600–2605.

(35) Jin, L.; Wang, T.; Feng, Z.-Q.; Leach, M. K.; Wu, J.; Mo, S.; Jiang, Q. A Facile Approach for the Fabrication of Core–shell PEDOT Nanofiber Mats with Superior Mechanical Properties and Biocompatibility. *J. Mater. Chem. B* **2013**, *1*, 1818–1825.

(36) Bongo, M.; Winther-Jensen, O.; Himmelberger, S.; Strakosas, X.; Ramuz, M.; Hama, A.; Stavrinidou, E.; Malliaras, G. G.; Salleo, A.; Winther-Jensen, B.; et al. PEDOT:gelatin Composites Mediate Brain Endothelial Cell Adhesion. *J. Mater. Chem. B* **2013**, *1*, 3860.

(37) Im, S. G.; Yoo, P. J.; Hammond, P. T.; Gleason, K. K. Grafted Conducting Polymer Films for Nano-Patterning onto Various Organic and Inorganic Substrates by Oxidative Chemical Vapor Deposition. *Adv. Mater.* **2007**, *19*, 2863–2867.

(38) Kovacic, P.; Jones, M. B. Dehydro Coupling of Aromatic Nuclei by Catalyst-Oxidant Systems: Poly(p-Phenylene). *Chem. Rev.* **1987**, *87*, 357–379.

(39) Amunts, A.; Drory, O.; Nelson, N. The Structure of a Plant Photosystem I Supercomplex at 3.4 A Resolution. *Nature* **2007**, *447*, 58–63.

(40) Bhattacharyya, D.; Senecal, K.; Marek, P.; Senecal, A.; Gleason, K. K. High Surface Area Flexible Chemiresistive Biosensor by Oxidative Chemical Vapor Deposition. *Adv. Funct. Mater.* **2011**, *21*, 4328–4337.

(41) Im, S. G.; Gleason, K. K. Systematic Control of the Electrical Conductivity of Poly(3,4-Ethylenedioxythiophene) via Oxidative Chemical Vapor Deposition. *Macromolecules* **2007**, *40*, 6552–6556.

(42) Arrondo, J. L. R.; Goñi, F. M. Structure and Dynamics of Membrane Proteins as

Studied by Infrared Spectroscopy. *Prog. Biophys. Mol. Biol.* **1999**, *72*, 367–405.

(43) Seshadri, S.; Khurana, R.; Fink, A. Fourier Transform Infrared Spectroscopy in Analysis of Protein Deposits. *Methods Enzymol.* **1999**, *309*, 559–576.

(44) Ruan, X.; Wei, J.; Xu, Q.; Wang, J.; Gong, Y.; Zhang, X.; Kuang, T.; Zhao, N. Comparison of the Effects of Triton X-100 Treatment on the Protein Secondary Structure of Photosystem I and Photosystem II Studied by FT-IR Spectroscopy. *J. Mol. Struct.* **2000**, *525*, 97–106.

(45) Deegan, R.; Bakajin, O.; Dupont, T.; Huber, G. Capillary Flow as the Cause of Ring Stains from Dried Liquid Drops. *Nature* **1997**, 827–829.

(46) Hu, H.; Larson, R. G. Marangoni Effect Reverses Coffee-Ring Depositions. *J. Phys. Chem. B* **2006**, *110*, 7090–7094.

(47) Hiyama, T.; Ke, B. Difference Spectra and Extinction Coefficients of P700*. *Biochim. Biophys. Acta* **1972**, *267*, 160–171.

(48) Amdursky, N.; Marchak, D.; Sepunaru, L.; Pecht, I.; Sheves, M.; Cahen, D. Electronic Transport via Proteins. *Adv. Mater.* **2014**, 1–20.

(49) Yang, S.; Robinson, M. T.; Mwambutsa, F.; Cliffel, D. E.; Jennings, G. K. Effect of Cross-Linking on the Performance and Stability of Photocatalytic Photosystem I Films. *Electrochim. Acta* **2016**, *222*, 926–932.

(50) Carlberg, J. C.; Inganäs, O. Poly(3,4-Ethylenedioxythiophene) as Electrode Material in Electrochemical Capacitors. *J. Electrochem. Soc.* **1997**, *144*, L61–L64.

(51) Shimelis, A.; Elfwing, A.; Jager, E. W. H.; Bao, Q.; Inganas, O. A Renewable Biopolymer Cathode with Multivalent Metal Ions for Enhanced Charge Storage. *J. Mater. Chem. A* **2014**, *2*, 1974–1979.

(52) Bobacka, J.; Lewenstam, A.; Ivaska, A. Electrochemical Impedance Spectroscopy of Oxidized Poly (3, 4-Ethylenedioxythiophene) Film Electrodes in Aqueous Solutions. *J. Electroanal. Chem.* **2000**, *489*, 17–27.

(53) Bobacka, J. Potential Stability of All-Solid-State Ion-Selective Electrodes Using Conducting Polymers as Ion-to-Electron Transducers. *Anal. Chem.* **1999**, *71*, 4932–4937.

(54) Snook, G. A.; Peng, C.; Fray, D. J.; Chen, G. Z. Achieving High Electrode Specific Capacitance with Materials of Low Mass Specific Capacitance : Potentiostatically Grown Thick Micro-Nanoporous PEDOT Films. *Electrochem. commun.* **2007**, *9*, 83–88.

(55) Lota, K.; Khomenko, V.; Frackowiak, E. Capacitance Properties of Poly(3,4-Ethylenedioxythiophene)/carbon Nanotubes Composites. *J. Phys. Chem. Solids* **2004**, *65*, 295–301.

(56) Ciesielski, P. N.; Scott, A. M.; Faulkner, C. J.; Berron, B. J.; Cliffel, D. E.; Jennings, G. K. Functionalized Nanoporous Gold Leaf Electrode Films for the Immobilization of Photosystem I. *ACS Nano* **2008**, *2*, 2465–2472.

(57) Faulkner, C. J.; Lees, S.; Ciesielski, P. N.; Cliffel, D. E.; Jennings, G. K. Rapid Assembly of Photosystem I Monolayers on Gold Electrodes. *Langmuir* **2008**, *24*, 8409–8412.

(58) Bard, A. J.; Faulkner, L. R.; Swain, E.; Robey, C. *Electrochemical Methods*, Second.; John Wiley & Sons, Inc., 2001.

(59) Shiozawa, J. A.; Alberte, R. S.; Thornber, J. P. The P700-Chlorophyll a-Protein. *Arch. Biochem. Biophys.* **1974**, *165*, 388–397.

(60) Baba, K.; Itoh, S.; Hastings, G.; Hoshina, S. Photoinhibition of Photosystem I Electron Transfer Activity in Isolated Photosystem I Preparations with Different Chlorophyll Contents. *Photosynth. Res.* **1996**, *47*, 121–130.

(61) Website: www.terpconnect.umd.edu/~toh/spectrum/CurveFittingC.html.

CHAPTER 6

CONCLUSIONS AND OUTLOOK

Summary

In this thesis, a coherent theory for mediated electron transfer (MET) in biohybrid solar cells containing three-dimensional assemblies of PSI proteins is described on a first-principles basis (Chapter 3). Key insights from this analysis are employed to fabricate a hierarchical natural dye-sensitized solar cell composed of a multilayer film of PSI atop a mesoporous film of anthocyanin-coated TiO_2 (TiO_2:AC/PSI). Cells of this type produce more than double the photovoltage of unmodified controls (TiO_2:AC) and offer a new paradigm for biohybrid solar cells based on the mass-produced photocatalytic components of plants. Finally, a gentle method for incorporating intrinsically conductive polymers—including poly(3,4-ethylenedioxythiophene) (PEDOT) and polypyrrole (PPy)—into as-prepared PSI multilayer films is presented; the Friedel-Crafts catalyst, $FeCl_3$, is added to PSI solutions used in drop casting, allowing for vapor-phase polymerization of a wide library of ICPs within the assembled film. We utilize IR spectroscopy to demonstrate negligible degradation of the protein's secondary structure during preparation and polymerization steps. Additionally, photoelectrochemical analysis demonstrates that assembly method does not disrupt the photocatalytic activity of a PSI multilayer, but rather boosts it for thicker films relative to control PSI films. Additionally, we demonstrate that the PEDOT within PSI:vpPEDOT films permits

localized MET within the film to permit unidirectional photocurrent production from the composite films not possible for the control films.

Outlook

The work presented within this thesis elucidates the working principles of photocurrent production by PSI multilayer films in the presence of diffusible mediators. Specifically, the model formulated in Chapter 3 accurately simulates photocurrent production from a PSI multilayer when exposed to $[Fe(CN)_6]^{4-/3-}$ (R/O) for variable applied potential at the working electrode (**Figure 3.10**) and PSI multilayer thickness (**Figure 3.11**). This model is thus expected to provide insights into set points for maximum performance of such photoelectrochemical cells.

To demonstrate, three-dimensional optimization plots are shown here; the concentration of film-bound PSI and the thickness of the PSI film are independent variables and anodic photocurrent density is the dependent variable. In contrast to the work-up involved in the model in Chapter 3, the formulation constructed here reflects that PSI is the only absorbing species and thus solely dictates the amount of absorption decay as light progresses from the film's extent to the reflective electrode surface:

$$N_\lambda(x) = N_{\lambda,s}\left[10^{-\varepsilon C_{PSI}(H+x)} + 10^{-\varepsilon C_{PSI}(H-x)}\right] \quad (1)$$

where $N_{\lambda,s}$ is the photon flux from the light source (95 mW/cm^2), ε is the molar absorptivity of chlorophyll (64 000 M^{-1} cm^{-1}), x is the distance from the electrode surface, C_{PSI} is the concentration of PSI in the film, and H is the PSI film thickness. With the

concentration of absorbing species now equal to the concentration of PSI, one can approximate the effects of PSI density on absorbance decay within the packed film and its effect on generated photocurrent. Note that the concentration of *R* and *O* are both 0.1 mM and the kinetic and diffusional constants derived from the fitting routines of Chapter 3 are utilized.

With zero overpotential, the model predicts a maximum anodic photocurrent density of 1.5 μA/cm^2 for a 4 μm-thick film containing 20 mM of PSI (**Figure 6.1a**). The maximum anodic photocurrent density is more than double that of the maximum reached with the PSI films in our experimental study of photocurrent *vs.* PSI film thickness (**Figure 6.1b**). Thus, simulations indicate that a reduction in the number of absorbing species (i.e. knockdown of per PSI chlorophyll count) can result in significant gains in performance of such systems.

However, this maximum photocurrent is very small relative to the more than 10 mA/cm^2 produced by state-of-the-art solar cells—such as silicon p-n junction devices. Additionally, the prospect of reaching near-mA/cm^2 photocurrent densities is confronted by the fundamental limits of the Butler-Volmer equation for heterogeneous reactions that underpin current at the underlying electrode,[1]

$$j = Fk^0 C_O^{*(1-\alpha)} C_R^{*\alpha} \left[\frac{C_O(0,t)}{C_O^*} e^{-\alpha f \eta} - \frac{C_R(0,t)}{C_R^*} e^{(1-\alpha) f \eta} \right] \quad (2)$$

where *F* is the faraday constant (96,485 C/mol), k^0 is the standard rate constant (5 x 10^{-4} cm/s), C_O^* is the bulk concentration of oxidized species (0.1 mM), C_R^* is the bulk concentration of reduced species (0.1 mM), α is the transfer coefficient (0.5), η is the

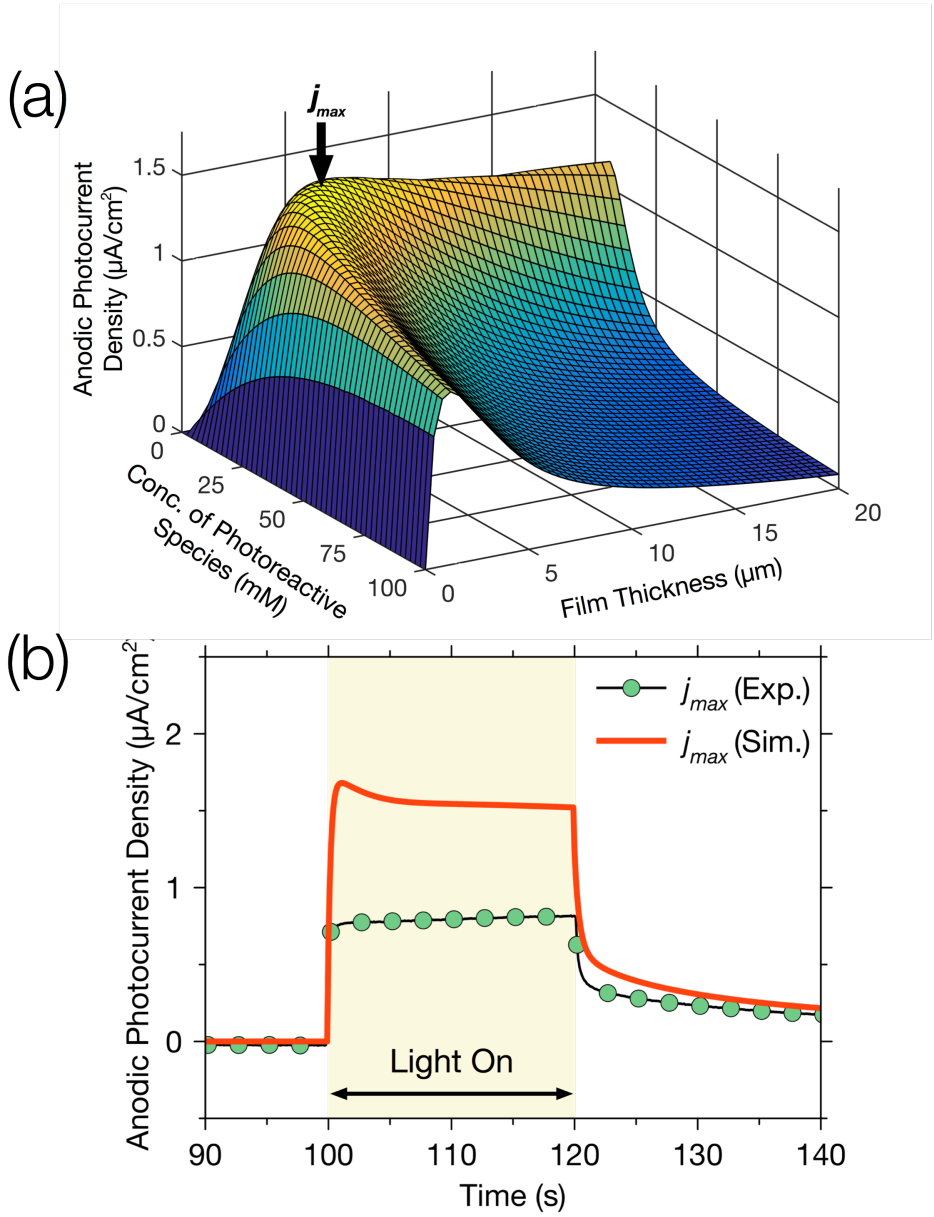

Figure 6.1. Simulation of PSI Multilayer Photocurrent as a Function of Film Thickness and Concentration of Photoreactive Species. (a) The model developed in Chapter 3 is used to provide an estimate for optimal photocurrents (1.5 μA/cm^2) for a 4.0 μm multilayer protein film containing 20 mM of a photoreactive species that acts as the sole absorber in the film. (b) The maximum photocurrent predicted from this exercise is more than double that of experimental thickness studies of PSI multilayer films. For the simulations provided, the kinetic constants used were the same as that derived from the fitting routine reported in Chapter 3 and the concentration of R and O was set to 0.1 mM and 0.1 mM, respectively.

overpotential supplied by the working electrode (0 mV), and f is nF/RT (1/25.693 mV^{-1}). $C_O(0,t)$ and $C_R(0,t)$ are the concentrations of oxidized and reduced mediator at the electrode surface, respectively, at time, t. Given that η = 0 mV and C_O^* and C_R^* are equal, eqn. 2 simplifies to,

$$j = Fk^0[C_O(0,t) - C_R(0,t)] \quad (3)$$

Eqn. 3 indicates that even if PSI were to completely convert all *O* to *R* within the film in this scenario, the bracketed term would equal [C_O^* + C_R^*] and j would reach its fundamental limit of just 9.6 μA/cm^2—more than three orders of magnitude lower than modestly performing conventional commercial solar cells.

As discussed in Chapter 3, applied overpotential can be used to augment photocurrent production by modifying the concentration of mediators within the PSI multilayer film to stimulate faster reaction rates between PSI and mediators. Indeed, under conditions of very large positive overpotential (+200 mV)—which stimulates heightened concentration of O within the PSI film—we predict a more than doubled maximum of 4 μA/cm^2 for a 3.7 μm PSI film containing 27 mM PSI (**Figure 6.2**). However, the effects of such efforts are also limited; in the case of +200 mV positive overpotential, eqn. 2 becomes:

$$j = Fk^0[0.02\ C_O(0,t) - 49\ C_R(0,t)] \quad (4)$$

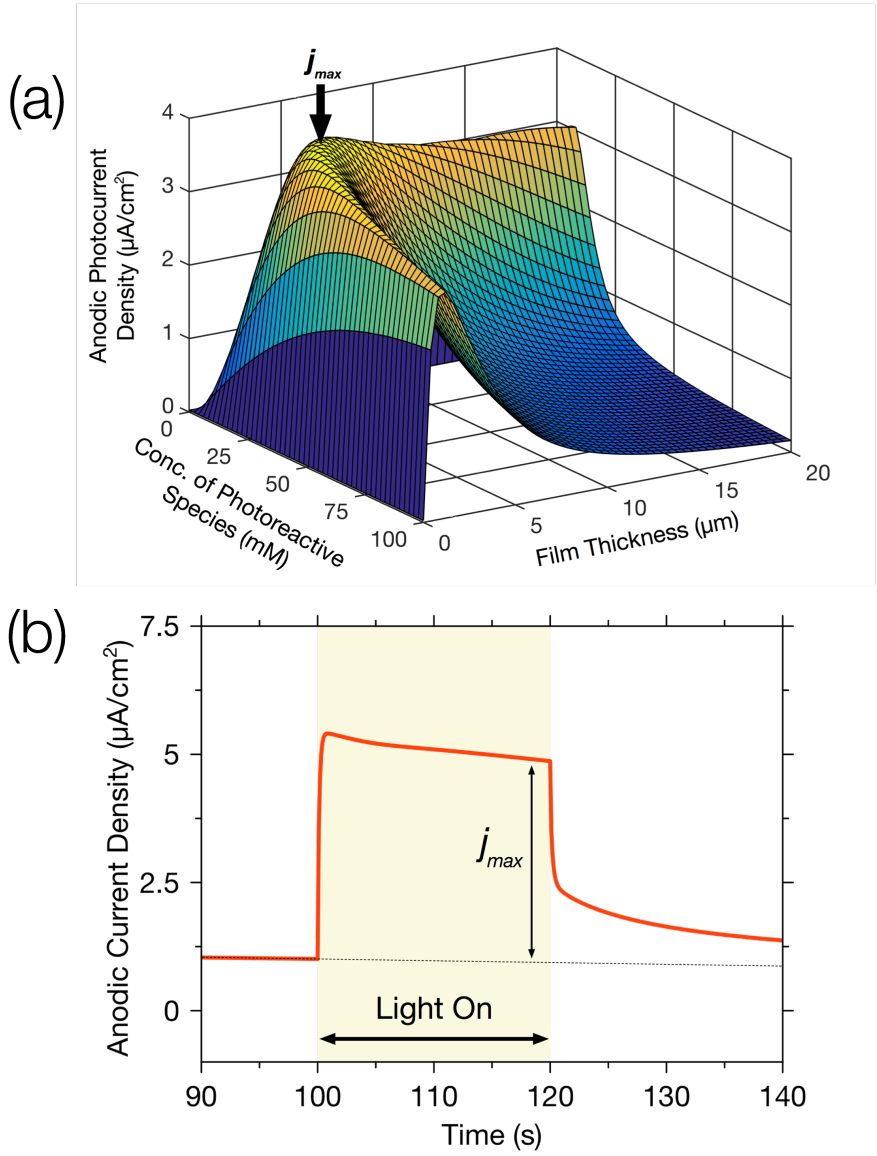

Figure 6.2. Simulation of PSI Multilayer Photocurrent as a Function of Film Thickness and Concentration of Photoreactive Species with Applied Bias. (a) Under applied bias, the model developed in Chapter 3 to provides an estimate for optimal photocurrents (3.9 μA/cm^2) for a 3.7 μm multilayer protein film containing 27 mM of a photoreactive species that acts as the sole absorber in the film. (b) The maximum photocurrent predicted from this exercise is more than double that under zero applied bias, but is still modest when compared to that produced by more conventional systems, such as silicon p-n junctions or dye-sensitized solar cells based on broadly absorbing synthetic dyes. For the simulations provided, the kinetic constants used were the same as that derived from the fitting routine reported in Chapter 3 and the concentration of R and O was set to 0.1 mM and 0.1 mM, respectively. At t = 0 s an overpotential of +200 mV was applied to the model cell and at t = 100 s light-driven reactions in the PSI film were simulated

Even in this extreme case, complete conversion of O to R within the film will produce just 470 μA/cm^2—an significant improvement relative to zero bias conditions but still more than an order of magnitude lower than that produced by commercial solar cells.

One could raise the concentration of O in the film, which would provide an increased upper limit to photocurrents (eqn. 3) and also speed-up the electron transfer reactions between PSI's high energy co-factors (P_{700}^* and F_B^-) and mediators in the electrolyte. However, due to the noted Michaelis-Menten asymptotic-type behavior, improvements based on this approach are similarly limited; in Chapter 3, with C_R^* held constant at 100 μM, an increase in C_O^* from 100 μM to 100 mM provided just a three-fold increase in photocurrent (**Figure 3.7**). This result indicates a reasonable expectation of maximum photocurrents of ~15 μA/cm^2 for photoelectrochemical cells incorporating large positive overpotential, chlorophyll knockdown, and optimized thickness. Thus, while the model suggests design approaches that will lead to significant improvement in photocurrent produced by PSI multilayer films, it also provides strong support for their limitations. However, as described in Chapter 4, efforts to apply PSI multilayer films in strategic supporting roles within a modular device design—such as a natural dye-sensitized solar cell—are useful in the push toward commercially viable biohybrid solar cells.

Efforts to construct photoelectrochemical systems incorporating dual MET by which two materials systems are employed to simultaneously transfer holes and electrons from photoexcited PSI are a route to push photoelectrochemical performance of PSI-based photoelectrochemical systems upward due to better separation of charge. Thus far, the best performing systems have encapsulated PSI proteins within a redox hydrogel that

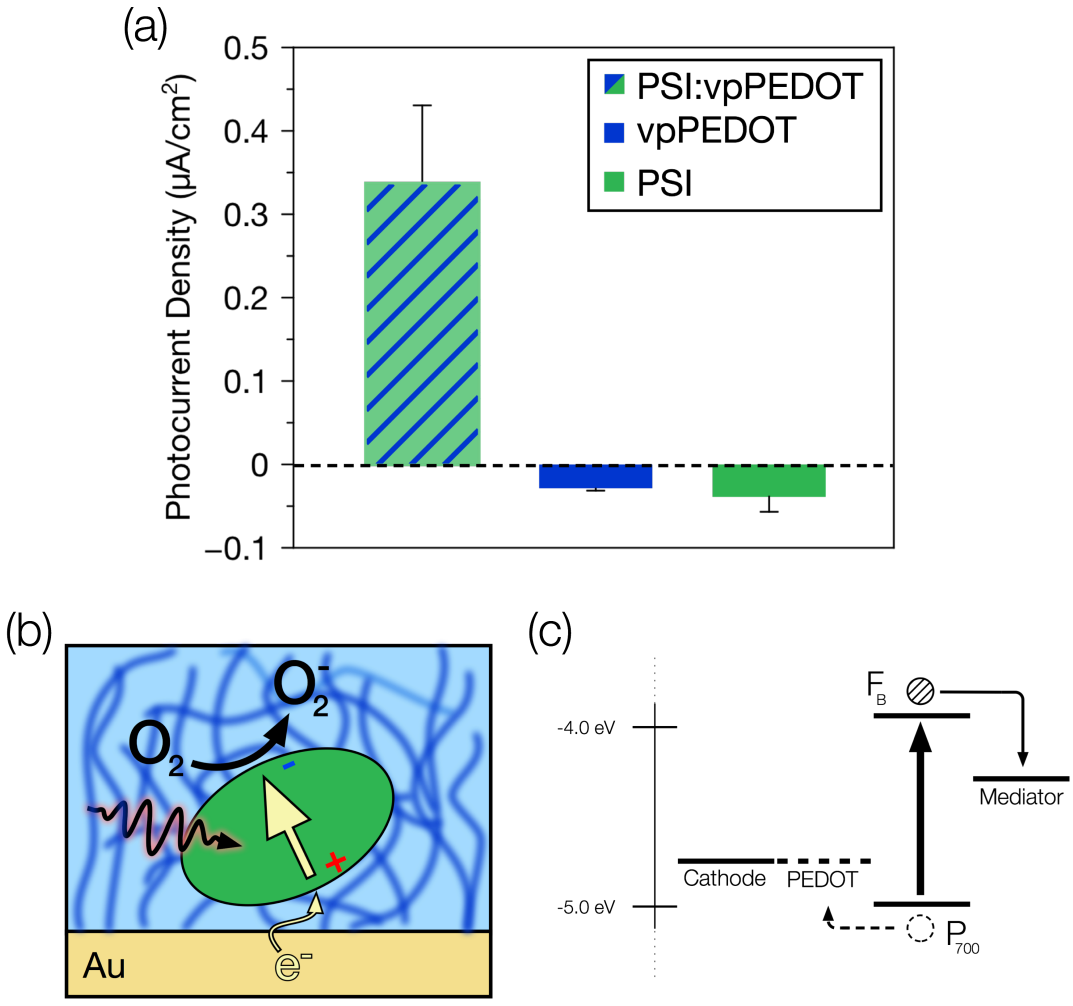

Figure 6.3. PSI:vpPEDOT in the Presence of Diffusible Mediators Promotes Unidirectional Cathodic Photocurrent *via* Dual MET. (a) PSI:vpPEDOT films on gold electrodes in the presence of an aqueous electrolyte containing solubilized O_2 demonstrate a near-order of magnitude improvement in photocurrent magnitude and a reverse in direction. (b) The reversed directionality of the improved photocurrent suggests that PEDOT incorporated within composite films enables a unique route of electron transfer during illumination—from the underlying electrode to the O_2. (c) An energy diagram displaying the pertinent energies of states involved in charge separation for PSI:vpPEDOT cells; photogenerated holes inject into PEDOT and shuttle to the Au cathode and photogenerated electrons inject into a generic water-soluble mediator—which could include high-energy acceptor species such as O_2 or methyl viologen.

permits hole transfer *via* redox moieties on the hydrogel scaffold and also electron transfer *via* high-energy diffusible mediators that demonstrate high partitioning into the hydrophilic polymer/PSI layer; such systems produce more than a 100 $\mu A/cm^2$ of photocurrent.[3] Progress in systems such as this continues, but the switch to more robust systems based on solid-state charge transfer are preferred due to their noted durability and lack of electrolyte evaporation concerns. In Chapter 5, composite films containing PSI and the intrinsically conductive polymer, PEDOT, prepared *via* vapor-phase polymerization are shown to provide a convenient materials system for hole extraction in dual MET photoelectrochemical cells (**Figure 6.3**). PEDOT and many other intrinsically conductive polymers have been used effectively within solid-state cells such as bulk heterojunction organic photovoltaics. Therefore, the coupling of PSI:vpICPs to a solid-state acceptor with reasonable electronic conductivity—such as [6,6]-Phenyl C_{61} butyric acid methyl ester (PCBM)—is a promising avenue toward highly resilient and efficient PSI-based solar cells.

Conclusions

This thesis has explored the mechanisms of and new materials systems for MET within PSI-based biohybrid solar cells. Herein, a persuasive mechanistic explanation for the photocatalytic effect of PSI multilayers is presented that describes experimental trends. MET between multilayer films of PSI proteins and diffusible mediators such as $[Fe(CN)_6]^{4-/3-}$ has been used toward a new and useful application within the larger field of biophotovoltaics, namely as a remarkably effective supporting engine within a natural dye-sensitized solar cell. Finally, a new materials system based on the combination of

PSI and PEDOT in a thick multilayer film via a gentle vapor-phase polymerization technique is developed and used to promote dual MET in photoelectrochemical cells. In general, future studies should focus on tuning the energetics and conductivity of mediation strategies to facilitate more efficient electron exchange with PSI co-factors and more rapid shuttling of charge carriers within the photocell, respectively.

Works Cited

(1) Bard, A. J.; Faulkner, L. R.; Swain, E.; Robey, C. *Electrochemical Methods*, Second.; John Wiley & Sons, Inc., 2001.

(2) Robinson, M. T.; Simons, C. E.; Cliffel, D. E.; Jennings, G. K. Photocatalytic Photosystem I/PEDOT Composite Films Prepared by Vapor-Phase Polymerization. *Nanoscale* **2017**, *9*, 6158–6166.

(3) Badura, A.; Guschin, D.; Kothe, T.; Kopczak, M. J.; Schuhmann, W.; Rogner, M. Photocurrent Generation by Photosystem 1 Integrated in Crosslinked Redox Hydrogels. *Energy Environ. Sci.* **2011**, *4*, 2435–2440.

APPENDIX A

MATLAB CODE USED FOR REACTION-DIFFUSION MODEL IN CHAPTER 3

The overall program requires the use of a script file (Diffusion.m) along with three function files—DiffusionICfun.m, DiffusionBCfun.m, DiffusionPDEfun.m, —that supply initial conditions, supply boundary conditions, and compute the solutions to the PDEs, respectively. To run the program, simply copy and paste what is provided below into separate MATLAB m files within the same folder. The program should output a simulated photochronoamperometric experiment (**Figure A.1**) corresponding to the fitted model of Chapter 3 (**Figure 3.8**).

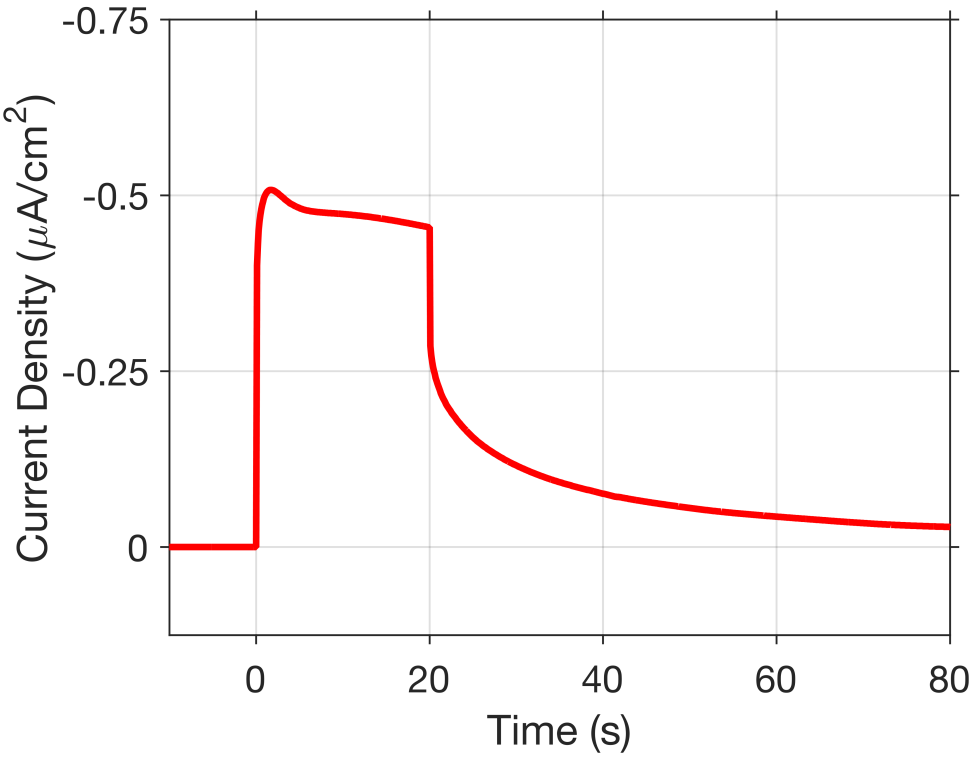

Figure A.1. Simulated Photochronoamperometric Experiment Based on Provided MATLAB Script and Function Files. *H*, C_R^*, C_O^*, θ, and η were 0.65 μm, 0.1 mM, 0.1 mM, 1, and 0 mV, respectively, for this simulation. Illumination is between 0 s and 20 s after which illumination ceases.

Script: *Diffusion.m*

```
clear
close all
%Transport Parameters
P(1)=7.6E-6; %D_R, Diffusion coefficient of reduced mediator, [cm^2/s]
P(2)=1.0E-2; %phi_R, Void fraction of PSI film for reduced mediator, [-]
P(3)=6.5E-6; %D_O, Diffusion coefficient of oxidized mediator, [cm^2/s]
P(4)=6.2E-3; %phi_O, Void fraction of PSI film for oxidized mediator, [-]

%Concentrations
P(5)=.1; %C_Rs, Initial concentration of reduced mediator, [umol/cm^3]
P(6)=.1; %C_Os, Initial concentration of oxidized mediator, [umol/cm^3]
P(7)=17.6; % C_PSI, Concentration of PSI in multilayer film, [umol/cm^3]
P(8)=83.7; % C_chl, Concentration of chl in PSI multilayer film, [umol/cm^3]

%Physical Parameters
P(9)=3000E-4; % Height of solution, [cm]
P(10)=0.65E-4; % H, Thickness of PSI film, [cm]

% Electrochemical Parameters
P(11)=5E-4; %k^0, Standard rate constant, [cm/s]
P(12)=.5; %alpha, Transfer coefficient, [-]
P(13)=0; %eta, Overpotential, [mV]

% Kinetic Constants
P(14)=2.57413E-4; % k_ox, [cm^3/umol/s]
P(15)=1.16148E6; % k_gen, [cm^2/umol]
P(16)=967.096; % k_rec, [1/s]
P(17)=271.097; % k_ETC, [cm^3/umol/s]
P(18)=8.37294E-3; % k_rec2, [cm^3/umol/s]
P(19)=1.42584E-2; % k_red, [cm^3/umol/s]
P(20)=1.27887E3; % k_red2, [cm^3/umol/s]
P(21)=1; %theta, constant for scattering/re-emission within PSI film, [-]

%Optical Parameters
P(22)=95; %Pwr, Lamp power, [mW/cm^2]
P(23)=680; %lambda, wavelength of source illumination, [nm]
P(24)=64; %Molar absorptivity of chlorophyll, [cm^2/mol]

% Parameter corresponding to the symmetry of the problem
% www.mathworks.com/help/matlab/ref/pdepe.html
m=0;

%Spatial Discretization
x1=linspace(0,P(10),200); % Points within PSI Film, [cm]
x2=linspace(P(10)+1E-14*P(10),P(9),200); % Points within bulk solution, [cm]
```

```
x=cat(2,x1,x2); % Concatenated system array, [cm]

%Time points for function evaluation
t=linspace(0,200,2001); % [s]

%Call of numerical pde solver
sol=pdepe(m,@DiffusionPDEfun,@DiffusionICfun,@DiffusionBCfun,x,t,[],P);

%Spatial- and time-dependent solutions to PDEs
C_R=sol(:,:,1); %C_R(x,t), concentration of reduced mediator, [umol/cm^3]
C_O=sol(:,:,2); %C_O(x,t), concentration of reduced mediator, [umol/cm^3]
C_Dp=sol(:,:,3); %C_Dp(x,t), concentration of depleted D (D^+), [umol/cm^3]
C_Ds=sol(:,:,4); %C_Ds(x,t), concentration of excited D (D^*), [umol/cm^3]
C_Am=sol(:,:,5); %C_Am(x,t), concentration of reduced A (A^-), [umol/cm^3]

% Constants for use within Butler-Volmer equation
C_Rs=P(5); %Initial concentration of reduced mediator, [umol/cm^3]
C_Os=P(6); %Initial concentration of oxidized mediator, [umol/cm^3]
k0=P(11); %Standard rate constant, [cm/s]
alpha=P(12); %Transfer coefficient, [-]
eta=P(13); %Overpotential, [mV]
F=96485; % Faraday constant, [C/mol]
j0=F*k0*C_Os^(1-alpha)*C_Rs.^alpha;  % Exchange current density [uA/cm^2]

% Butler-Volmer equation for current density, j [uA/cm^2]
j=j0.*(C_O(:,1)./C_Os.*exp(-alpha.*eta./25.693)-C_R(:,1)./C_Rs.*exp((1-
alpha).*eta./25.693));

%Plots
plot(t-100,j,'Color',[1,0,0],'LineWidth',2.5)
grid on
axis([-10 80 -0.75 0.125])
ax = gca;
ax.YTick = [-.75 -.5 -.25 0];
ax.XTick = [0 20 40 60 80];
ylabel('Current Density (\muA/cm^2)')
xlabel('Time (s)')
set(ax,'Fontsize',16)
set(ax,'Fontname','Helvetica Neue')
set(gca,'Ydir','reverse')
set(gca,'TickDir','out')
```

Function: ***DiffusionICfun.m***

```
function [u0] = DiffusionICfun(x,P)

% Parameter Extraction
C_Rs=P(5); % Initial concentration of reduced mediator, [umol/cm^3]
C_Os=P(6); % Initial concentration of oxidized mediator, [umol/cm^3]
H=P(10); % Thickness of PSI film, [cm]

% Initial conditions for t=0, can be a function of x
if x>=0 && x<=H
u0=[C_Rs;C_Os;0;0;0];
elseif x>H
u0=[C_Rs;C_Os;0;0;0];
end
```

Function: *DiffusionBCfun*

```
function [pl,ql,pr,qr] = DiffusionBCfun(xl,ul,xr,ur,t,P)
% Boundary conditions for x = 0 and x = L

C_Rs=P(5); % Initial concentration of reduced mediator, [umol/cm^3]
C_Os=P(6); % Initial concentration of oxidized mediator, [umol/cm^3]
k0=P(11); % Standard rate constant, [cm/s]
alpha=P(12); % Transfer coefficient, [-]
eta=P(13); % Overpotential, [mV]
f=1/25.693; % nF/RT, [1/mV] **assuming n=1**

% Boundary conditions: p+qf=0 %

% p, right side
pr=[0;0;0;0;0];

% q, right side
qr=[1;1;1;1;1];

% p, left side
pl=-k0.*C_Os.^(1-alpha).*C_Rs.^alpha.*[ul(1)/C_Rs.*exp((1-alpha).*f.*eta)-
ul(2)./C_Os.*exp(-alpha.*f.*eta);-ul(1)./C_Rs.*exp((1-
alpha).*f.*eta)+ul(2)./C_Os.*exp(-alpha.*f.*eta);0;0;0];

% q, left side
ql=[1;1;1;1;1];

end
```

Function: *DiffusionPDEfun.m*

```
function [ c,f,s ] = DiffusionPDEfun(x,t,u,dudx,P)

% Extracted Parameters
D_R=P(1); % Diffusion coefficient of reduced mediator, [cm^2/s]
phi_R=P(2); % Void fraction of PSI film for reduced mediator, [-]
D_O=P(3); % Diffusion coefficient of oxidized mediator, [cm^2/s]
phi_O=P(4); % Void fraction of PSI film for oxidized mediator, [-]
C_PSI=P(7); % Concentration of PSI in multilayer film, [umol/cm^3]
C_chl=P(8); % Concentration of chl in PSI multilayer film, [umol/cm^3]
H=P(10); % Thickness of PSI film, [cm]
k_ox=P(14); % [cm^3/umol/s]
k_gen=P(15); % [cm^2/umol]
k_rec=P(16); % [1/s]
k_ETC=P(17); % [cm^3/umol/s]
k_rec2=P(18); % [cm^3/umol/s]
k_red=P(19); % [cm^3/umol/s]
k_red2=P(20); % [cm^3/umol/s]
theta=P(21); % [-]
Pwr=P(22); % Lamp power, [mW/cm^2]
lambda=P(23); % Wavelength of source illumination, [nm]
eps=P(24); % Molar absorptivity of chlorophyll, [cm^2/mol]

% Constants
h_b=1.0546E-34; % Reduced Planck Constant, [J*s]
c_l=3E8*100; % Speed of Light, [cm/s]
N_A=6.022E23; % Avogadro's number, [1/mol]


% PDE specification, c*dudt=d/dx(f)+s
c=[1;1;1;1;1];

% if statement for diffusion coefficients within film and bulk electrolyte
if x>=0 && x<H
f=[phi_R*D_R;phi_O*D_O;0;0;0].*dudx;
elseif x>=H
f=[D_R;D_O;0;0;0].*dudx;
end

 % Concentration Specification
C_R=u(1);
C_O=u(2);
C_Dp=u(3);
C_Ds=u(4);
C_Am=u(5);

 % if-then statement for intra-film reactions before, during, and after illumination
```

```
if x>=0 && x<H
   if t<100
      % Initial rates of formation (C_R, C_O, C_Dp, C_Ds, C_Am)
      dCRdt_init=0; % [umol/cm^3]
      dCOdt_init=0; % [umol/cm^3]
      dCDpdt_init=0; % [umol/cm^3]
      dCDsdt_init=0; % [umol/cm^3]
      dCAmdt_init=0; % [umol/cm^3]

      s=[dCRdt_init;dCOdt_init;dCDpdt_init;dCDsdt_init;dCAmdt_init];

   elseif t>=100 && t<=120

      % Conservation statements for C_A, C_D
      C_A=C_PSI-C_Am; % [umol/cm^3]
      C_D=C_PSI-C_Dp-C_Ds; % [umol/cm^3]

      % 1-D Absorption Model

      % Source photon flux [mol/cm^2/s]
      Nls=Pwr*lambda/h_b/c_l/N_A/1000/(2*pi)*1E-7;
      % Spatially-dependent photon flux in film [mol/cm^2/s]
      Nl=Nls*(10.^-(eps.*C_chl.*(H-x))+10.^-(eps.*C_chl.*(H+x)));

      % Rates of formation during illumination [umol/cm^3/s]
      dCRdt_on=-k_ox*C_Dp*C_R+k_red*C_Am*C_O+k_red2*C_Ds*C_O;
      dCOdt_on=-dCRdt_on;
      dCDpdt_on=-k_ox*C_Dp*C_R+k_ETC*C_Ds*C_A-
k_rec2*C_Am*C_Dp+k_red2*C_Ds*C_O;
      dCDsdt_on=theta*k_gen*Nl*C_D-k_rec*C_Ds-k_ETC*C_Ds*C_A-
k_red2*C_Ds*C_O;
      dCAmdt_on=k_ETC*C_Ds*C_A-k_rec2*C_Am*C_Dp-k_red*C_Am*C_O;

      s=[dCRdt_on;dCOdt_on;dCDpdt_on;dCDsdt_on;dCAmdt_on];

   elseif t>120

      % Conservation statements for C_A, C_D
      C_A=C_PSI-C_Am; % [umol/cm^3]
      C_D=C_PSI-C_Ds-C_Dp; % [umol/cm^3]

      % Photon flux calculation
      Nl=0; [mol/cm^2/s]

      % Rates of formation post-illumination [umol/cm^3/s]
      dCRdt_off=-k_ox*C_Dp*C_R+k_red*C_Am*C_O+k_red2*C_Ds*C_O;
```

```
        dCOdt_off=-dCRdt_off;
        dCDpdt_off=-k_ox*C_Dp*C_R+k_ETC*C_Ds*C_A-
k_rec2*C_Am*C_Dp+k_red2*C_Ds*C_O;
        dCDsdt_off=theta*k_gen*Nl*C_D-k_rec*C_Ds-k_ETC*C_Ds*C_A-
k_red2*C_Ds*C_O;
        dCAmdt_off=k_ETC*C_Ds*C_A-k_rec2*C_Am*C_Dp-k_red*C_Am*C_O;

        s=[dCRdt_off;dCOdt_off;dCDpdt_off;dCDsdt_off;dCAmdt_off];

    end

elseif x>=H

   s=[0;0;0;0;0];
end
```

APPENDIX B

SURFACE-INITIATED RING-OPENING METATHESIS POLYMERIZATION FROM FILMS OF PSI PROTEINS

Introduction

The organic photovoltaic (OPV) framework for 3rd generation solar cells demonstrates competitive efficiency and promising materials costs. The operating principle is based on exciton generation and separation at materials interfaces of divergent electron affinity. Typically, a good hole-transfer species that also generates excitons under illumination—such as P3HT—is coupled to proximal phase(s) of an electron acceptor species—such as PCBM. However, the materials used in OPVs are often expensive to make and have considerable stability issues. Thus, the use of abundant and highly stable natural species within such systems is a potential avenue for more economical OPV technologies.

With this in mind, we developed a method to graft polymers from PSI proteins using surface-initiated ring-opening metathesis polymerization (SI-ROMP) in the effort to develop an OPV system based around PSI being the principal photoactive element. SI-ROMP is a well-studied polymerization technique that is catalyzed by the release of ring strain from a monomer groups (in this case a norbornene moiety). SI-ROMP has been applied to grafting from procedures from various surfaces and films. In this section, efforts to grow thick films of a test polymer—poly(5-(perfluorohexyl)norbornene) (pNBF6)—are documented. After demonstrating success with pNBF6, we attempted to

grow polyacetylene—an intrinsically conductive polymer (ICP)—*via* SI-ROMP of cyclooctatraene from PSI monolayers.

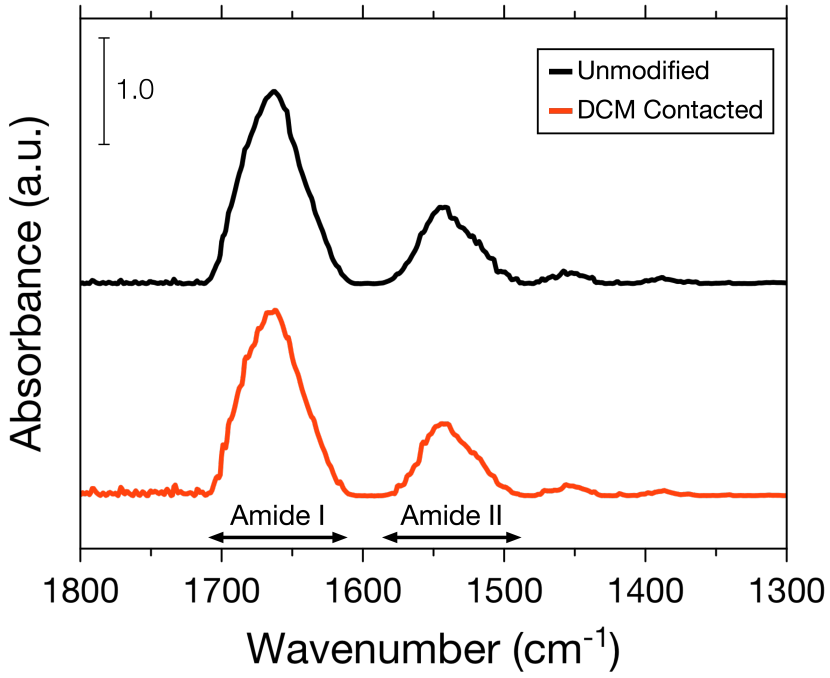

Sample	β-turn	β-sheet	α-helix	Unordered helix
Unmodified	19.5 ± 2.2 %	38.1 ± 4.0 %	33.4 ± 2.2 %	9.0 ± 2.1 %
DCM Contacted	21.2 ± 1.7 %	34.2 ± 0.4 %	35.7 ± 1.9 %	9.0 ± 1.9 %

Figure B.1. PM-IRRAS of Unmodified and DCM-Exposed PSI Monolayers on Au/AET Electrodes. Top: Representative PM-IRRAS spectra of an unmodified PSI monolayer film (green) and a PSI monolayer film that was exposed to DCM for 30 minutes, paralleling that time of exposure during the SI-ROMP procedure. Bottom: Amide I spectra were deconvolved into contributions from different secondary folding structures—including β-turn, β-sheet, unordered helix, and α-helix. Based on this analysis, we conclude that 30 minute exposure to DCM does not significantly modify the secondary structure of PSI adsorbed to Au/AET.

Results and Discussion

Before an SI-ROMP protocol was established, it was necessary to test PSI's stability within the solvent used in SI-ROMP, dichloromethane (DCM). To do this, we placed gold substrates with adsorbed PSI monolayers into DCM for 30 min corresponding to the amount of time that the films would be in DCM for the duration of the planned polymerization procedure. After 30 min, both secondary structure (**Figure B.1**) and photocurrent generation (**Figure B.2**) of PSI adsorbed onto gold substrates are not significantly modified.

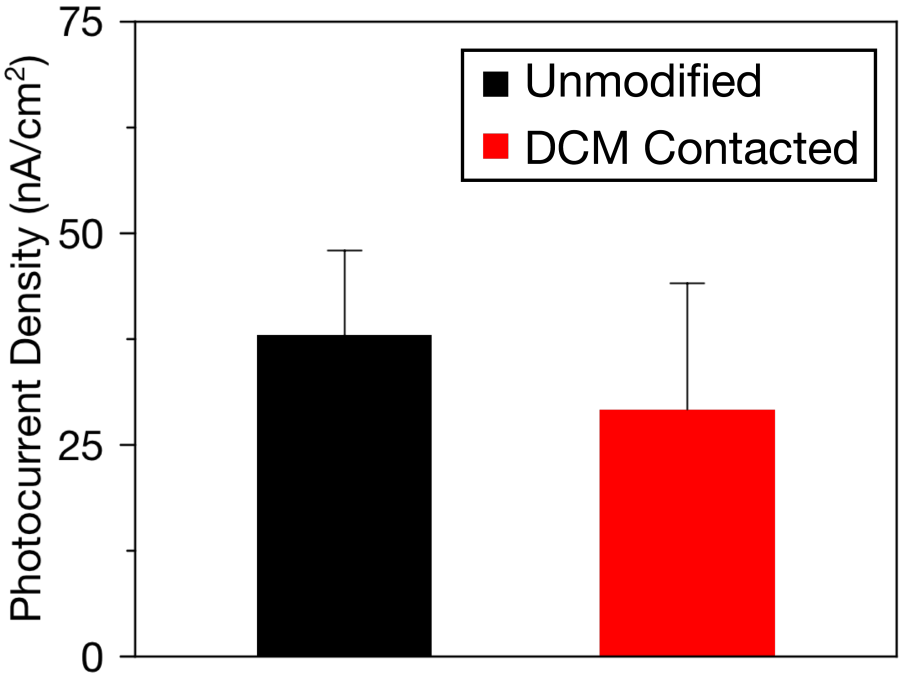

Figure B.2. Photocurrent Generated by Unmodified and DCM-Contacted PSI Monolayers on Gold Electrodes. After 30 min of exposure to DCM, PSI monolayers adsorbed on gold electrodes produce ~80% of the photocurrent of unmodified monolayers. The aqueous electrolyte used in photocurrent measurements included 5 mM sodium ascorbate, 250 μM DCPIP, and 100 mM KCl. Cells were illuminated with a white light source (142 mW/cm^2).

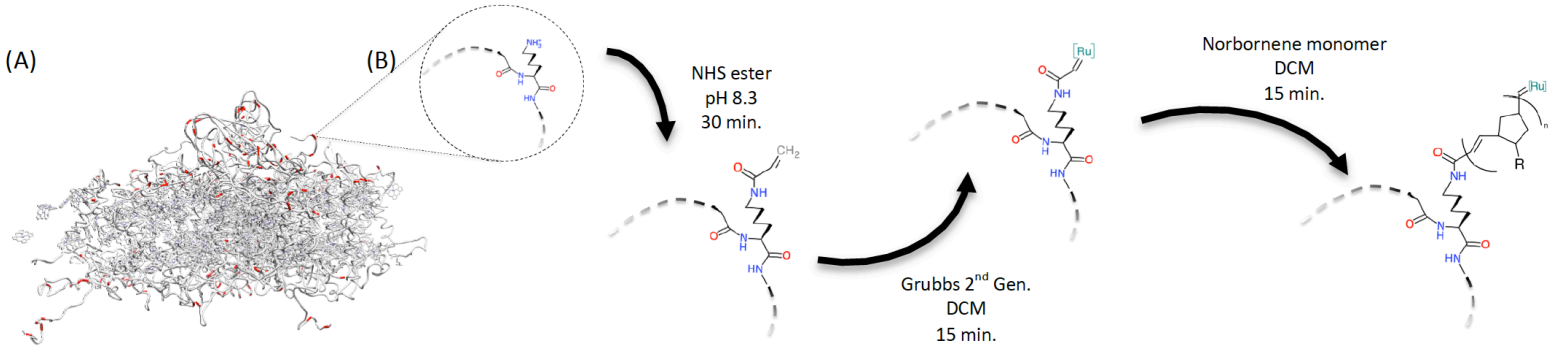

Figure B.3. Primary Amine-Initiated SI-ROMP from PSI Proteins. (A) 3-D model of PSI where red regions denote the 136 lysine residues on stromal and luminal sides of the protein. (B) General vinyl attachment and polymerization procedure.

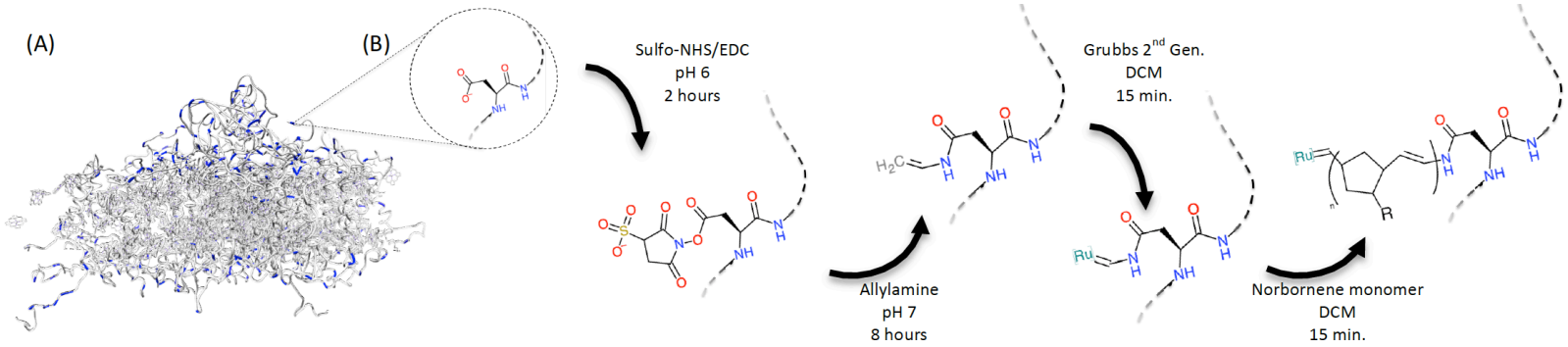

Figure B.4. Carboxylic Acid-Initiated SI-ROMP from PSI Proteins. (A) 3-D model of PSI where blue regions denote the 250 aspartic and glutamic acid residues on stromal and luminal sides of the protein. (B) General vinyl attachment and polymerization procedure.

Two separate approaches were applied in order to graft from either carboxylic acid and primary amine moieties present on the stromal and luminal sides of PSI proteins. In order to attach to carboxylic acids, we first exposed PSI monolayers on gold to EDC/sulfo-NHS and then reacted this with allylamine to get a vinyl group expressed at the site of initiation (**Figure B.3**). In order to attach to primary amines, we exposed PSI monolayers on gold to NHS ester (**Figure B.4**). While PM-IRRAS indicates that grafting was initiated (**Figure B.5a**), such growth was limited to just a few nm (**Figure B.5b**). In order to boost the initiation of pNBF6, we utilized NBDAC to get a norbornene species at the site of initiation through reaction of NBDAC's acyl chlorides with primary amines on PSI (**Figure B.6a**); NBDAC's reaction with PSI did not significantly lower the magnitude of photocurrent produced in photoelectrochemical systems, but did slow the photocurrent rise time—ostensibly due to bound NBDAC obstructing sites for charge transfer reactions between PSI's terminal co-factors and solution phase mediators (**Figure B.6b**). By soaking the monolayer films in 20 mM NBDAC, we were able to get nearly 20 nm of growth of pNBF6; however, a rinse of PSI films in 20 mM NBDAC permitted growth of ~170 nm of pNBF6 (**Figure B.7**).

With the success of this NBDAC approach, we attempted to grow polyacetylene from PSI residues in a similar fashion by polymerizing cyclooctatraene from PSI monolayers on gold (**Figure B.8**). This effort was ultimately unsuccessful, but we were able to grow polyacetylene in the vapor phase above the deposited PSI monolayer. It is possible that a grafting-from approach targeted to a PSI multilayer (rather than monolayer) on a gold substrate could work much better given the significantly higher sites for initiation.

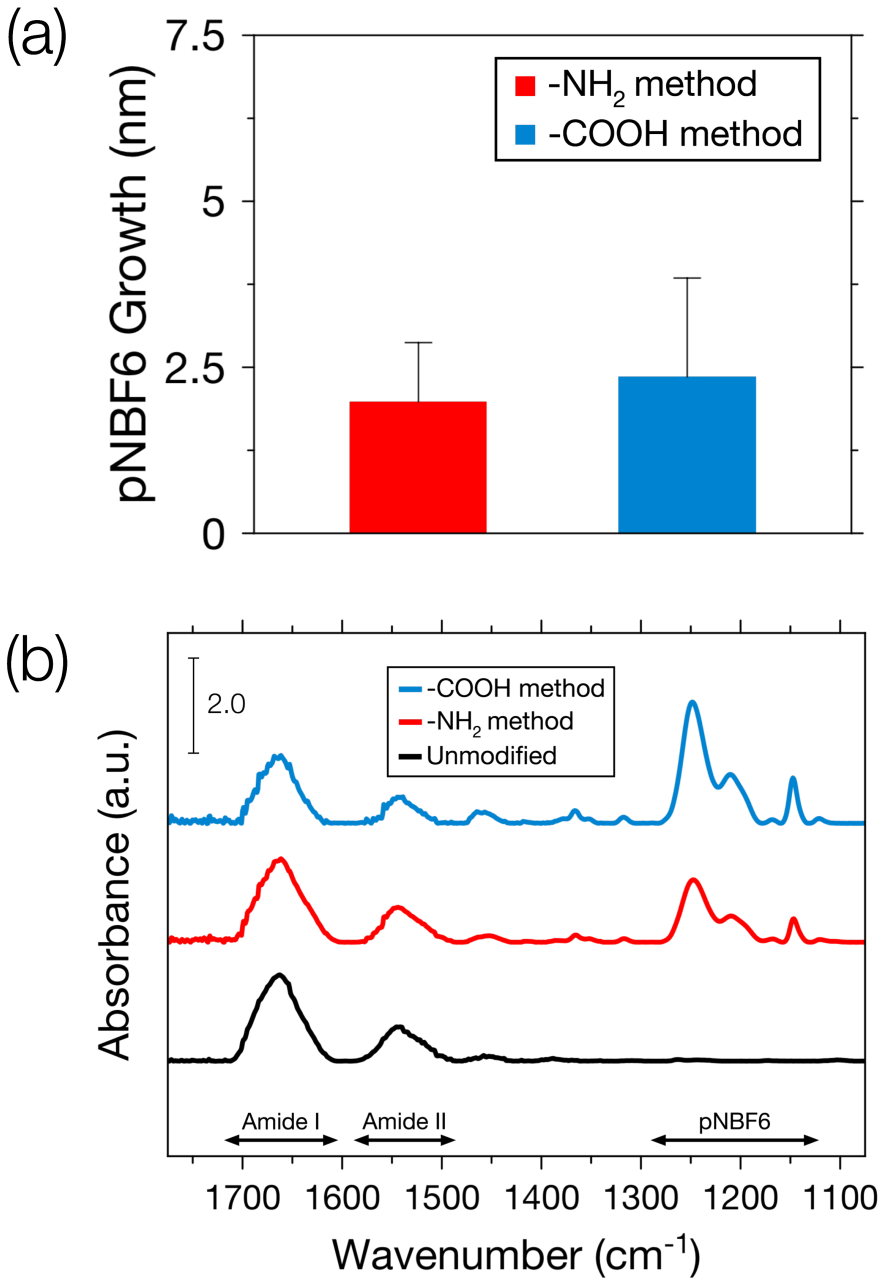

Figure B.5. Thickness and PM-IRRAS Characterization of SI-ROMP of pNBF6 from PSI Using Carboxylic Acids or Primary Amines as Initiation Sites. (a) Ellipsometry indicates that both the NHS ester and EDC/NHS/allylamine methods of initiating polymer growth from primary amine and carboxylic acid residues of PSI provided for poor growth of pNBF6. (b) Despite the limited growth of pNBF6, PM-IRRAS spectra indicate that pNBF6 grafting from PSI was achieved for both methods employed.

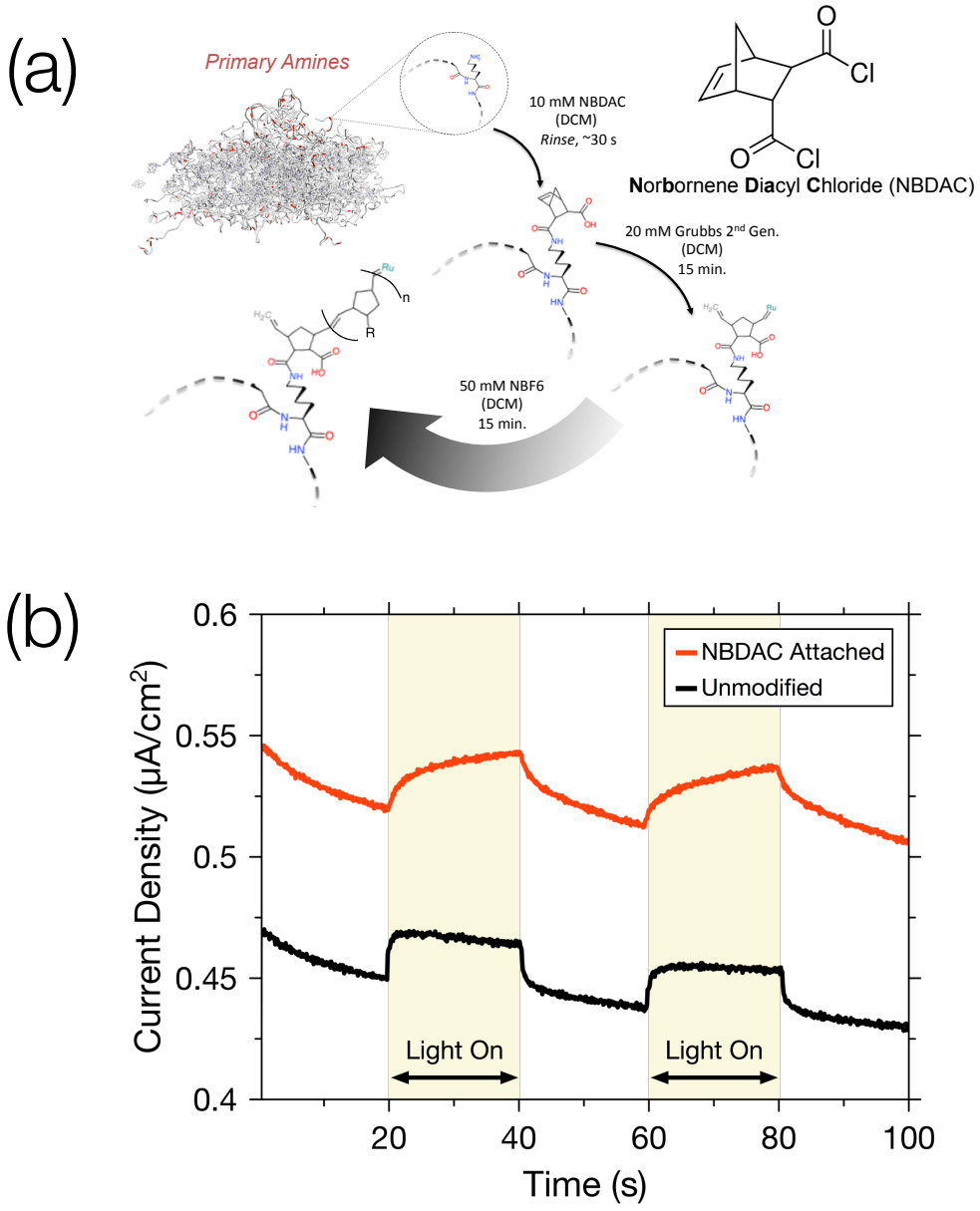

Figure B.6. NBDAC as Initiator for pNBF6 Grafting from PSI's Lysine Residues. (a) General procedure for grafting. (b) PCA of NBDAC-modified PSI monolayers demonstrates limited changes in the photocurrent magnitudes, but slower rise times possibly due to the attached NBDAC species blocking charge transfer routes between PSI co-factors and solution-phase mediators. PCA measurements were collected in an aqueous electrolyte containing 5 mM sodium ascorbate and 250 μM DCPIP. The working electrode was set at -0.1 V vs. Ag/AgCl for both tests shown.

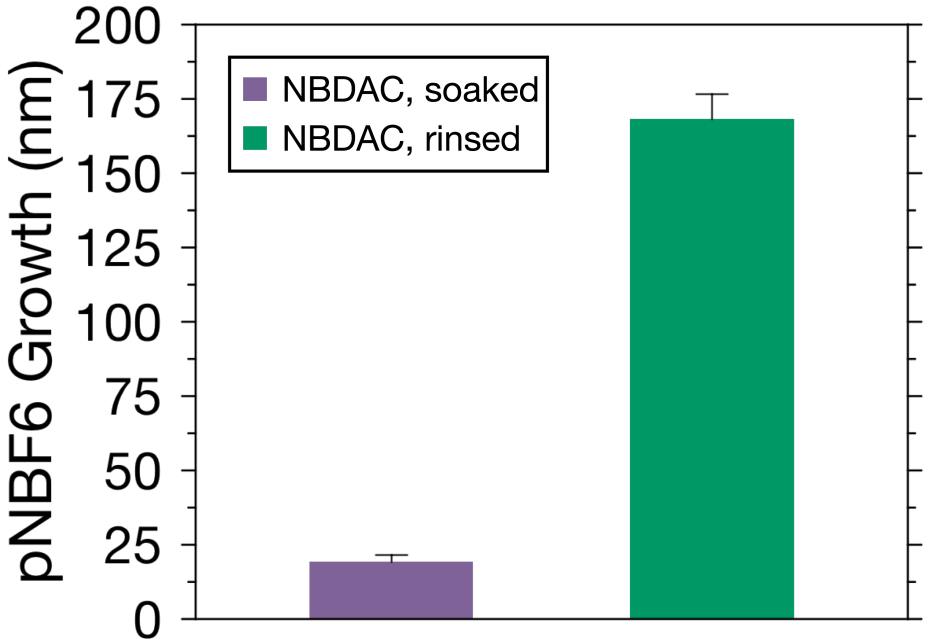

Figure B.7. Thickness of pNBF6 Grown from PSI Monolayers on Gold Substrates Using NBDAC Initiation Method. Rinsing PSI films in 20 mM NBDAC solution in DCM provided for nearly 9x more pNBF6 growth relative to soaking the films in the same solution for 50 minutes.

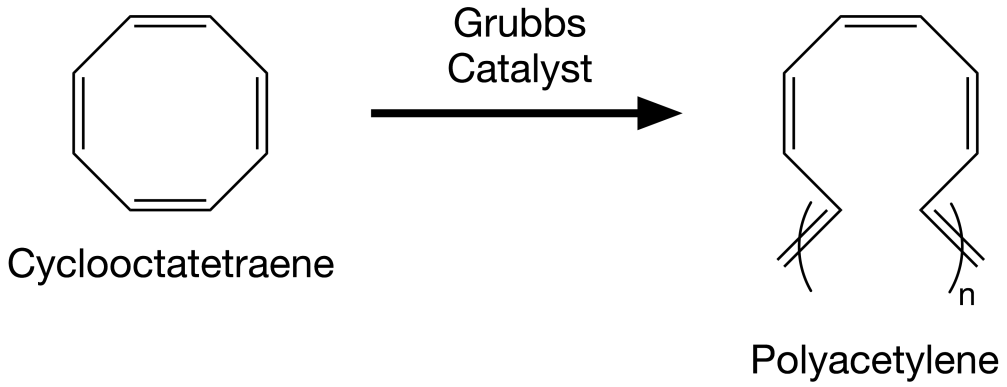

Figure B.8. Cyclooctatraene as ROMP-able Monomer to Grow Polyacetylene from PSI Protein Films. Cyclooctatraene has sufficient ring strain to be opened by Grubbs catalyst to form strands of polyacetylene, an intrinsically conductive polymer.

Experimental Methods

Extraction and isolation of PSI proteins

Photosystem I proteins were extracted from spinach leaves as described previously.[1] Briefly, baby spinach leaves were ground and macerated. The resulting solution was centrifuged at 8 000 g to isolate thylakoid membranes. Re-suspension of the resulting pellet in an aqueous solution containing 1% w/v Triton X-100 opened the thylakoids, releasing unbound PSI proteins into solution. A second round of centrifugation at 20 000 g was used to separate out higher molecular weight proteins/fragments from the PSI solution. Chilled hydroxylapatite column chromatography of the supernatant provided the final aqueous PSI solution. Using the methods of Baba et. al. [2], [P_{700}] was determined to be 0.5 μM.

PSI monolayer film preparation

PSI monolayer preparation followed previously described methods.[3] Briefly, 1.5 cm by 5 cm gold substrates were cleaned using ethanol and water and dried using a stream of nitrogen. 50 μL PSI solution was applied to the surface of the gold substrates and vacuum was applied to evaporate water and leave behind a PSI film. The samples were rinsed vigorously with DI water to rinse away all but the first layer of protein and then dried in a stream of nitrogen. This process provided protein monolayers with ~8 nm average ellipsometric thickness.

Aqueous pNBF6 'grafting-from' primary amines

PSI monolayers on gold electrodes were exposed to an aqueous solution containing 20 mM acrylic acid N-hydroxysuccinimide ester and 80 mM HEPES buffer (pH 8.3). After 30 min the samples were washed in 80 mM HEPES buffer solution (pH 8.3) and placed in a 20 mM Grubbs second-generation catalyst solution in DCM for fifteen minutes. Samples were then removed and washed in DCM for 30 s. Next, samples were placed in a vial containing 25 mM NBF6 in DCM to prompt polymerization. After 15 min, the samples were removed, washed with DCM, and allowed to air dry.

Aqueous pNBF6 'grafting-from' carboxylic acids

PSI monolayers on gold electrodes were exposed to an aqueous solution containing 10 mM sulfo-N-hydroxysuccinimide ester, 10 mM 1-Ethyl-3-(3-dimethylaminopropyl)carbodiimide, and MES buffer (pH 6.0). After 30 min the samples were washed in MES buffer solution (pH 6.0) and placed in a 20 mM Grubbs second-generation catalyst solution in DCM for fifteen minutes. Samples were then removed and washed in DCM for 30 s. Next, samples were placed in a vial containing 25 mM NBF6 in DCM to prompt polymerization. After 15 min, the samples were removed, washed with DCM, and allowed to air dry.

NBDAC 'Grafting-from' procedure

NBDAC was attached to PSI monolayers in one of two ways. For the 'rinsed' protocol, 10 mM NBDAC solution in dichloromethane (DCM) was rinsed over the surface of each monolayer sample for ~30 seconds using a long-stem pipette. For the

'soaked' protocol, the monolayer sample was placed in 10 mM NBDAC solution for 50 min. Regardless of the NBDAC attachment method the samples were subsequently rinsed in DCM for 30 s. Once the DCM had evaporated, the samples were placed in a 20 mM Grubbs second-generation catalyst solution in DCM for fifteen minutes. Samples were immediately washed vigorously in a stream of DCM for 30 s and placed in a 25 mM NBF6 reaction vial to prompt polymerization. After 15 min, the samples were removed, washed with DCM, and allowed to air dry.

Ellipsometry: All ellipsometric measurements were taken with a variable angle spectroscopic ellipsometer (J. A. Woollam M-2000DI). Thicknesses were fit to data measured for wavelengths spanning 400 nm to 700 nm at two angles from the surface normal—70° and 80°—using a refractive index of 1.45.

Photocurrent measurements

PCA was conducted using a CH Instruments CHI 660a potentiostat. A three-electrode setup was used including a Ag/AgCl reference electrode, platinum mesh counter electrode, and a PSI monolayer-decorated gold electrode that served as working electrode. Lamp light intensity was 140 mW/cm^2. All photocurrent statistics were taken after 17 s of illumination.

Works Cited

(1) Ciesielski, P. N.; Faulkner, C. J.; Irwin, M. T.; Gregory, J. M.; Tolk, N. H.; Cliffel, D. E.; Jennings, G. K. Enhanced Photocurrent Production by Photosystem I Multilayer Assemblies. *Adv. Funct. Mater.* **2010**, *20*, 4048–4054.

(2) Baba, K.; Itoh, S.; Hastings, G.; Hoshina, S. Photoinhibition of Photosystem I Electron Transfer Activity in Isolated Photosystem I Preparations with Different Chlorophyll Contents. *Photosynth. Res.* **1996**, *47*, 121–130.

(3) Faulkner, C. J.; Lees, S.; Ciesielski, P. N.; Cliffel, D. E.; Jennings, G. K. Rapid Assembly of Photosystem I Monolayers on Gold Electrodes. *Langmuir* **2008**, *24*, 8409–8412.

APPENDIX C

$Co(bpy)_3^{2+/3+}$ AND $Fe(CN)_6^{4-/3-}$ AS HOLE TRANSFER SPECIES WITHIN PSI-BASED DYE-SENSITIZED SOLAR CELLS

Dye-Sensitized Solar Cells (DSSCs)

Three modular materials systems are contained within a DSSC, namely a hole-extracting p-type layer, an electron extracting n-type layer, and sensitizing molecule bound to the surface of the n-type layer (**Figure C.1**). Typically, the n-type layer is a wide band gap (3-4 eV) inorganic metal-oxide such as ZnO, Fe_2O_3, or TiO_2 with ample sites for coordination with specific chemical functionalities present on the sensitizer.[1,2]

Basic operation can be summarized as follows. Solar energy propagates through a window layer of indium tin oxide (ITO)- or fluorine-doped tin oxide (FTO)-coated glass, striking a particle layer of n-type material coated in dye-molecules. The light stimulates an electronic transition in the dye-molecule; an electron is generated at an energy outlined by its lowest unoccupied molecular orbital (LUMO), and a hole is generated at its highest occupied molecular orbital (HOMO). Driven by favorable free energy change, the generated electron drifts to the conduction band of the n-type layer. Similarly, excess electrons supplied by redox-active solution-phase mediators or p-type polymers (for solid-state systems) annihilate holes left on the sensitizer.

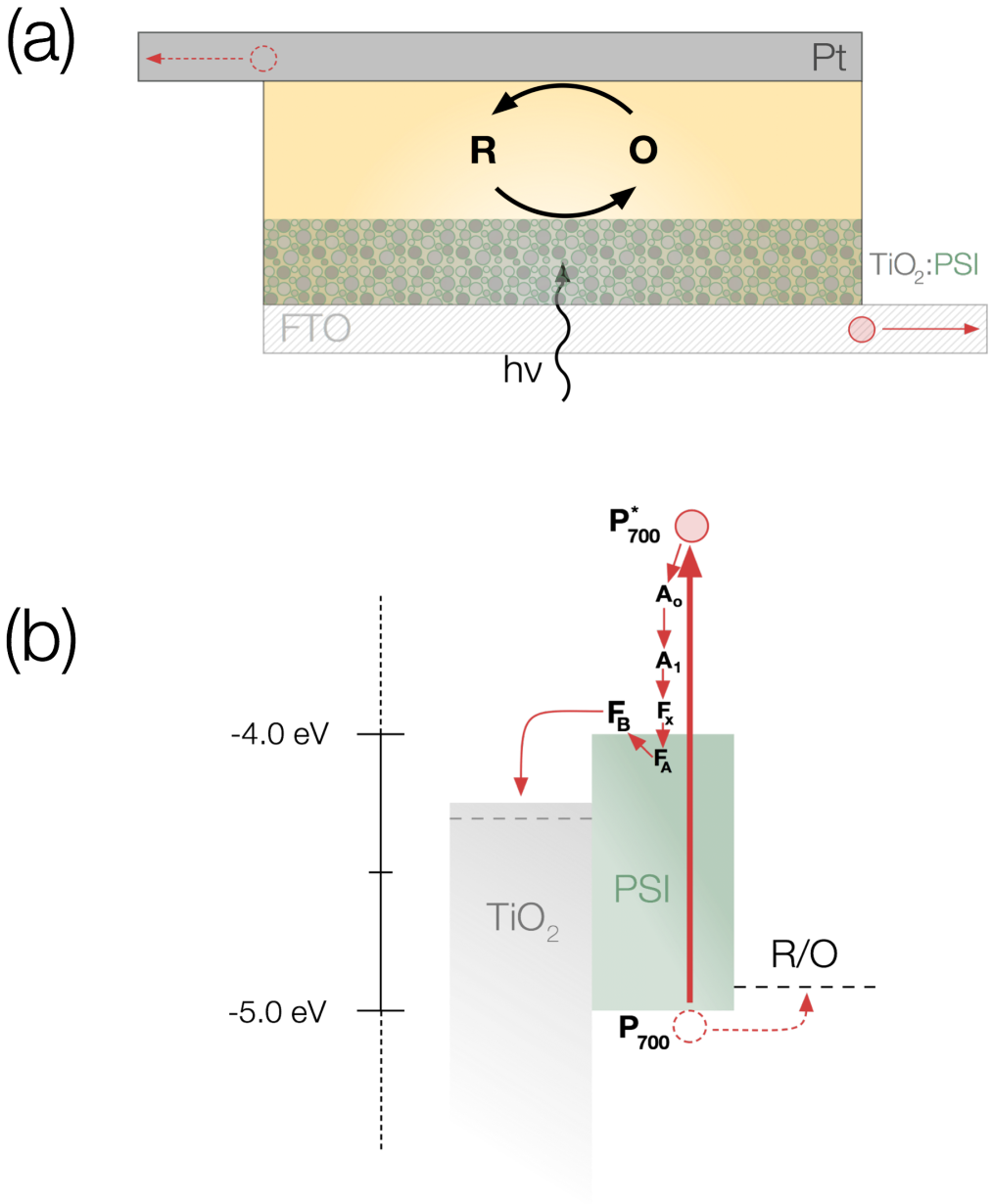

Figure C.1. Aqueous Dye-Sensitized Solar Cell based on Photosystem I Proteins. (a) Visual model of two-electrode device. (b) Generalized energy diagram of proposed design.

$Co(bpy)_3^{2+/3+}$ and $Fe(CN)_6^{4-/3-}$ as Aqueous Redox Mediators

Previous studies of PSI-based DSSCs have implemented electrolytes based on organic solvents, including acetonitrile (ACN) or ethylene carbonate.[3–5] Ultimately, however, the switch to an aqueous system is imperative to permit more complete replication of in-vivo dielectric and pH conditions to optimize protein activity and longevity in devices. Furthermore, the use of toxic or high vapor pressure solvents like ACN hampers the wider application of DSSCs because of stringent sealant requirements.[6] Therefore, water-soluble redox pairs were investigated.

The chosen mediator system must efficiently transfer electrons to P_{700}+, and therefore must exhibit a formal potential more negative of 0.3 V vs. Ag/AgCl. Two mediator systems that satisfy this requirement, $Fe(CN)_6^{4-/3-}$ and $Co(bpy)_3^{2+/3+}$, have been identified and were studied to elucidate unique advantages and limitations to their use within aqueous DSSCs (**Figure C.2**).

Previous work in this group established the utility of the $Fe(CN)_6^{4-/3-}$ couple (E^o=0.25 V vs. Ag/AgCl) in combination with monolayers[7] and multilayers[8,9] of PSI on gold electrodes. Furthermore, Daeneke et. al. reported efficient aqueous DSSCs based on this couple using well characterized sensitizers[10] However, UV-light is known to stimulate irreversible degradation in this pair in proportion to concentration.[11] Care should be taken when exceeding ~10 mM loadings. Consequently, all $Fe(CN)_6^{4-/3-}$ investigations have been conducted at 100 μM R/O concentrations. The species is readily available from chemical suppliers.

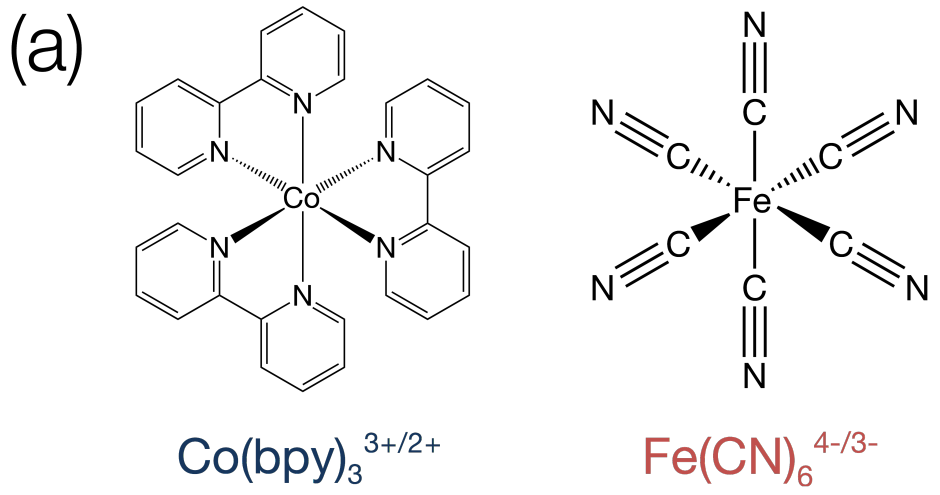

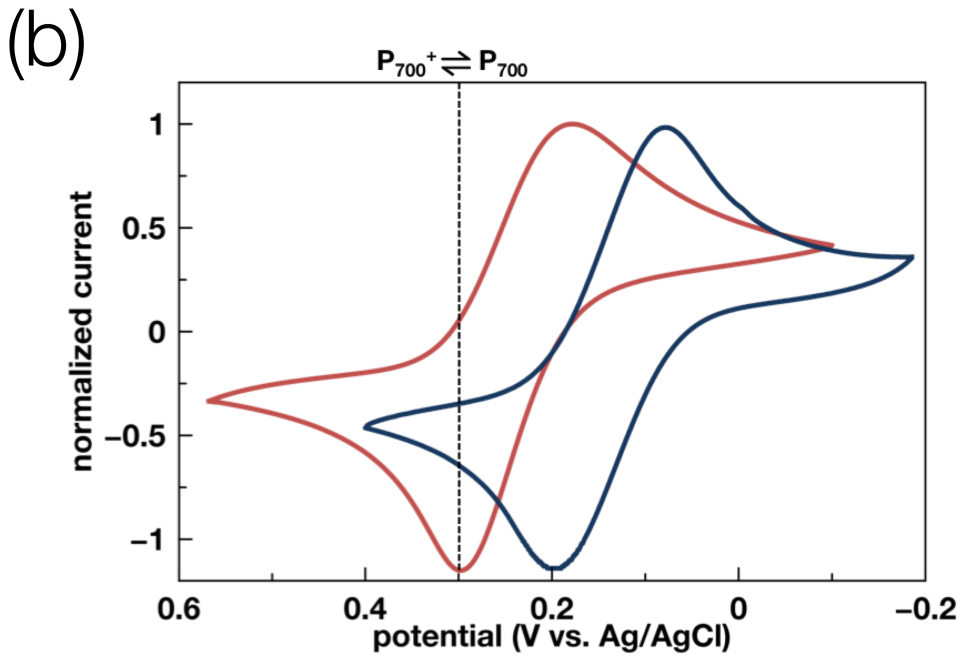

Figure C.2. Electrochemical Characterization of Aqueous Mediators. Structure (a) and characteristic cyclic voltammetry of $Co(bpy)^{2+/3+}$ and $Fe(CN)^{4-/3-}$, denoting P_{700} redox potential (b). Mediator formal potentials can be estimated by averaging the potentials at anodic and cathodic current maximums.

$Co(bpy)_3^{2+/3+}$ has been used effectively as a substitute for iodide/triiodide in organic solvent-based DSSCs.[12,13] Furthermore, it has been recently reported that the $Co(bpy)_3^{2+/3+}$ redox pair performs well in aqueous DSSCs, and does not deteriorate significantly under UV irradiance.[14] Additionally, its redox potential is 100 mV more negative of $Fe(CN)_6^{4-/3-}$ (~.15 V vs. Ag/AgCl), which implies augmented overpotential for P_{700}^+ reduction. The synthesis procedure is simple; the reduced form is acquired by ligand exchange from $Co(NO_3)_2 \bullet H_2O$ with 2,2-bipyridine (both commercially available) and the oxidized form is produced *via* homogeneous reaction between the reduced form and silver nitrate.[14] Note that silver was removed from the oxidized product solution using vacuum filtration.

The performance characteristics of both redox species have been assessed photoelectrochemically as coupled to mesoporous TiO_2 modified by PSI monolayers (**Figure C.3**). Steady state short-circuit current densities were estimated using photochronoamperometry (PCA). Briefly, dark equilibrium potentials are assessed potentiometrically and then used as the working electrode potential for the time-resolved current measurement. Illuminated open circuit potentials were estimated through time-resolved measurement of the change in working electrode potential from dark to illuminated conditions, providing time for steady states to emerge at each stage. The three-electrode results are normalized to the dark open circuit potential (as shown) to provide an estimate for V_{OC}. For all measurements, the TiO_2 was masked with plater's tape to expose a 0.28 cm^2 surface area to the bulk electrolyte; this area was used in calculation of photocurrent density. During measurements, the light source was directed such that photons impinged from the FTO window layer into the TiO_2; the total area of

illumination was approximately 1 in x 0.5 in (3.2 cm^2). Regardless of redox mediator chosen, the inclusion of PSI to the photoanode was observed to increase photocurrent density (**Figure C.3a**) and photovoltage (**Figure C.3b**) by ~20 $\mu A/cm^2$ and ~100 mV, respectively.

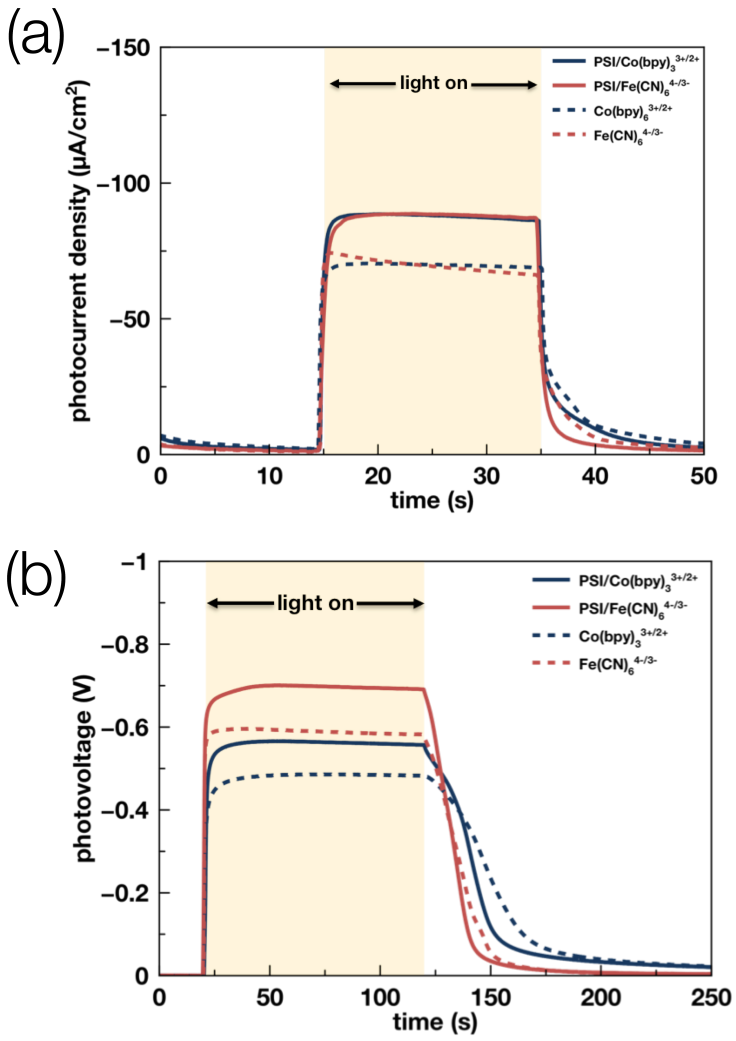

Figure C.3. Photoelectrochemical Performance of PSI Monolayers Adsorbed atop Mesoporous TiO_2 Using the $Fe(CN)_6^{4-/3-}$ and $Co(bpy)_3^{2+/3+}$ Redox Pairs. (a) Steady-state short circuit current measurements indicate charge-transfer limitations at the PSI-TiO_2 interface. (b) Steady-state open circuit voltage under illumination indicates ~100 mV improvements based on monolayer incorporation. Cells consist of PSI monolayer-coated mesoporous TiO_2 in contact with a 100 μM of both the reduced and oxidized form of the redox couple, 100 mM KCl, and 5 mM phosphate buffer (pH 7.0).

Multilayer systems stabilized on mesoporous TiO_2 anodes have been analyzed using a solution containing 5 mM/.5 mM $Co(bpy)_3^{2+/3+}$ and 100 mM KCl as supporting electrolyte. Multilayers provide an additional photocurrent enhancement over monolayers (**Figure C.4**). Augmented charge injection rates through adsorbed PSI or directly *via* exposed Ti centers are established due to the rapid production of reduced mediator by delocalized F_B^- throughout multilayer films.

Optimum PSI multilayer deposition conditions have been identified (**Figure C.4a**). A maximum J_{SC} when as-dialyzed protein solutions are diluted by 100% (1:1 deionized water (DIW):PSI solution); this enhancement represents a four-fold enhancement over bare mesoporous TiO_2. Profilometry indicates a negligible change in average layer thickness (all films were ~350 nm thick) with dilution, indicating that dilute PSI packs into a more porous film during the evaporation step, affording faster mediator diffusion. This effect is diminished as PSI loading dips below a certain threshold (as in 2:1 DIW:PSI solution); ultimately, diffusional rates fail to counterbalance attenuation of bulk O reduction. Additionally, pH control was applied as an attempt to stimulate more intimate electrostatic interaction between TiO_2 and PSI (**Figure C.4b**). Both highly protonated (pH 4) and deprotonated (pH 10) conditions yield lower average photocurrents.

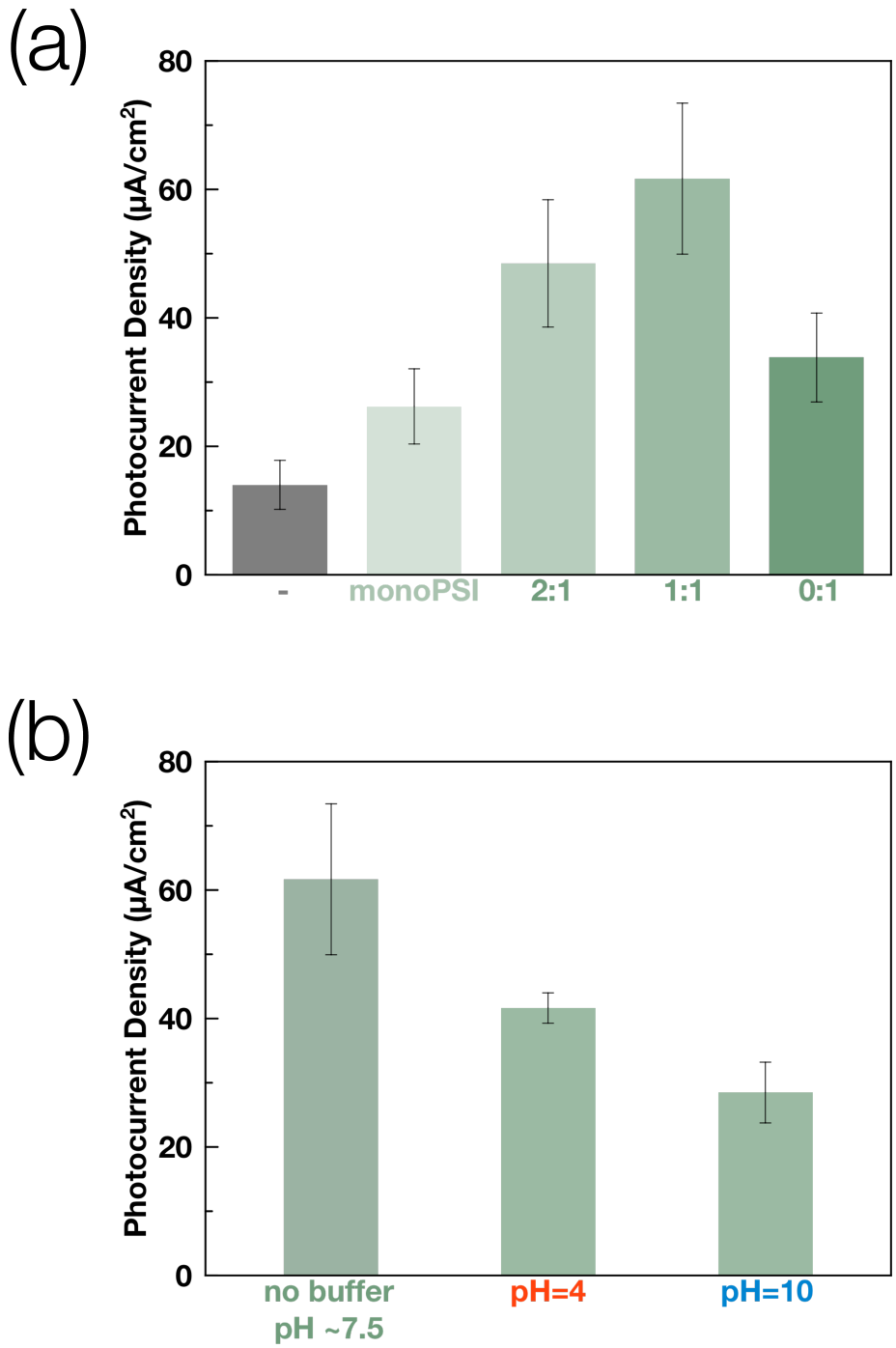

Figure C.4. Characterization of Multilayer Enhancements for Mesoporous TiO_2 films. (a) Effect of film quality on multilayer-based photocurrent enhancement. (b) pH dependence of 1:1 DIW:PSI photocurrent production. The electrolyte used in all studies is a 5 mM/.5 mM $Co(bpy)_3^{2+/3+}$ with 100 mM KCl as supporting electrolyte; a 10 mM phosphate buffer was used for pH modification.

Works Cited

(1) Hardin, B. E.; Snaith, H. J.; McGehee, M. D. The Renaissance of Dye-Sensitized Solar Cells. *Nat. Photonics* **2012**, *6*, 162–169.

(2) Grätzel, M. Photoelectrochemical Cells. *Nature* **2001**, *414*, 338–344.

(3) Mershin, A.; Matsumoto, K.; Kaiser, L.; Yu, D.; Vaughn, M.; Nazeeruddin, M. K.; Bruce, B. D.; Grätzel, M.; Zhang, S. Self-Assembled Photosystem-I Biophotovoltaics on Nanostructured TiO2 and ZnO. *Sci. Rep.* **2012**, *2*, 1–7.

(4) Yu, D.; Wang, M.; Zhu, G.; Ge, B.; Liu, S.; Huang, F. Enhanced Photocurrent Production by Bio-Dyes of Photosynthetic Macromolecules on Design TiO_2 Film. *Sci. Rep.* **2015**, *5*, 1–9.

(5) Ocakoglu, K.; Krupnik, T.; van den Bosch, B.; Harputlu, E.; Gullo, M. P.; Olmos, J. D. J.; Yildirimcan, S.; Gupta, R. K.; Yakuphanoglu, F.; Barbieri, A.; et al. Photosystem I-Based Biophotovoltaics on Nanostructured Hematite. *Adv. Funct. Mater.* **2014**, *24*, 7467–7477.

(6) Law, C.; Pathirana, S. C.; Li, X.; Anderson, A. Y.; Barnes, P. R. F.; Listorti, A.; Ghaddar, T. H.; O'Regan, B. C. Water-Based Electrolytes for Dye-Sensitized Solar Cells. *Adv. Mater.* **2010**, *22*, 4505–4509.

(7) Ciesielski, P. N.; Faulkner, C. J.; Irwin, M. T.; Gregory, J. M.; Tolk, N. H.; Cliffel, D. E.; Jennings, G. K. Enhanced Photocurrent Production by Photosystem I Multilayer Assemblies. *Adv. Funct. Mater.* **2010**, *20*, 4048–4054.

(8) Ciesielski, P. N.; Cliffel, D. E.; Jennings, G. K. Kinetic Model of the Photocatalytic Effect of a Photosystem I Monolayer on a Planar Electrode Surface.

J. Phys. Chem. A **2011**, *115*, 3326–3334.

(9) Chen, G.; LeBlanc, G.; Jennings, G. K.; Cliffel, D. E. Effect of Redox Mediator on the Photo-Induced Current of a Photosystem I Modified Electrode. *J. Electrochem. Soc.* **2013**, *160*, H315–H320.

(10) Daeneke, T.; Uemura, Y.; Duffy, N. W.; Mozer, A. J.; Koumura, N.; Bach, U.; Spiccia, L. Aqueous Dye-Sensitized Solar Cell Electrolytes Based on the Ferricyanide-Ferrocyanide Redox Couple. *Adv. Mater.* **2012**, *24*, 1222–1225.

(11) Arellano, C. A. P.; Martínez, S. S. Effects of pH on the Degradation of Aqueous Ferricyanide by Photolysis and Photocatalysis under Solar Radiation. *Sol. Energy Mater. Sol. Cells* **2010**, *94*, 327–332.

(12) Yum, J.-H.; Baranoff, E.; Kessler, F.; Moehl, T.; Ahmad, S.; Bessho, T.; Marchioro, A.; Ghadiri, E.; Moser, J.-E.; Yi, C.; et al. A Cobalt Complex Redox Shuttle for Dye-Sensitized Solar Cells with High Open-Circuit Potentials. *Nat. Commun.* **2012**, *3*, 631.

(13) Liu, Y.; Jennings, J. R.; Huang, Y.; Wang, Q.; Zakeeruddin, S. M.; Gr, M. Cobalt Redox Mediators for Ruthenium-Based Dye-Sensitized Solar Cells : A Combined Impedance Spectroscopy and Near-IR Transmittance Study. **2011**, 18847–18855.

(14) Xiang, W.; Huang, F.; Cheng, Y.-B.; Bach, U.; Spiccia, L. Aqueous Dye-Sensitized Solar Cell Electrolytes Based on the Cobalt(II)/(III) Tris(bipyridine) Redox Couple. *Energy Environ. Sci.* **2013**, *6*, 121–127.

APPENDIX D

MACROPOROUS TITANIA FOR INCREASED LOADING OF PSI PROTEINS IN DYE-SENSITIZED SOLAR CELL PHOTOANODES

TiO_2 is a wide band gap semiconductor frequently employed in dye-sensitized solar cells (DSSCs). It has a band gap of 3.2 eV with reported conduction and valence bands of -4.3 eV and -7.6 eV, respectively.[1] The TiO_2 conduction band is an energetic match with PSI, providing at most ~300 mV of overpotential for electron injection from F_B^-.[2–4] Anodes are assembled from doctor-bladed colloidal pastes atop FTO-coated glass. A final sintering step at 500 ^oC fixes the crystal structure in the anatase phase.[5]

However, the narrow pore structure of mesoporous TiO_2 does not adequately accommodate the protein's considerable size. Our independently conducted dynamic light scattering (DLS) analysis confirms the conclusions of Liu et. al., in which PSI was observed to aggregate in surfactant-stabilized micellar structures with an average effective diameter of >40 nm (**Figure D.1**).[6] Therefore, mesoporous films, which incorporate pore sizes of less than 50 nm, are expected to curtail solution-based PSI penetration (**Figure D.2A**). This is corroborated by UV-vis data (**Figure D.2B**), which reveal very low PSI loading within a mesoporous film. This suggests that a more open pore structure in the TiO_2 photoanode will improve device performance due to augmented incorporation of PSI.

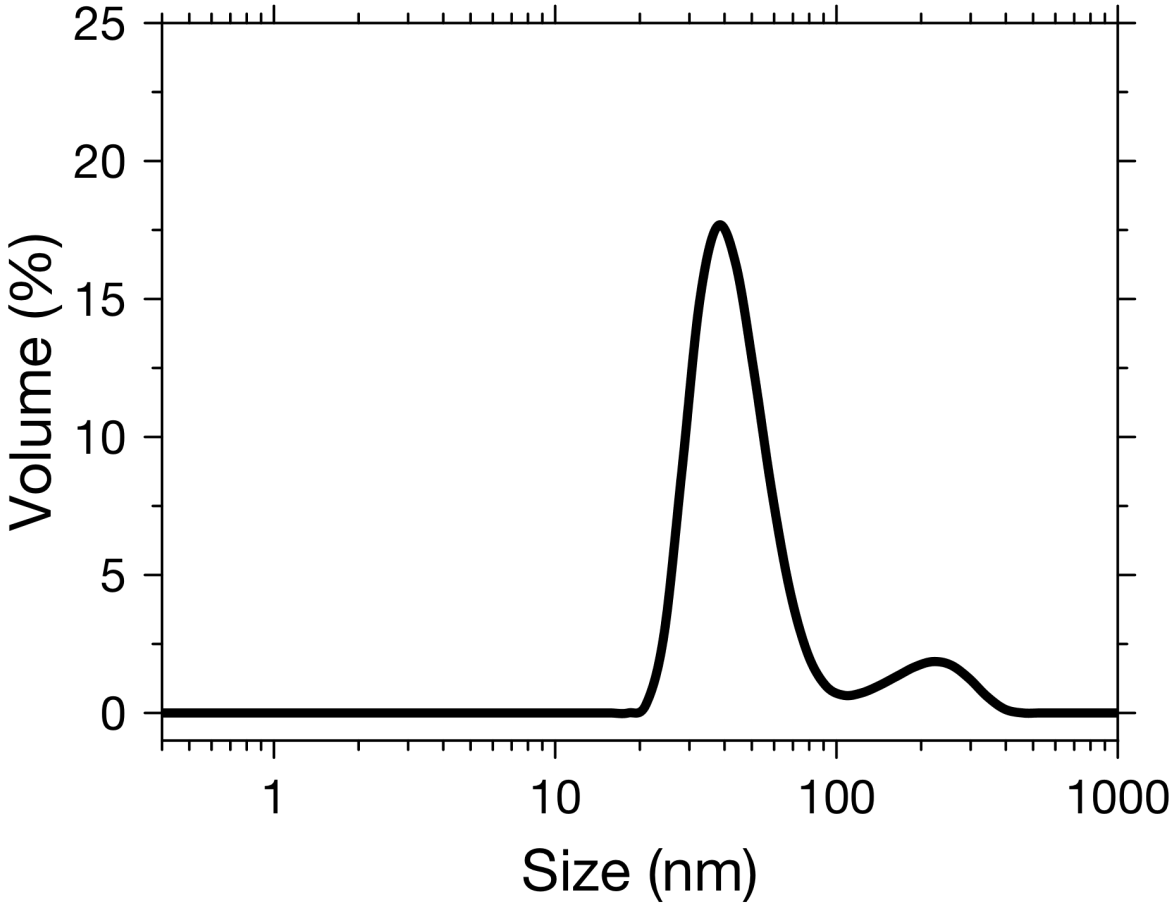

Figure D.1. DLS for Determination of PSI Protein Diameter in Solution. DLS demonstrates that PSI in solution takes up a total volume of ~40 nm, which will occlude its penetration into mesoporous films of titania ($d_{pore} \leq 50$ nm) The data shown were taken from DLS measurements of dialyzed solutions of PSI that were diluted by 1000x (C_{PSI}~10 pM). Measurements taken at 500x dilution showed similar peaks.

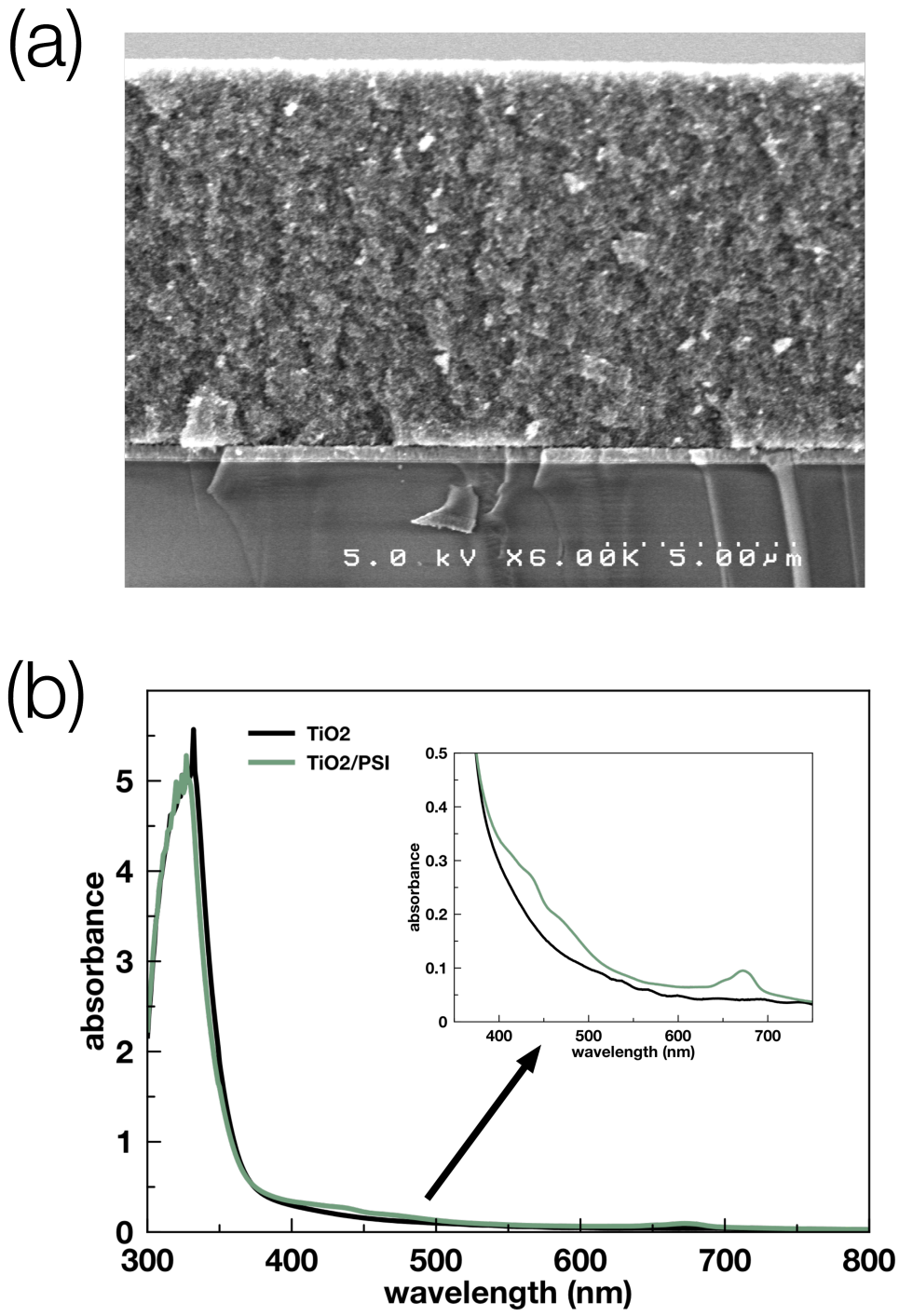

Figure D.2. Mesoporous TiO_2 Photoanodes. (a) Cross-sectional SEM demonstrating narrow pore structure. (b) Absorbance profiles for bare and PSI monolayer-coated TiO_2 illustrates limited protein incorporation.

To allow rapid PSI integration within this proposed architecture, provision of film-pervasive, interconnected macropores (d_{pore}>50 nm) is necessary. To achieve needed interconnections without making the film brittle (i.e. individual pores that are so large or so dense as to detrimentally overlap), a hierarchical design is desired, requiring inclusion of two distinct pore sizes. This has been achieved by combining oil-in-water emulsion and polystyrene TiO_2 templating techniques to confer large and small template size domains, respectively.

Phadke et. al. report a method to create macroporous (d_{pore}>50 nm) TiO_2 using an oil-in-water emulsion templating method, based on the surfactants Tween and Span.[7–9] They substitute water included in a standard TiO_2 paste with an emulsion, allowing formation of oil droplets of controllable diameter; under the high heat of sintering, the oil evaporates and leaves behind pores of a specific size distribution. As a maximum, they report ~100 nm pores using a 40% oil-in-water emulsion; unfortunately, films were difficult to reproduce and were not observed to develop adequate pore interconnections.

Reproducible pore-pore connections are observed upon addition of spherical polystyrene particles into oil-in-water emulsions, as is evident in scanning electron microscopy (SEM) images (**Figure D.3a**). Film preparation modifies the approach of Nazeeruddin et. al.,[10] in which the templating mixture supplants DIW addition. Presently, the best films are achieved by employing a 1:1 mixture of 60% oil-in-water emulsion and 1 μm-diameter polystyrene particles (60%+1μm), permitting very large (up to several μm) and small (~.75 μm) pore domains, contributed by the emulsion and polystyrene particles, respectively. Significantly improved PSI incorporation is demonstrated in UV-vis data (**Figure D.3b**).

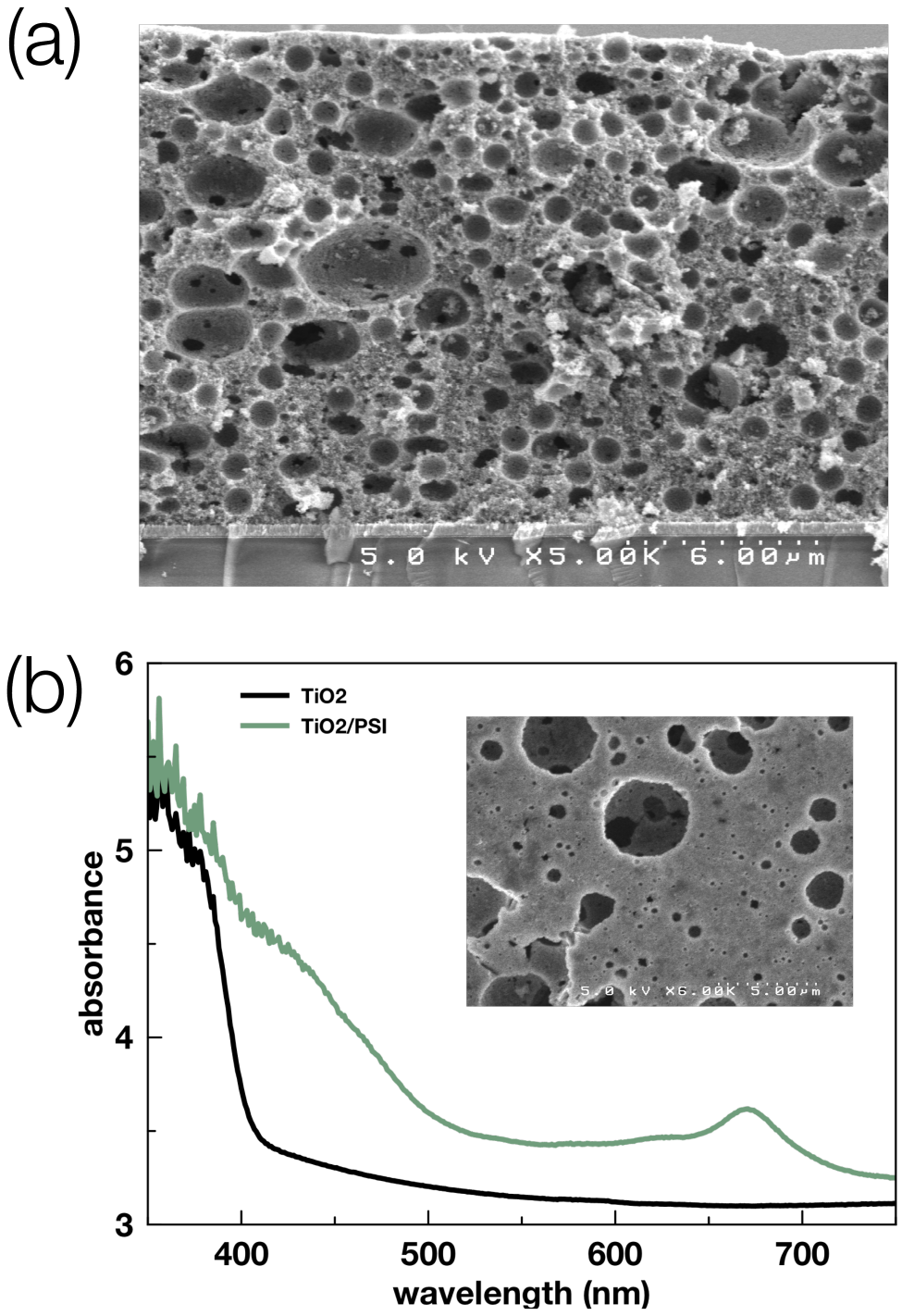

Figure D.3. Macrotemplated TiO_2. (a) cross sectional view of 60%+1µm templated TiO_2 anodes. (b) UV-vis spectra indicating high incorporation of PSI proteins throughout interconnected pore structure as indicated in top-view SEM (inset).

Works Cited

(1) Linsebigler, A. L.; Lu, G.; Yates, J. T. Photocatalysis on TiO_2 Surfaces: Principles, Mechanisms, and Selected Results. *Chem. Rev.* **1995**, *95*, 735–758.

(2) Mershin, A.; Matsumoto, K.; Kaiser, L.; Yu, D.; Vaughn, M.; Nazeeruddin, M. K.; Bruce, B. D.; Grätzel, M.; Zhang, S. Self-Assembled Photosystem-I Biophotovoltaics on Nanostructured TiO_2 and ZnO. *Sci. Rep.* **2012**, *2*, 1–7.

(3) Yu, D.; Wang, M.; Zhu, G.; Ge, B.; Liu, S.; Huang, F. Enhanced Photocurrent Production by Bio-Dyes of Photosynthetic Macromolecules on Design TiO_2 Film. *Sci. Rep.* **2015**, *5*, 1–9.

(4) Ocakoglu, K.; Krupnik, T.; van den Bosch, B.; Harputlu, E.; Gullo, M. P.; Olmos, J. D. J.; Yildirimcan, S.; Gupta, R. K.; Yakuphanoglu, F.; Barbieri, A.; et al. Photosystem I-Based Biophotovoltaics on Nanostructured Hematite. *Adv. Funct. Mater.* **2014**, *24*, 7467–7477.

(5) Zarick, H. F.; Hurd, O.; Webb, J. A.; Hungerford, C.; Erwin, W. R.; Bardhan, R. Enhanced Efficiency in Dye-Sensitized Solar Cells with Shape-Controlled Plasmonic Nanostructures. *ACS Photonics* **2014**, *1*, 806–811.

(6) Liu, J.; Zhang, X.; Wang, M.; Liu, J.; Cao, M.; Lu, J.; Cui, Z. Characterization of Photosystem I from Spinach: Effect of Solution pH. *Photosynth. Res.* **2012**, *112*, 63–70.

(7) Phadke, S.; Du Pasquier, A.; Birnie, D. P. Enhanced Electron Transport through Template-Derived Pore Channels in Dye-Sensitized Solar Cells. *J. Phys. Chem. C* **2011**, *115*, 18342–18347.

(8) Phadke, S. A. Dye Sensitized Solar Cells with Templated TiO2 Coatings, Rutgers

University, 2010.

(9) Phadke, S.; Ho, J.; Birnie, D. P. Emulsion Templating to Obtain Dual-Size-Scale Mesoporous Titania Coatings. *Mater. Lett.* **2009**, *63*, 2619–2621.

(10) Nazeeruddin, M. K.; Kay, A.; Rodicio, I.; Humphry-Baker, R.; Müller, E.; Liska, P.; Vlachopoulos, N.; Grätzel, M. Conversion of Light to Electricity by Cis-X_2Bis(2,2'-bipyridyl-r,r'-dicarboxylate)ruthenium(II) Charge-Transfer Sensitizers (X= Cl-, Br-, I-, CN-, and SCN-) on Nanocrystalline TiO_2 Electrodes. *J. Am. Chem. Soc.* **1993**, *115*, 6382–6390.

APPENDIX E

INCORPORATION OF PLASMONIC NANOCUBES WITHIN PHOTOSYSTEM I MULTILAYER FILMS FOR PHOTOCURRENT ENHANCEMENT

Chapter 3 shows that multilayer films of PSI proteins in mediated environments produce larger photocurrents with higher intra-film flux of red photons. Therefore, photocurrents from PSI multilayers would be expected to produce higher photocurrents with the same source photon flux if additive species were included help retain photon flux within the film. Herein, this is accomplished with silver-coated gold nanocubes (Au@Ag NCs) that scatter red light efficiently (**Figure E.1**). To make composite multilayer films containing PSI and Au@Ag NCs, a modified vacuum-assisted assembly procedure was used. Briefly, the nanoparticles produced from the synthesis procedure that are coated in CTAB[1] were centrifuged at 1100 x g for 18 min and the pellet was resuspended in DIW. Subsequently, this solution was centrifuged 1100 x g for 18 min and the pellet resuspended in 1 mM mercaptopropylsulfonate (MPS) to promote ligand exchange. After 30 min, the MPS-coated Au@Ag NCs were centrifuged at 1100 x g for 18 min and the pellet resuspended in DIW. This solution was then mixed with an aqueous solution of PSI and was subsequently drop cast to form a composite film containing Au@Ag NCs and PSI. Photocurrent tests demonstrate that the addition of Au@Ag NCs to PSI multilayer films significantly improves photocurrent (**Figure E.2**).

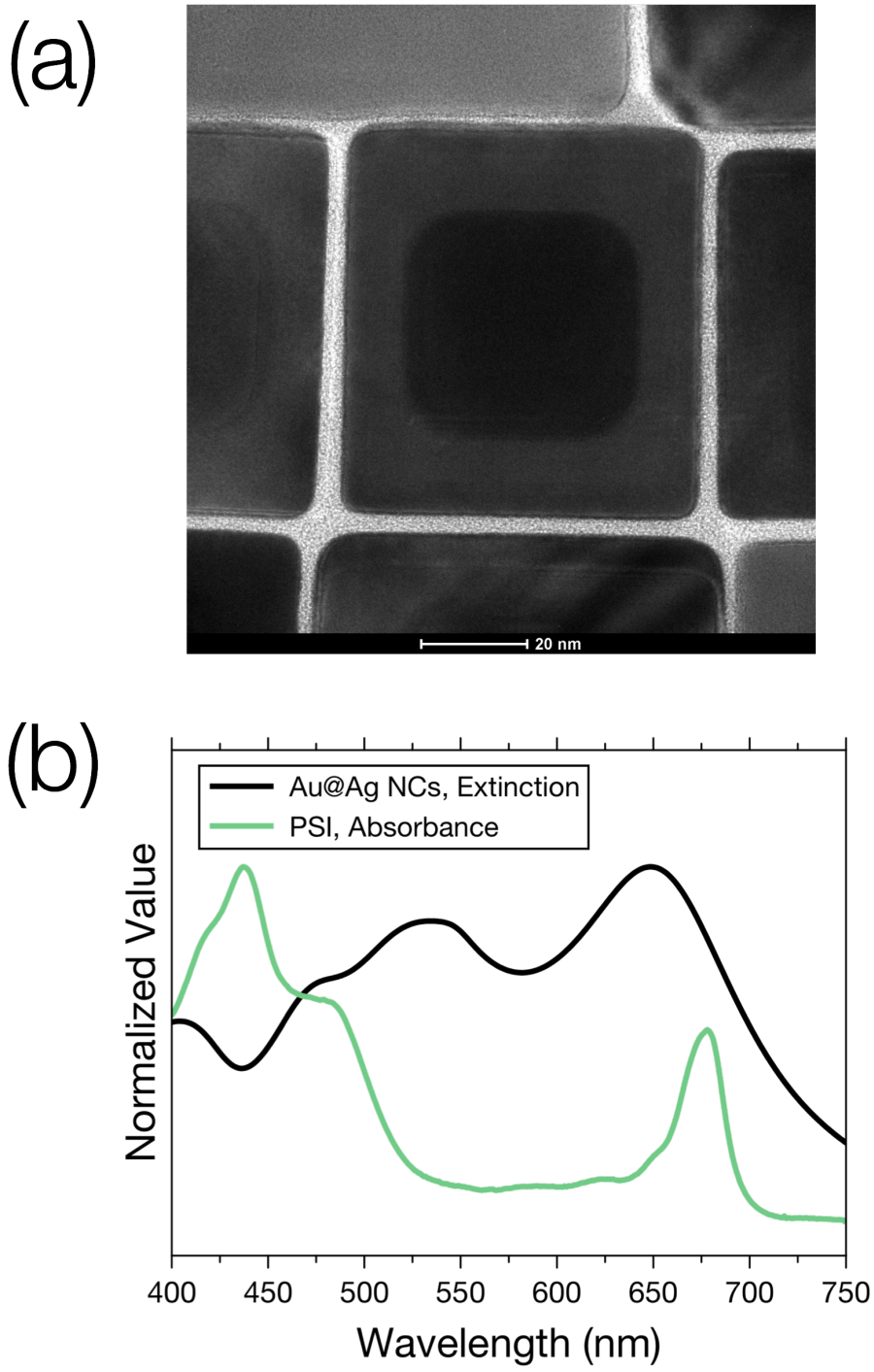

Figure E.1. Physical and Optical Characteristics of Au@Ag NCs. (a) Au@Ag NCs were produced with ~60 nm side length consisting of an inner cube of Au (side length = 40 nm) and a 10-15 nm shell of Ag. (b) Extinction spectra of solutions of Au@Ag NCs (black curve) demonstrate its high scattering characteristics for red light that corresponds to chlorophyll absorbance of PSI proteins (green curve).

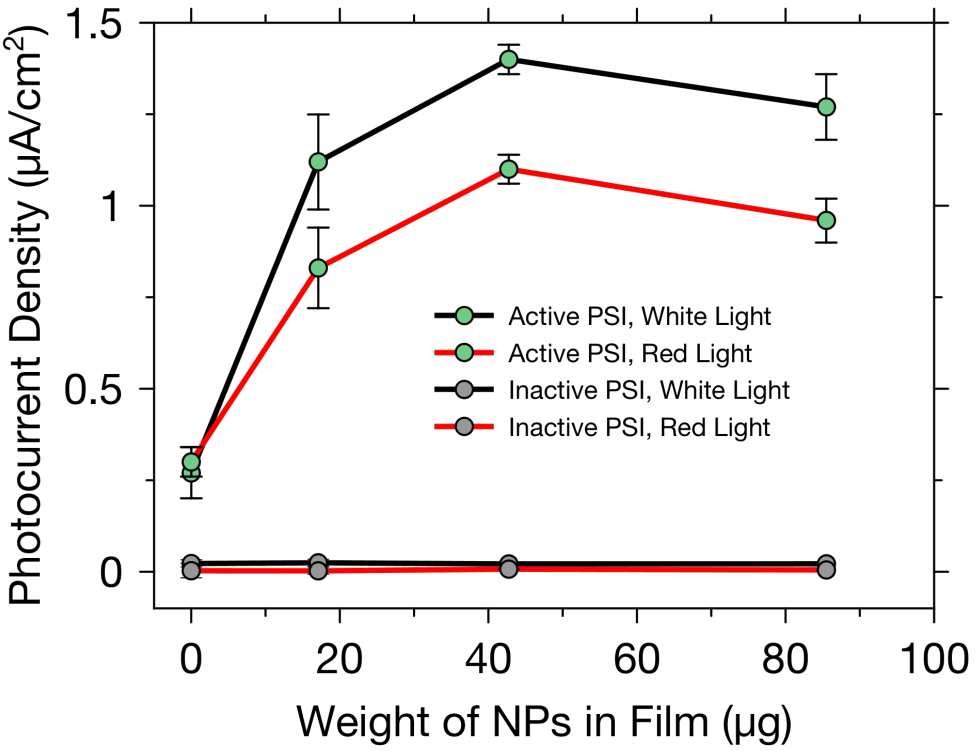

Figure E.2. Photocurrent Enhancement of PSI Multilayers with Incorporation of Au@Ag NCs. NC incorporation within PSI multilayers permits a more than 5-fold improvement in photocurrent relative to unmodified PSI multilayer films. A maximum average photocurrent of 1.4 μA/cm^2 is observed for incorporation of 43 μg of NCs within a 600 nm-thick PSI film. The red light enhancement is 80% that of full spectrum enhancement, suggesting that the high red light scattering of the nanoparticles underlies improvements. In agreement with the scattering hypothesis, when the PSI used in drop casting is photobleached by way of exposure to high-intensity UV light for 5 h (inactive PSI), the photocurrent enhancements are not observed with NC incorporation. The photoelectrochemical cell consisted of Au/AET with a composite NC+PSI film on top exposed to an aqueous electrolyte containing 100 mM KCl, 20 mM sodium ascorbate, and 1 mM dichloroindophenol. White light illumination was 54 mW/cm^2. Red light illumination was provided through use of an optical filter (cutoff = 633 nm). Red light intensity was 26 mW/cm^2.

Works Cited

(1) Zarick, H. F.; Hurd, O.; Webb, J. A.; Hungerford, C.; Erwin, W. R.; Bardhan, R. Enhanced Efficiency in Dye-Sensitized Solar Cells with Shape-Controlled Plasmonic Nanostructures. *ACS Photonics* **2014**, *1*, 806–811.